MESO-SCALE FINITE ELEMENT MODELLING OF CARBON NANOTUBE REINFORCED POLYMER COMPOSITES

A THESIS SUBMITTED TO
THE BOARD OF GRADUATE PROGRAMS
OF
MIDDLE EAST TECHNICAL UNIVERSITY, NORTHERN CYPRUS CAMPUS

BY

ALTAY HAYDAR

IN PARTIAL FULFILLMENT OF THE REQUIREMENTS
FOR
THE DEGREE OF MASTER OF SCIENCE
IN MECHANICAL ENGINEERING PROGRAM

DECEMBER 2021

Approval of the Board of Graduate Programs

Prof. Dr. Cumali Sabah

Chairperson

I certify that this thesis satisfies all the requirements as a thesis for the degree of Master of Science

Prof. Dr. Eşref Eşkinat

Program Coordinator

This is to certify that we have read this thesis and that in our opinion it is fully adequate, in scope and quality, as a thesis for the degree of Master of Science.

Assoc. Prof. Dr. Volkan Esat

Supervisor

Examining Committee Members

Asst. Prof. Dr. Ali Atashbar Orang	Mechanical Engineering Program / METU NCC	
Assoc. Prof. Dr. Volkan Esat	Mechanical Engineering Program / METU NCC	
Asst. Prof. Dr. Süleyman Aşır	Material Science and Nanotechnology Engineering Department / NEU	

I hereby declare that all information in this document has been obtained and presented in accordance with academic rules and ethical conduct. I also declare that, as required by these rules and conduct, I have fully cited and referenced all material and results that are not original to this work.

Name, Last Name : Altay, Haydar

Signature :

ABSTRACT

MESO-SCALE FINITE ELEMENT MODELLING OF CARBON NANOTUBE REINFORCED POLYMER COMPOSITES

Haydar, Altay
Master of Science, Mechanical Engineering Program
Supervisor: Assoc. Prof. Dr. Volkan Esat

December 2021, 112 Pages

Carbon nanotube (CNT) reinforced polymer composites (CNTRPs) are promising materials which can be utilized in a variety of industries. Several experimental research studies have been conducted to determine the mechanical properties of CNTRPs, however results have not been conclusive. In this study, meso-scale representative volume elements (RVEs) of straight and coiled CNT (CCNT) reinforced epoxy composites were analysed by using commercial finite element analysis software MSC Marc-Mentat. CNTs were randomly distributed and oriented inside the RVE by using developed C++ code. The interface region between CNT and epoxy was modelled by exploiting Cohesive Zone Modelling (CZM) feature of Marc. Weak van der Waals interaction between CNT and epoxy is considered. In randomly oriented CNTs case, increasing CNT volume fraction, CCNT helix angle, and CCNT number of revolutions had positive effects on elastic properties of CNTRP while increasing CNT diameter had detrimental effects. In aligned CNTs case, CNTRP had improved mechanical property in the alignment direction. End structure of CNT (blunt or capped) did not have any significant effect on the elastic properties of CNTRP. Maximum Von Mises stress and maximum elastic strain in CNT showed an increasing trend with raise in CNT volume fraction. Rise in CCNT helix angle slightly increased CNTRP's Poisson's ratio while increasing CCNT number of revolutions and CNT diameter did the exactly opposite. The results obtained from finite element analyses (FEAs) were compared with well-known analytical micromechanics models. This study claims to have developed a novel CCNT reinforced epoxy composite finite element model.

Keywords: Finite element analysis, carbon nanotube reinforced polymer composites, cohesive zone modelling, coiled carbon nanotube, capped carbon nanotube

ÖZ

KARBON NANOTÜP TAKVİYELİ POLİMER KOMPOZİTLERİN MEZO ÖLÇEKTE SONLU ELEMANLAR MODELLENMESİ

Haydar, Altay
Yüksek Lisans, Makina Mühendisliği Programı
Tez Yöneticisi: Doç. Dr. Volkan Esat

Aralık 2021, 112 Sayfa

Karbon nanotüp (KNT) takviyeli polimer kompozitler (KNTTP) çeşitli sektörde uygulanmak üzere gelecek vaadeden bir malzemedir. KNTTP'lerin mekanik özelliklerini ölçmek için birçok deneysel çalışma yapılmıştır fakat elde edilen sonuçlar kesin değildir. Bu çalışmada mezo ölçekte oluşturulan düz veya sarmal KNT (SKNT) takviyeli epoksi kompozit temsili hacim elemanlarının (THE) bir ticari sonlu elemanlar analizi yazılımı olan MSC Marc-Mentat kullanılarak analizleri yapılmıştır. Geliştirilen C++ kodu kullanılarak KNT'ler THE içerisinde rastgele dağıtılmış ve yönlendirilmiştir. KNT ve epoksinin arayüzü Marc'ın birleşik bölge modellemesi (BBM) özelliği kullanılarak modellenmiştir. KNT ve epoksi arasında zayıf van der Waals etkileşimi göz önünde bulundurulmuştur. KNT'lerin rastgele yönlendirildiği durumda KNT hacim oranı, SKNT helis açısı ve SKNT tur sayısını artırmanın KNTTP'in elastik özelliklerine olumlu etkisi olurken KNT'ün çapının artırılmasının zararlı etkisi olmuştur. KNT'lerin belli bir yönde doğrultulduğu durumda KNTTP'in mekanik özelliği doğrultu yönünde artmıştır. KNT'ün uç yapısının (küt veya şapkalı) KNTTP'in elastik özelliklerine belirgin bir etkisi olmamıştır. KNT'teki maksimum Von Mises gerilimi ve maksimum elastik gerinimi hacim oranındaki yükselmeyle birlikte artan bir eğilim göstermiştir. SKNT'ün helis açısındaki artış KNTTP'in Poisson oranında hafif bir yükselmeye neden olurken SKNT'ün tur sayısı ve KNT çapındaki artış tam ters etkiyi göstermiştir. Sonlu elemanlar analizlerinden (SEA) elde edilen sonuçlar bilinen mikromekanik yöntemlerle karşılaştırılmıştır. Bu çalışmada yeni bir SKNT takviyeli epoksi kompozit sonlu elemanlar modeli oluşturulduğu düşünülmektedir.

Anahtar Kelimeler: Sonlu elemanlar analizi, karbon nanotüp takviyeli polimer kompozitler, birleşik bölge modellemesi, sarmal karbon nanotüp, şapkalı karbon nanotüp

To my parents Sıtkı Haydar and Şerife Haydar

ACKNOWLEDGEMENTS

I am grateful to Assoc. Prof. Dr. Volkan Esat for offering me this very interesting topic and supervising my thesis. I would like to also add that he has always been positive and motivating throughout my research.

I also wish to express my appreciation to the other members of my jury, Asst. Prof. Dr. Ali Atashbar Orang and Asst. Prof. Dr. Süleyman Aşır for their insightful comments and recommendations.

Lastly, but most importantly, I would like to thank my father Sıtkı Haydar and my mother Şerife Haydar for their continuous support and encouragement.

TABLE OF CONTENTS

LIST OF TABLES

TABLES

LIST OF FIGURES

FIGURES

LIST OF ABBREVIATIONS

ABBREVIATIONS	
1D	1-Dimensional
3D	3-Dimesnional
ASTM	American Society for Testing and Materials
CCNT	Coiled carbon nanotube (helical carbon nanotube)
CNT	Carbon nanotube
CNTRC	Carbon nanotube reinforced composite
CNTRP	Carbon nanotube reinforced polymer composite
DNA	Deoxyribonucleic acid
EMI	Electromagnetic interference
FE	Finite element
FEA	Finite element analysis
HEPA	High-efficiency particulate air
HRTEM	High resolution transmission electron microscopy
IEA	International Energy Agency
ISO	International Organization for Standardization
LEV	Local exhaust ventilation
MD	Molecular dynamics
MWNT	Multi-walled carbon nanotube
NF	Nanofibre
PBC	Periodic boundary condition
PPE	Personal protective equipment
RET	Reactive ethylene terpolymer
RSA	Random Sequential Adsorption
RVE	Representative volume element
SWNT	Single walled carbon nanotube

LIST OF SYMBOLS

SYMBOLS

A_{CNT}	Cross-sectional area of carbon nanotube
A_{LEF}	Cross-sectional area of equivalent fibre
C_h	Chiral vector
C_{ij} $(i,j=1,2,3)$	Stiffness matrix
C_m	Elasticity tensor of matrix
C_r	Elasticity tensor of fibre
C_θ	Chiral angle
D_e	Dislocation energy
E_{CNT}	Young's modulus of carbon nanotube
E_L	longitudinal modulus
E_{LC}	Longitudinal modulus of micro-scale RVE composite
E_{LEF}	Longitudinal modulus of equivalent fibre
E_M	Young's modulus of matrix
E_{MP-b}	Morse potential bending component
E_{MP-s}	Morse potential bond stretching component
E_T	Transverse modulus
E_{TC}	Transverse modulus of micro-scale RVE composite
E_{TEF}	Transverse modulus of equivalent fibre
E_c	Young's modulus of composite
E_f	Longitudinal modulus of fibre
E_{ijkl} $(i,j,k,l=1,2,3)$	Elasticity tensor
E_{random}	Young's modulus of randomly distributed fibre composite
F_{LJ}	Lennard-Jones potential force
G_C	Shear modulus of micro-scale RVE composite or cohesive energy
G_{EF}	Shear modulus of equivalent fibre
G_L	Longitudinal shear modulus
G_M	Shear modulus of matrix
G_T	Transverse shear modulus
G_c^l	Lower limit bulk modulus of composite
G_c^u	Upper limit shear modulus of composite
G_{in}	Shear modulus of inclusion

G_{out}	Shear modulus of hybrid matrix
G_{random}	Shear modulus of randomly distributed fibre composite
K_T	Transverse bulk modulus
K_c^l	Lower limit bulk modulus of composite
K_c^u	Upper limit bulk modulus of composite
K_f	Bulk modulus of fibre
K_{in}	Bulk modulus of inclusion
K_m	Bulk modulus of matrix
K_{out}	Bulk modulus of hybrid matrix
U_A	Beam strain energy in axial loading
U_M	Beam strain energy in bending
U_T	Beam strain energy in torsion
U_r	Bond stretching energy
U_{vdw}	Non-bonded van der Waals energy
U_Φ	Dihedral angle torsion energy
U_θ	Bond angle bending energy
U_ω	Out of plane torsion energy
V_{EF}	Volume fraction of equivalent fibre
V_{LJ}	Lennard-Jones potential energy
V_M	Volume fraction of matrix
V_r	Volume fraction of reinforcement
$V_r^{inclusion}$	Volume fraction of reinforcement inside inclusions
V_r^m	Volume fraction of reinforcement inside hybrid matrix
a_h, b_h	Helix parameters
$\vec{c}, \vec{d}$	Points on axes of cylinder 1 and 2
c_m	Matrix volume fraction
c_r	Fibre volume fraction
$d_\parallel$	Distance between parallel lines
d_{CNT}	Carbon nanotube diameter
d_f	Diameter of fibre
k_r	Bond stretching force constant
k_θ	Bond angle bending force constant
k_τ	Torsional resistance
l_1, l_2	Line 1, line 2

l_f	Length of fibre
r_{LJ}	Distance between atoms
r_{MP}	Morse potential current bond length
$u_i\ (i = 1, 2, 3)$	Displacement
v_C	Poisson's ratio of micro-scale RVE composite or critical separation distance
v_{CNT}	Poisson's ratio of carbon nanotube
v_{EF}	Poisson's ratio of equivalent fibre
v_f	Poisson's ratio of fibre
v_m	Poisson's ratio of matrix or complete separation distance
v_{out}	Poisson's ratio of hybrid matrix
v_{random}	Poisson's ratio of randomly distributed fibre composite
$x_{int}, y_{int}, z_{int}$	Intersection point x, y, z coordinates
$x_p,\ y_p,\ z_p$	Coordinates of any point on the line
β_{MP}	Potential width control constant
$\varepsilon_{kl}\ (k, l = 1, 2, 3)$	Strain tensor
$\varepsilon_r, \varepsilon_m$	Average strains
θ_{MP}	Morse potential current angle of the adjacent bond
θ_r	Inclination angle
$\sigma_{LJ}, \varepsilon_{LJ}$	Lennard-Jones parameters
$\sigma_{ij}\ \ (i, j = 1, 2, 3)$	Stress tensor
φ_r	Azimuth angle
Λ	Aspect ratio
A	Cross-sectional area
E	Young's modulus
I	Identity tensor
K	Bulk modulus
L	Side length of representative volume element
M	Moment
N	Axial force
S	Eshelby tensor
T	Torsion
V	Total volume
a, b	Unit vectors
a, b, c	x, y, z components of direction vector

d	Minimum distance between non-coplanar lines
k, l, m, n, p	Hill's elastic moduli
l	Line
n, m	Integers
$p(\alpha, \beta)$	Probability density function in terms of Euler angles
po	Coordinates of point
$ro, k_{\theta-MP}, \theta_o, k_{sextic}$	Modified Morse potential parameters
v	Poisson's ratio
ΔL	Axial stretch
Δr	Bond stretching increment
$\Delta \Phi$	Change of bond twisting
$\Delta \beta$	Torsional rotation angle
$\Delta \theta$	Bond angle change
α	Rotational angle at the ends of the beam
ξ, ζ	Agglomeration parameters
ρ	Vector magnitude

CHAPTER 1

INTRODUCTION

1.1 Overview

World's one of the most important issue is climate change. The increase of greenhouse gases in Earth's atmosphere prevents the escape of excessive heat from Earth which has serious consequences, such as increase in global land and ocean temperature, sea level rise, melting of glaciers, change of extreme weather conditions. The main source of greenhouse gases is the burning of fossil fuels [1]. Currently, transportation is the second largest CO_2 emitting sector in the world (see Figure 1.1) [2].

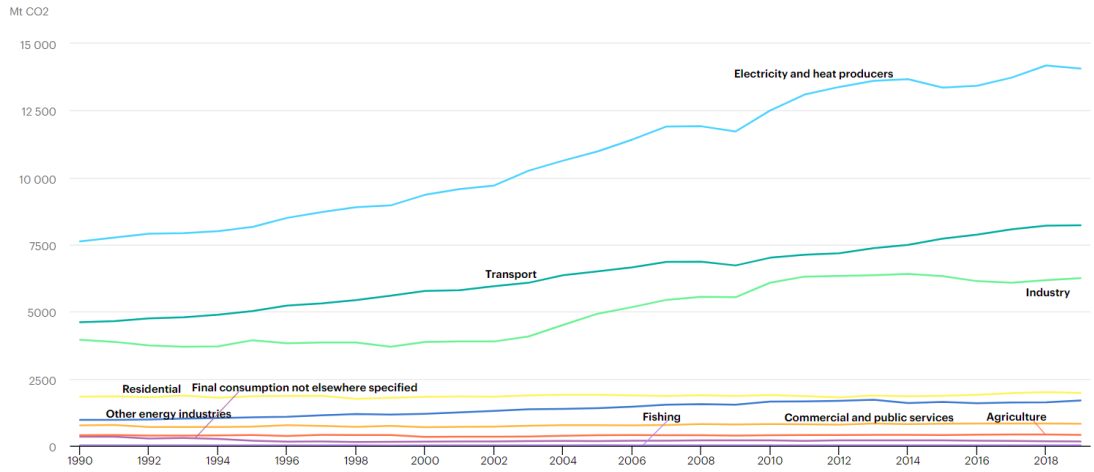

Figure 1.1: Global CO_2 emissions by sector [2].

Transportation makes up one quarter of the direct CO_2 emission from fossil fuel burning and IEA's forecast shows that the trend will not drastically change in the near future (see Figure 1.2) [3].

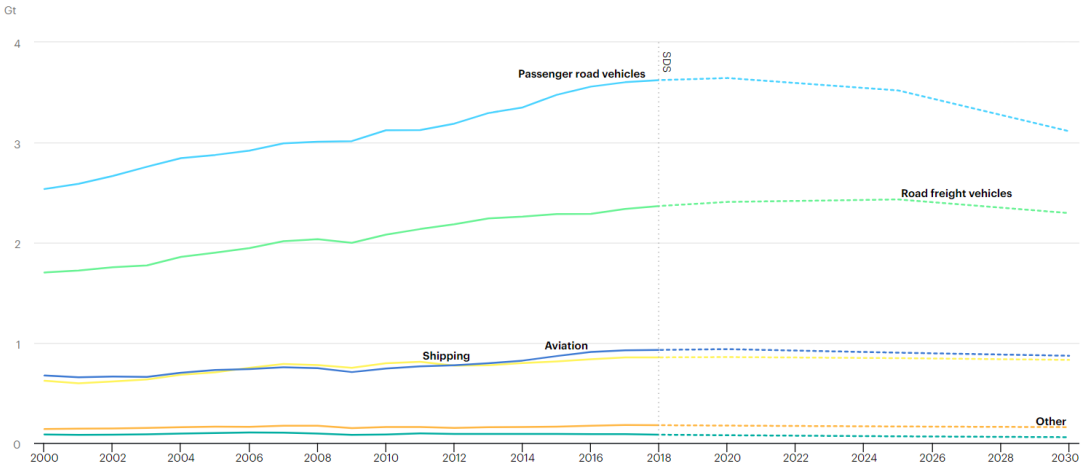

Figure 1.2: Transport sectors CO_2 emissions forecast [3].

The use of lightweight materials will reduce fuel consumption and, as a result, decrease CO_2 emissions. In addition to this, lightweight materials provide better performance. Some of the lightweight materials used are aluminium, magnesium, titanium and composite [4]. Composites have the advantages like having high specific strength and specific modulus, fatigue and corrosion resistance. Reinforcement is responsible for providing strength to the composite and generally fibre reinforcement is used due to its high aspect ratio and strength in axis direction [5]. Experimental and computational studies show that SWNTs have Young's modulus of 1 TPa and failure strain of 15 % [6]. The unprecedented mechanical properties of CNTs have made them a novel fibre reinforcement. Figures 1.3 to 1.6 compares the mechanical properties of CNT with renowned high strength fibres. The values are taken from references: [5]–[8].

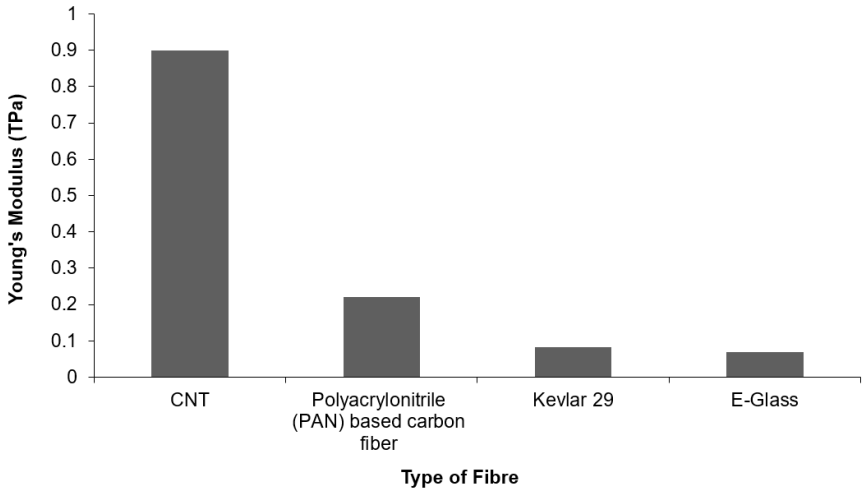

Figure 1.3: Young's modulus comparison of various fibre reinforcements [5]–[8].

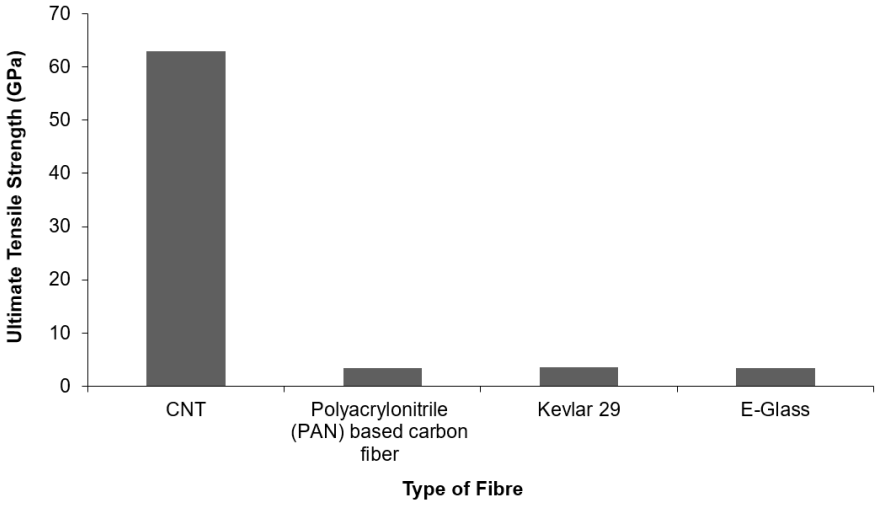

Figure 1.4: Ultimate tensile strength comparison of various fibre reinforcements [5]–[8].

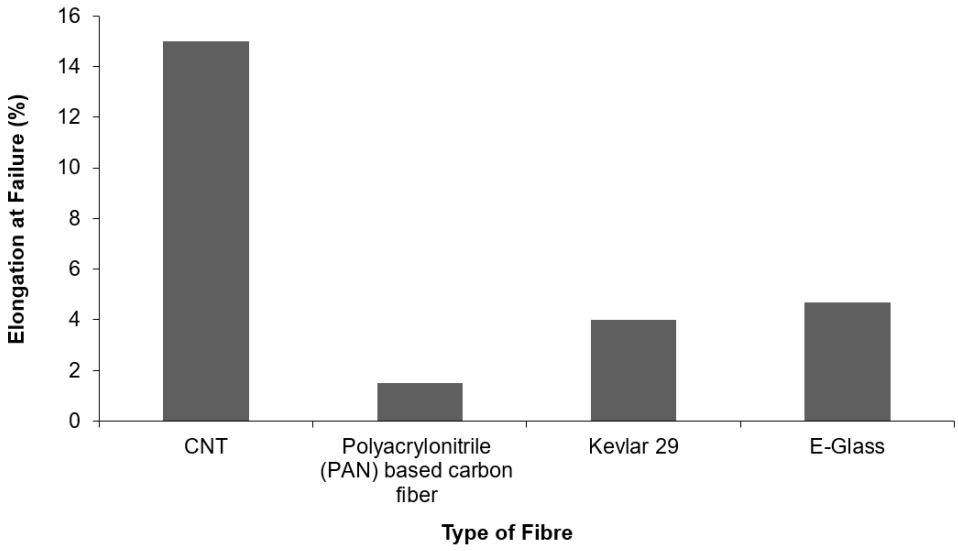

Figure 1.5: Failure strains of various fibre reinforcements [5]–[8].

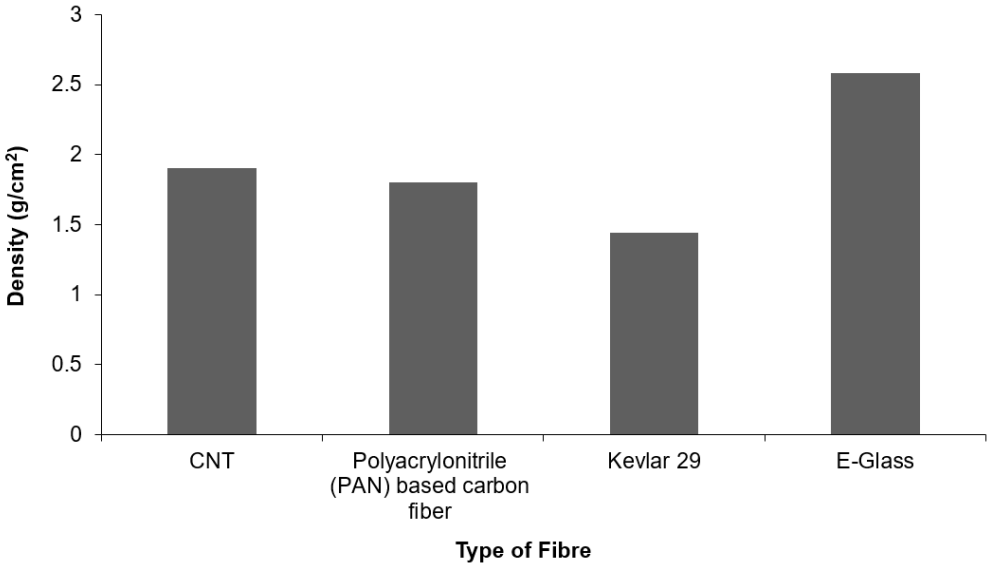

Figure 1.6: Area densities of various fibre reinforcements [5]–[8].

Figures 1.7 and 1.8 show the huge difference in mechanical properties of CNT and other engineering materials.

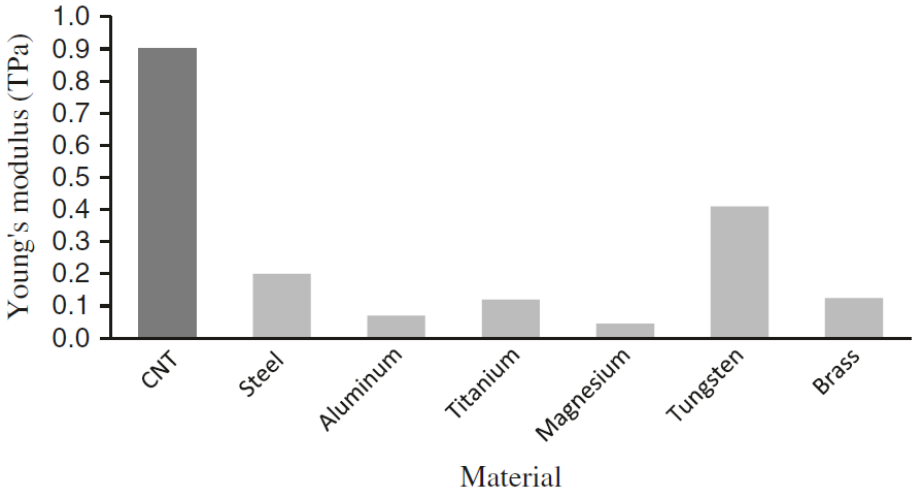

Figure 1.7: Average Young's modulus of CNT and widely used engineering materials [7].

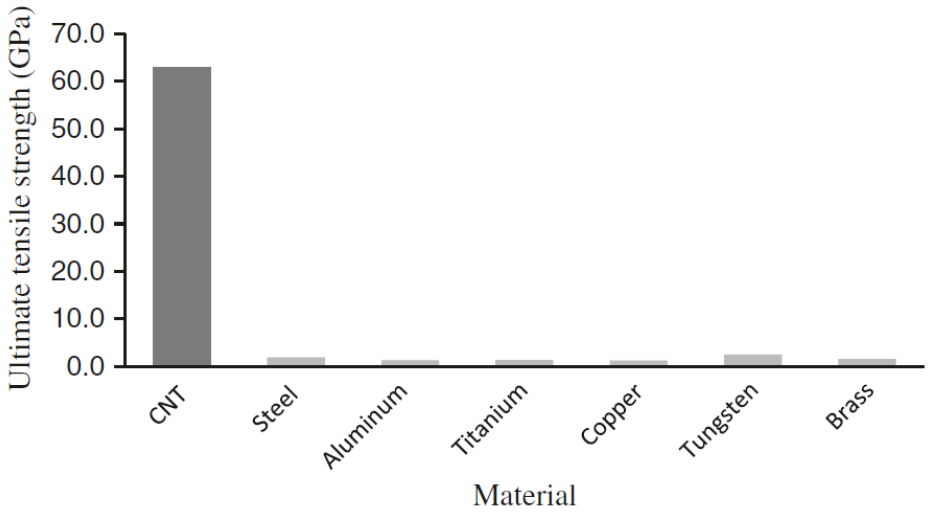

Figure 1.8: Average ultimate tensile strength of CNT and widely used engineering materials [7].

CNT reinforced composites (CNTRCs) have high specific strength and modulus and can be utilized in fields like aerospace, automotive and marine structures [9]. Tensile tests made by Deplancke et al. showed that 10 % (mass fraction) addition of CNT into polymer increased its tensile strength and Young's modulus by 37 % and 20 % respectively [10]. CNTs also possess high electrical conductivity which is an important feature for electronic industry. The research on high strength and electrical conductor composites such as CNT reinforced metal matrix composites is still developing and the future applications are expected to be nanonetworks, nanorobotics and future soldiers [9]. BMC Switzerland manufactured the first bicycle whose framework is made of CNTRC (see Figure 1.9).

Figure 1.9: Bicycle whose framework is made of CNTRC [11].

Researcher Marcio Loos manufactured world's first CNT reinforced polyurethane wind turbine (see Figure 1.10). Improved fatigue resistance is obtained [11].

Figure 1.10: Wind blades made of CNTRP [11].

1.2 Motivation

Several experimental research studies have been conducted to determine the mechanical properties CNTRPs, however results have not been conclusive. FEAs of CNTRP can provide insights into the parameters affecting the mechanical properties of CNTRPs.

1.3 Aims and Objectives

There is a paucity of research on the meso-scale mechanical properties of CNT reinforced epoxy composite. This study aims to understand how embedded CNTs' properties affect the meso-scale mechanical properties of CNTRP. The investigated parameters include CNT orientation, volume fraction, end-structure (blunt-capped) and curvature (for CCNT case).

1.4 Contents

Chapter 1 points out the importance of lightweight materials, then compares mechanical properties of CNT with other materials. The initial applications of CNTRP are introduced and lastly, the aim and objective of this thesis is expressed.

Chapter 2 makes a comprehensive review of literature about CNT, CNTRP, their fabrication, safety, testing, and FE and analytical micromechanics models. This chapter ends with the determined gaps in the literature.

Chapter 3 explains the in-house developed C++ code in detail and provides information about the developed FE model.

Chapter 4 displays the FEA results and micromechanics models on line and bar graphs. In addition to this, verbal explanation of results is made.

Chapter 5 sums up the findings of this study, evaluates the correctness of results, indicates the limitations of FEA and makes recommendations for future studies.

CHAPTER 2

LITERATURE REVIEW

2.1 What Is Nanomaterial?

Nanomaterials are classified into two groups as nano-object and nanostructured material. A nano-object is an individual material which has at least one of its dimensions in the range between 1 nm and 100 nm. This range is also called as nanoscale. On the other hand, a nanostructured material has outer dimensions above the nanoscale but contains nano-object(s) inside it. A nano-object may have internal nanostructure but it is still classified under nano-object [12].

2.2 Carbon Nanotubes

2.2.1 Brief History of Carbon Nanotubes

Most of the researchers believe that Japanese scientist Sumio Iijima invented carbon nanotubes (CNTs) in 1991 [13]. Nevertheless, it is still a controversial topic among researchers because there are claims that Radushkevich and Lukyanovich discovered the hollow carbon filaments with nanoscale diameter in 1952 [14] and Oberlin et al prepared hollow carbon fibres in 1976 which also had nanoscale diameter and shared images taken by high resolution transmission electron microscopy (HRTEM) [15]. Iijima's work in 1991 has dramatically increased the interest and speeded up the research on CNTs and in the following years CNTs' exceptional mechanical, electronic and thermal properties have been discovered [16].

2.2.2 Molecular Structure of CNT

Carbon nanotubes are purely composed of carbon atoms like diamond, graphite and buckminsterfullerene. Although they are all made of carbon atoms they have different bonding structures which makes them allotropes [17]. In CNT and graphene structure, each carbon atom makes two single and one double bond with the three neighbouring carbon atoms, thus each carbon atom has one delocalised electron. This bonding structure forms a honeycomb like lattice. CNTs, as its name would suggest, has a hollow cylinder (tube) structure. If this tube is cut imaginatively from one end to the other and laid on a flat surface it will form the same structure as graphene. Graphene is a 2D material

and CNT is the tubular and 1D form of graphene (see Figure 2.1) [18]. Length to diameter ratio of a fibre is called aspect ratio [5] and CNTs can have aspect ratio as high as 132 million [9].

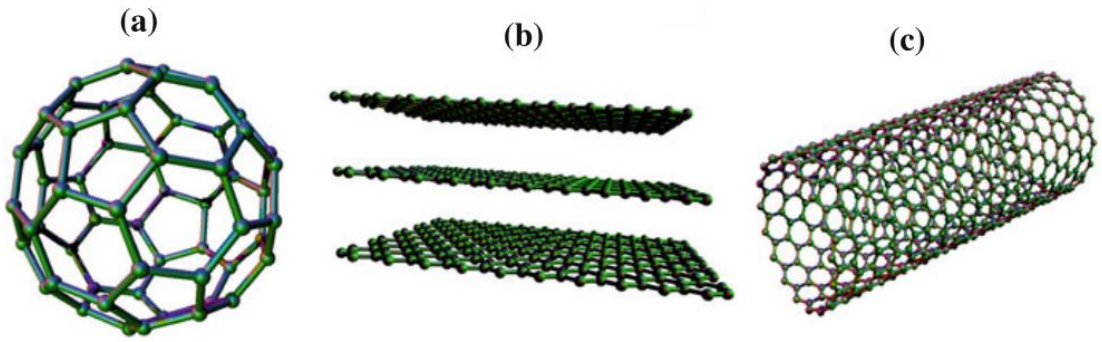

Figure 2.1: (a) C_{60} spherical fullerene, (b) Graphite, (c) CNT [19].

In graphene and CNT, each carbon atom forms sp^2 hybridization. sp^2 hybridization is formed by the mixture of one *s* orbital and two *p* orbitals. Bonds between carbon atoms has 120° angle with each other. This type of bonding generates σ and π bonds. CNTs owe their high mechanical properties to σ-bonds. In addition to σ-bonds, weaker π-bonds arise due to the unhybridized *p* orbitals that exists above and below σ-bond. σ-bonds contribute to the in-plane forces where as π-bonds contribute to the out of plane forces (see Figure 2.2) for instance, forces between CNT bundles and forces between concentrically located CNTs (also known as MWNTs). σ and π bonds rehybridize by virtue of curved tube structure of CNT [18].

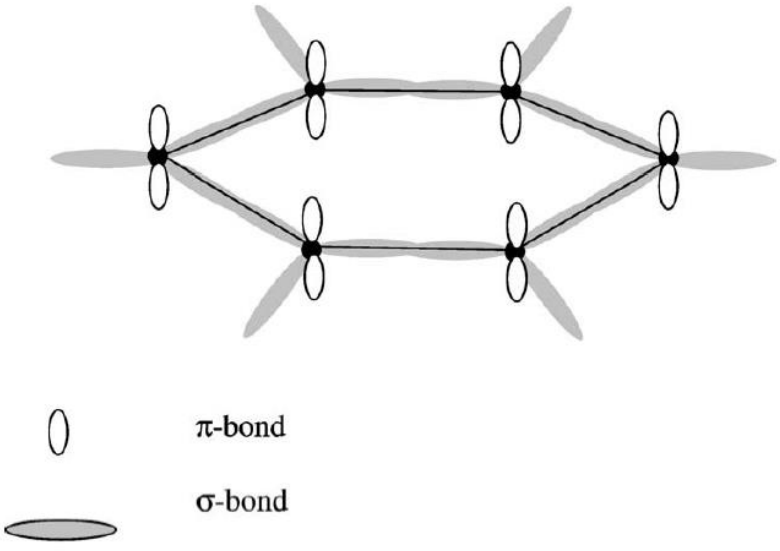

Figure 2.2: Hexagonal bonding structure of CNT showing σ and π-bonds [18].

2.2.3 Types of CNTs

There are mainly three types of CNTs which are single walled CNT (SWNT) and multi walled CNT (MWNT) and defective CNT [20].

SWNT consists of a single CNT while MWNT is made up of two or more SWNTs which are located concentrically like old maritime telescope (see Figures 2.3, 2.4 and 2.5).

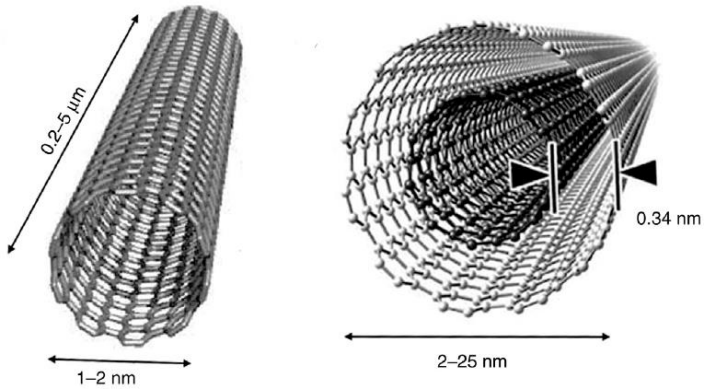

Figure 2.3: Illustration of SWNT and MWNT with dimension ranges [16].

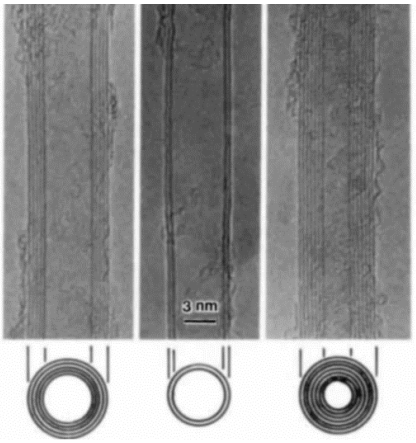

Figure 2.4: Electron micrographs of the most renowned MWNTs [13].

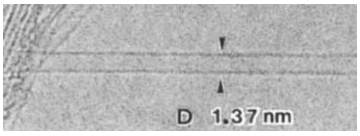

Figure 2.5: Electron micrograph of SWNT published in 1993 [21].

In the literature there are two models for MWNT which are Russian Doll model and Parchment model. Russian Doll model assumes multiple SWNT with different diameters are located concentrically with certain distances between them while Parchment model which is published in 1960 presumes that a single graphene layer rolls to form MWNT (see Figure 2.6) [19], [22].

Figure 2.6: Illustration of Parchment model [22].

Helical or coiled CNT (CCNT) and Y-junction CNT are examples of defected CNTs. They are created when carbon bonds in CNT form pentagonal and heptagonal bonding shapes (rings) in addition to hexagonal network. These defects in CCNTs cause it to bend and become coiled (see Figure 2.7). CCNTs have both multi-walled and single-walled types [23].

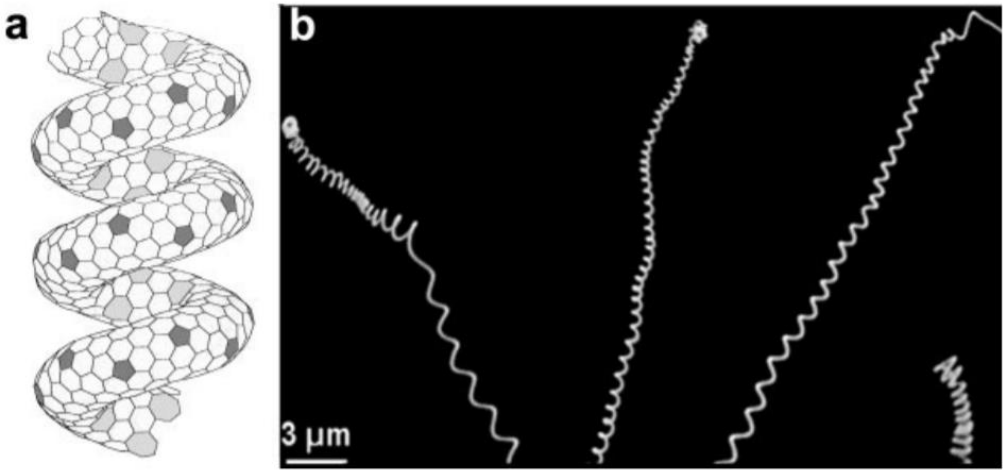

Figure 2.7: (a) Depiction of CCNT with pentagonal and heptagonal bonding defects (b) Images of CCNTs resembling corkscrew [24].

CNTs can have either open-blunt ends or capped-closed ends. CNTs with the same radius can have different cap structures. Capped ends are formed from hemi-fullerenes (see Figure 2.8) [25].

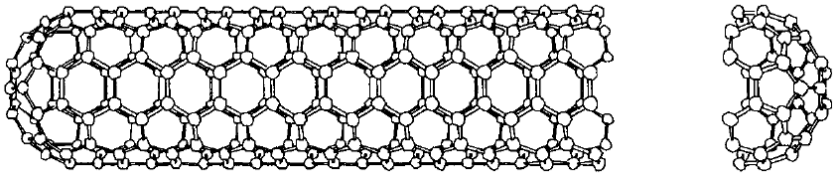

Figure 2.8: Schematic diagram of closed end (capped) CNT [25].

2.2.4 Chirality of CNT

SWNTs are classified with respect to their chirality or in other words helicity. Chiral vector (Ch) is defined as the vector drawn from one side of the graphene sheet to the other. When the graphene sheet is rolled imaginatively to form SWNT the start and end points of Ch match (see Figure 2.9).

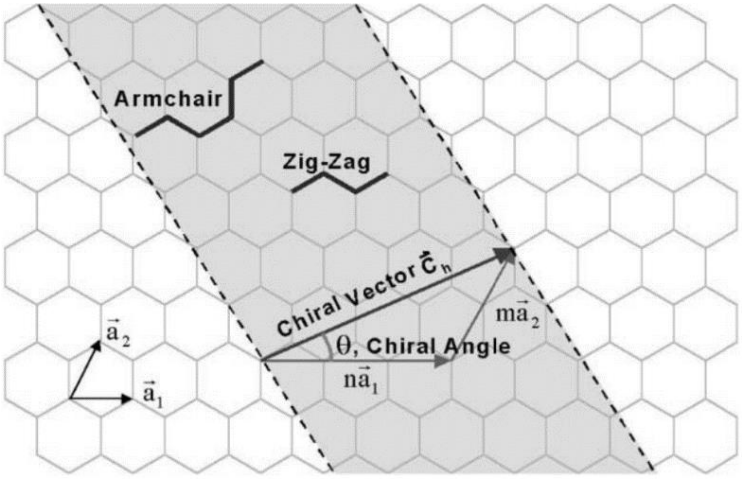

Figure 2.9: Depiction of graphene sheet with chiral vector and angle [26].

Chiral vector equation is [16]:

$$C_h = na + mb \tag{2.1}$$

a and b are unit vectors (see Figure 2.10) and n and m are integers. Chiral angle C_θ is the angle between vector Ch and vector a. There are three types of chiralities which are zigzag when $m = 0$, armchair when $n = m$ and chiral when $m \neq n \neq 0$ (see Figure 2.11) [16], [18].

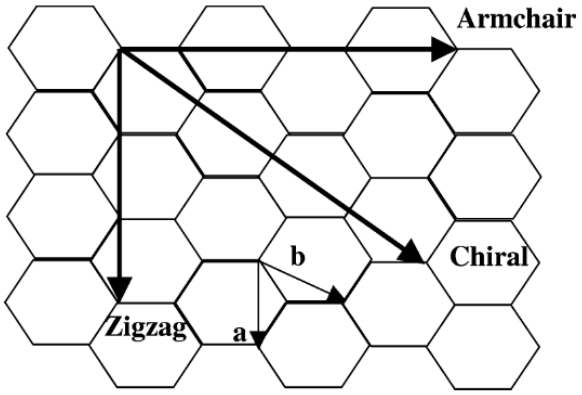

Figure 2.10: Chiral vector and unit vectors a and b [18].

Carbon nanotube diameter (d_{CNT}) is calculated by Equation 2.2 [16]:

$$d_{CNT} = \frac{|C_h|}{\pi} = \frac{\sqrt{3} * L}{\pi}(m^2 + mn + n^2)^{\frac{1}{2}} \tag{2.2}$$

L is C-C bond length which is equal to 0.142 nm. Chiral angle (C_θ) is calculated by the below equation [16]:

$$C_\theta = \tan^{-1}\left(\frac{\sqrt{3}\, m}{m + 2n}\right) \tag{2.3}$$

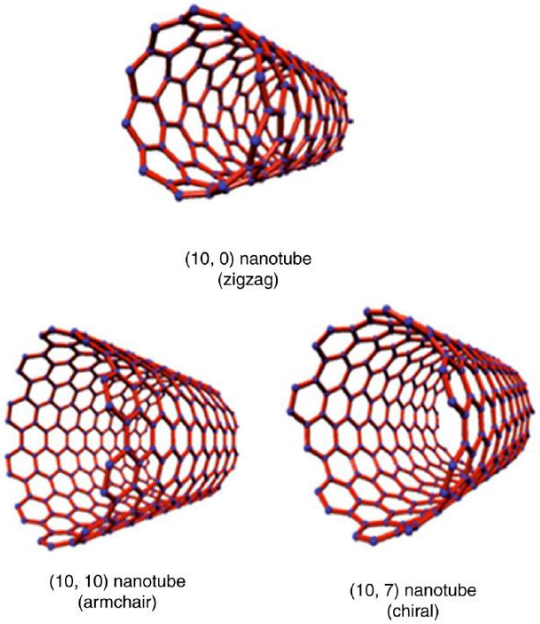

Figure 2.11: Molecular models of zigzag, armchair and chiral SWNTs [27].

SWNTs that make a MWNT can have different chiralities. If the MWNT is constituted from only one type of chirality it is called monochiral MWNT but if it is made up of SWNTs with different chiralities then it is named as polychiral MWNT [28].

2.2.5 Synthesis of CNTs

2.2.5.1 Arc Discharge Evaporation Method

Iijima produced high quality MWNTs in 1991 by arc discharge evaporation method [13]. The most common apparatus used for this method is stainless steel vacuum chamber (see Figure 2.12). Arc discharge method is similar to Krätschmer–Huffman technique which is used for synthesizing C_{60} fullerene. In Krätschmer–Huffman technique anode and cathode touches each other but in arc discharge evaporation method electrodes are held distant. In arc discharge method, initially inert gases such as He or H_2 flows continuously inside the chamber with an optimum pressure of 500 torr. 20 V DC power supply is used for charging electrodes. At the beginning electrodes made of graphite are positioned distant so current do not flow between electrodes. Then anode electrode is gradually brought closer to cathode until a stable arc is created and anode is kept stable at this position. Anode heats up due to electron bombardment and evaporates progressively. Fullerene soot condenses and deposits on cathode and on the inner surface of the chamber. CNTs are present inside the deposit on cathode. The

aforementioned method is used for MWNT production, for SWNT production ferromagnetic metal (for example, Co-Y, Ni-Y or Ni-Co) impregnated graphite electrodes must be used rather than pure graphite electrodes. This method produces CNTs with lesser defects than CVD method (see Section 2.2.5.3) but the CNTs are entangled, have non-uniform lengths and require further purification and this method not suitable for large scale production [29]–[31]. Figure 2.13 depicts the formation of MWNTs by arc discharge evaporation method.

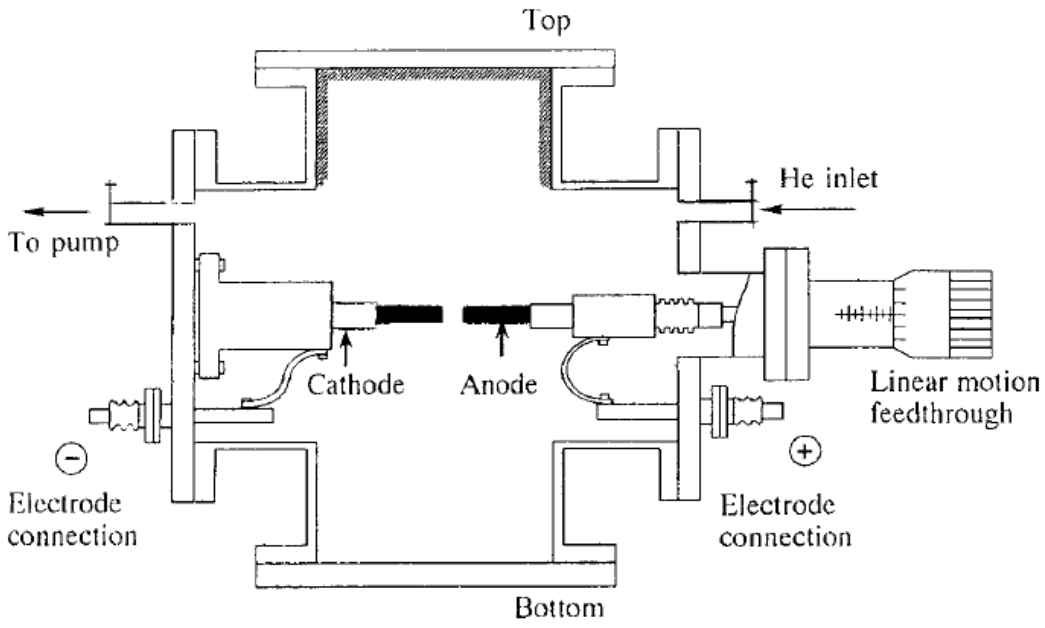

Figure 2.12: Schematic illustration of arc evaporation chamber [29].

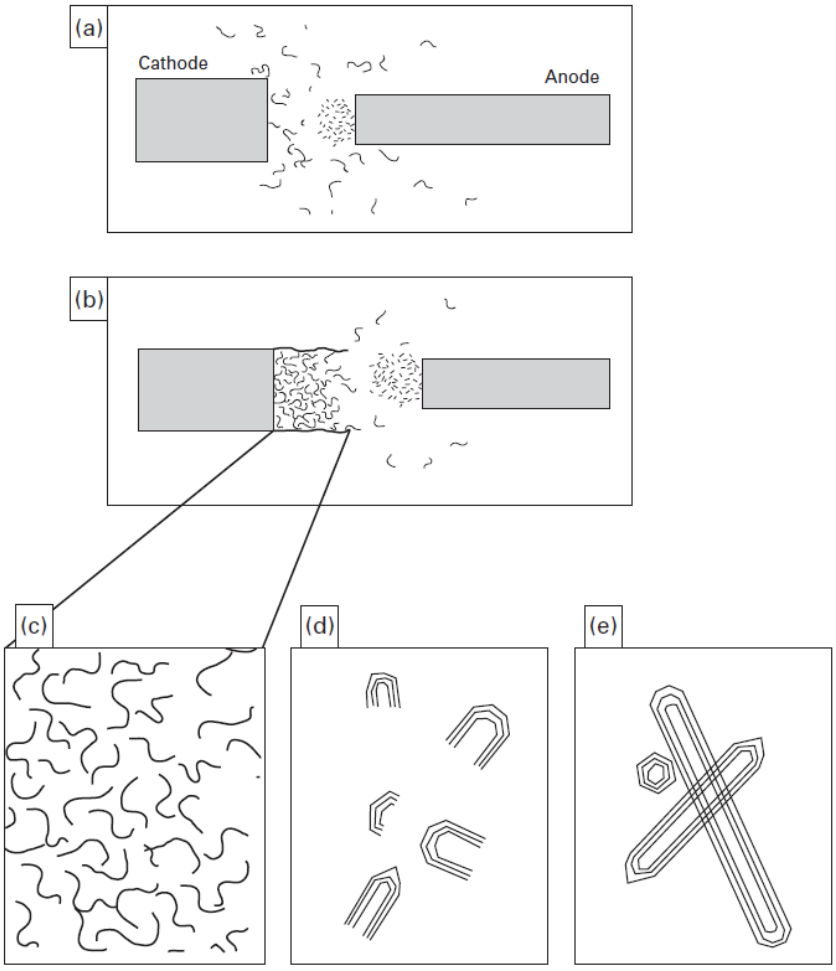

Figure 2.13: Progressive formation MWNTs by arc discharge evaporation method [29].

2.2.5.2 Laser Ablation (Vaporisation) Method

Both SWNTs and MWNTs are produced by utilizing this method. Figure 2.14 shows schematic representation of laser vaporisation apparatus. The quartz tube furnace is heated up to 1200 °C and Ar gas flows inside the furnace with a constant pressure of 500 torr. Neodymium yttrium aluminium garnet laser (Nd: TAG laser) is used to evaporate cylindrical graphite target. Evaporated substances are carried to the water-cooled copper collector with the flow of Ar gas. CNTs deposit on water cooled copper collector. In order to synthesize SWNT, graphite target must be enriched with metal catalysts, for instance Co and Ni. This method has the drawbacks of expensive laser equipment, high energy consumption and CNTs require purification after synthesis. However, it produces very high quality CNTs in large scale [20], [29], [31]–[33].

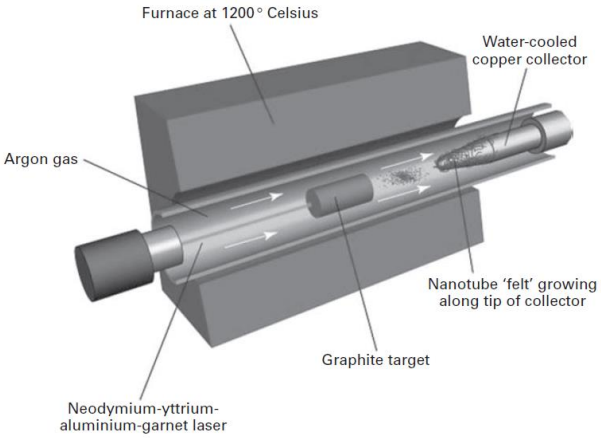

Figure 2.14: Schematic representation of laser vaporisation apparatus [29].

2.2.5.3 Catalytic Chemical Vapour Deposition (CVD) Method

Catalytic chemical vapour deposition method is suitable for large scale production of SWNTs and MWNTs [20] and it is especially preferred in areas like electronics and optoelectronics [34]. Methane, acetylene and carbon monoxide gases are used as carbon source. Thermal source or plasma is used for decomposing carbonous gas. Dissociated carbon atoms nucleate and grow on catalyst covered substrate and form CNTs. Fe, Co, Ni and V are some of the catalysts used. Catalyst particle size is an important feature, for instance large catalyst particles are used for MWNT synthesis [20], [34]. Generally, this method produces highly defected CNTs [35]. However, this method requires lower temperature than other methods which makes this method cost effective [30] and capable of producing large amount of CNTs and CNTs can be aligned vertically [31]. Figure 2.15 shows a schematic view of a type of catalytic vapour deposition reactor.

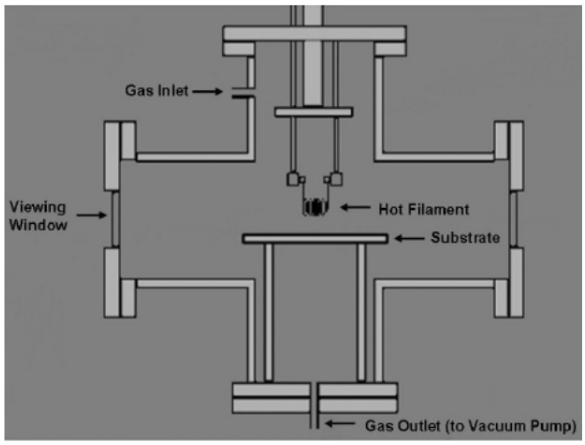

Figure 2.15: Scheme of a hot filament catalytic vapour deposition reactor [34].

2.2.6 Defects in CNTs

Pristine CNTs have exceptional mechanical properties but the defects in CNTs have detrimental effects on its mechanical properties such as Young's modulus, tensile strength and tensile failure strain [36]–[38]. Sometimes presence of defects is inevitable. CNT synthesis and chemical functionalization are some of the reasons of formation of defects [39].

2.2.6.1 Vacancy Defect

Vacancy defects occur after CNT synthesis [40] or functionalization process (see Section 2.3.4) [39]. When one (monovacancy) or two (divacancy) carbon atoms are removed from the regular hexagon pattern, the bonds that used to make connection with the dislocated carbon atom become dangling bonds. Dangling bonds either rehybridize or connect with the molecules nearby. Figure 2.16 shows vacancy defects before and after reconstruction [40].

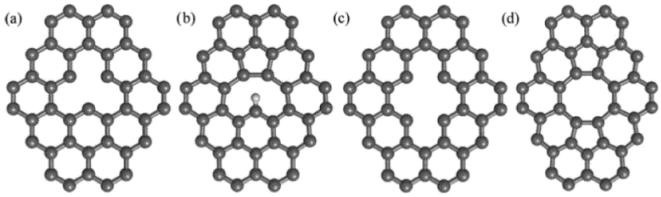

Figure 2.16: Monovacancy (a) before and (b) after reconstruction

Divacancy (c) before and (d) after reconstruction [40].

2.2.6.2 Stone-Wales Defect

In this type of defect, four neighbouring hexagonal bonds convert into two pentagon and two heptagon bonds and forms a 5-7-7-5 configuration (see Figure 2.17). Stone-Wales defect does not change the topology of CNTs [40], [41].

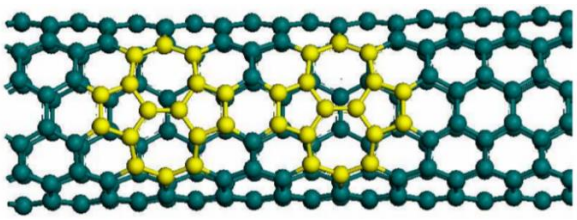

Figure 2.17: Two Stone-Wales defects on a SWNT [42].

2.2.7 Engineering Applications of CNTs

Apart from structural composites (see chapter 1 for structural composite applications), CNTs are also used in fields like coating and films, sensors, electromagnetics and biotechnology.

Marine current turbines are coated with CNTs to prevent biofouling. CNTs have hydrophobic property which prevents adhesion of algae and barnacles [9]. CNTs possess superior electrical conductivity and semi-conductivity features [25] which makes them suitable for sensor applications. Researchers from the University of Delaware developed new sensors made of CNT containing coatings (see Figure 2.18). These sensors have extremely wide pressure sensing range which can be as little as a gentle touch of a finger or as high as the crush of a forklift [43]. Thin CNT composite films are also used for structural health monitoring [44]. Park et al. showed that CNT-reactive ethylene terpolymer (RET) has excellent microwave shielding efficiency which can be used in electromagnetic interference (EMI) applications [45]. Some of the medical applications of CNTs are cancer and infection therapy, biosensor vehicles for diagnostics and detection, and gene therapy by DNA delivery [9].

Figure 2.18: A thin sensor made of CNTRC placed inside a shoe to measure foot pressure [43].

2.3 Manufacturing of CNTRP

Various methods are available in the literature for CNTRP fabrication, such as melt mixing, solution mixing, sonication, resin transfer molding, bucky paper resin infiltration, aligned CNT sheet process, shear mixing melt processing and *in situ* polymerization [31]. Only the three methods are explained in this thesis, further information can be found in the review paper of Nurazzi et al. [31].

2.3.1 Solution Mixing

Solution mixing is the most widely used technique for CNTRP fabrication. CNTs, solvent and polymer are agitated by mechanical/magnetic stirring, sonication or high shear mixer, then solvent is evaporated to form CNTRP [29], [31].

2.3.2 Melt Processing

Thermoplastic polymer is melted and blended with CNTs in the extruder (see Figure 2.19). Solvent is not used in this process. This method is easy, fast, cheap, environmentally friendly and high volume CNTRP part can be fabricated. The downside is the difficulty in mixing because of high viscosity of mixture. To handle this high shear mixer is used and this can damage CNTs while mixing (CNTs can be cut into smaller pieces) [29], [31].

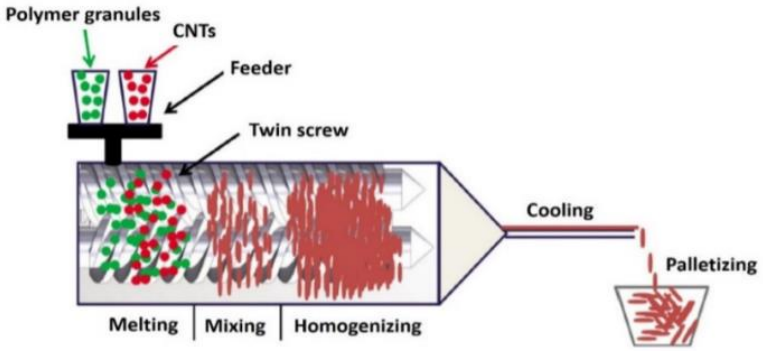

Figure 2.19: Illustration of micro-compounder [31].

2.3.3 *In Situ* Polymerization

Initially, CNTs are mixed with monomers instead of polymer, then the polymerization procedure is executed. This technique is preferred if the polymer is insoluble and solution mixing and melt processing methods cannot be applied. Moreover, good dispersion and strong CNT-polymer interface is achieved in this process. On the other hand, viscosity builds-up during process [29], [31].

2.3.4 Chemical Functionalization of CNTs

CNT tips and sidewalls can be functionalized chemically while manufacturing CNTRP to make the bonding between CNT and polymer stronger and improve the dispersion of CNTs in matrix by increasing the solubility of CNTs in polymer solution [29], [46]. This process has the disadvantage of causing defects in CNTs [39].

2.4 Macro-Scale Mechanical Testing of CNTRP

Macroscopic mechanical properties of CNTRP can be measured by various experiments. The results of these experiments must be comparable to other experiments available in the literature. In order to attain this, norms set by international standards must be applied. The norms include test specimen dimensions and tolerances, testing apparatus, measuring devices, procedure, number of test specimens, environmental conditioning, calculations and reporting.

Some of the standards convenient for measuring tensile, bending and impact properties of CNTRP are ASTM D638-14 [47], ASTM D790-17 [48], ASTM D6272-17e1 [49], ASTM D6110-18 [50] and ASTM D256-10 (Reapproved 2018) [51]. Interested readers may refer to these standards for more detailed information.

2.5 Occupational Health and Safety While Working on CNTs

2.5.1 CNT Toxicity and Potential Health Problems Caused Due to Exposure

A number of *in vivo* and *in vitro* studies are available in the literature which investigated the potential diseases that could be caused because of CNT exposure. However, *in vivo* studies are merely limited to experiments on rodents. Nonetheless, present studies show that CNT exposure may cause serious illnesses and suggest minimizing CNT exposure [52].

CNTs can cause health problems because they are in nanoscale and fibre shaped with very high aspect ratio just like asbestos fibres. Furthermore, it is biopersistent which is associated with its graphitic structure [53]. CNTs which are synthesized by employing catalysts stores metal impurities and these impurities can also contribute to the toxicity of the nanomaterial. Surface modification or functionalization alters the chemical structure of CNT and increases the level of toxicity [54].

The most dangerous CNT exposure route is inhalation [54]. Murray et al. conducted experiments on mice and compared the effects of pulmonary exposure to SWNT, nanofibre (NF) and asbestos. Exposure to these nanomaterials caused inflammation, pulmonary damage, fibrosis and oxidative stress in the

lungs of mice. Among these three nanomaterials SWNT induced more severe problems [55]. In the study of Porter et al. granulomatous inflammation occurred in the lungs of a mice after being exposed to MWNTs [56]. Takagi et al. stated in their research that MWNT is carcinogenic and cause mesothelioma [57]. Saber et al. performed *in vivo* experiments in the lungs of mice and compared CNT containing epoxy composite dusts with neat epoxy dusts and both of them revealed similar responses like inflammation and DNA damage in the lung tissue [58].

Koyama et al. injected SWNT and MWNT under the skin of mice and found out that granulomas are formed under the skin after injection [59]. In the study of Mohanta et al., it is indicated that CNTs also cause liver, central nervous system, kidney, cardiovascular, spleen and eye (ocular) toxicities [60].

2.5.2 Engineering Controls

CNTs can be processed in different forms such as powder, slurry or embedded in matrix. The amount of CNT handled and the production procedure followed varies from factory to factory and from factory to research laboratory. Different engineering controls are used considering the aforementioned conditions. For example, grinding or cutting CNTRP easily makes CNTs airborne thus, local exhaust ventilation (LEV), ventilated downflow booths with HEPA filter exhausts and wet cutting techniques should be applied. If CNTs are handled in research laboratories and operations like weighing, mixing, blending, transferring small amount of CNT is being done then using laboratory fume hood, glove box isolator or biological safety cabinet class 2 with HEPA filtered exhaust is more appropriate [52], [61].

2.5.3 Personal Protective Equipment (PPE)

If all the engineering control measures are implemented but still it is insufficient then PPE should be used. PPE is only capable of protecting the person who wears it not the others. The user should know how to use and store PPE and they should also wear and test the PPE before using it. Damaged PPE is no longer protective and the person who wears it is vulnerable to nanomaterial exposure [61].

PPE mainly consists of respirator, protective clothing, gloves, safety goggles and impermeable shoes.

2.5.4 Further Reading About Safe Use of CNTs

General hygiene, safe disposal, correct respirator selection, health screening and surveillance, and many other important information about safe handling of CNTs can be found in references: [52], [61]–[67].

2.6 Multiscale Modelling of CNTRP

Hierarchical multiscale modelling approach is explained in this section. This method is computationally reasonable and also takes into account the nano-scale properties of CNTRP [68]. It has four length scales which are nano, micro, meso, and macro (see Figure 2.20) [69], [70].

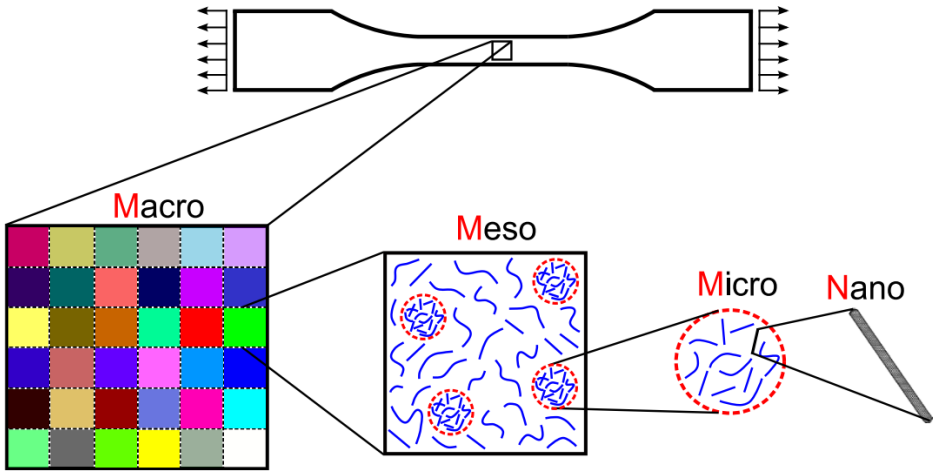

Figure 2.20: Multiscale modelling scheme [71].

2.6.1 Nano-Scale Model

At nano-scale various models have been introduced. Some of them utilized molecular dynamics (MD) [72] and *ab initio* methods which are limited to small time and length scales due to their high computational costs [73]. In this section various models which make a linkage between molecular mechanics and structural mechanics are explained. These methods are computationally cheaper compared to MD and *ab initio* methods.

CNTs are composed of carbon atoms and the motion of these atoms are controlled by force field. Force field is caused by nucleus-nucleus and nucleus-electron interactions. Force field is defined in terms of steric potential energy. Equation 2.4 shows the total steric potential energy which includes bonded and non-bonded interactions while disregarding electrostatic interaction [74].

$$U = \sum U_r + \sum U_\theta + \sum U_\Phi + \sum U_\omega + \sum U_{vdw} \tag{2.4}$$

where U_r is bond stretching, U_θ is bond angle bending, U_Φ is dihedral angle torsion, U_ω is out of plane torsion and U_{vdw} is non-bonded van der Waals interaction energies. In covalent systems the contribution of van der Waals interaction is negligible and, consequently, this term is omitted. Steric potential energy

can be characterized by harmonic approximation for simplification. This method is limited to small deformation only. See Equation 2.5 for harmonic form of steric potential energy. Note that U_{Φ} and U_{ω} are summed into one term U_{τ} [74].

$$U_r = \frac{1}{2}k_r(r - r_0)^2 = \frac{1}{2}k_r(\Delta r)^2$$
$$U_\theta = \frac{1}{2}k_\theta(r - r_\theta)^2 = \frac{1}{2}k_\theta(\Delta\theta)^2$$
$$U_\tau = U_\Phi + U_\omega = \frac{1}{2}k_\tau(\Delta\Phi)^2 \quad (2.5)$$

where k_r, k_θ, and k_τ are the bond stretching force constant, bond angle bending force constant and torsional resistance respectively and Δr, $\Delta\theta$ and $\Delta\Phi$ refer to bond stretching increment, bond angle change, and angle change of bond twisting, respectively. Li and Chou [74] established a connection between molecular mechanics and structural mechanics (see Figure 2.21). They represented C-C bonds with circular cross sectioned beam elements. The structural properties of beam elements are obtained by equalising steric potential energies to strain energies of uniform beam. Equation 2.6 shows beam strain energies for different loading conditions which are pure axial, pure bending and pure torsion, respectively and Equation 2.7 shows relation between force constants and beam's mechanical properties [74].

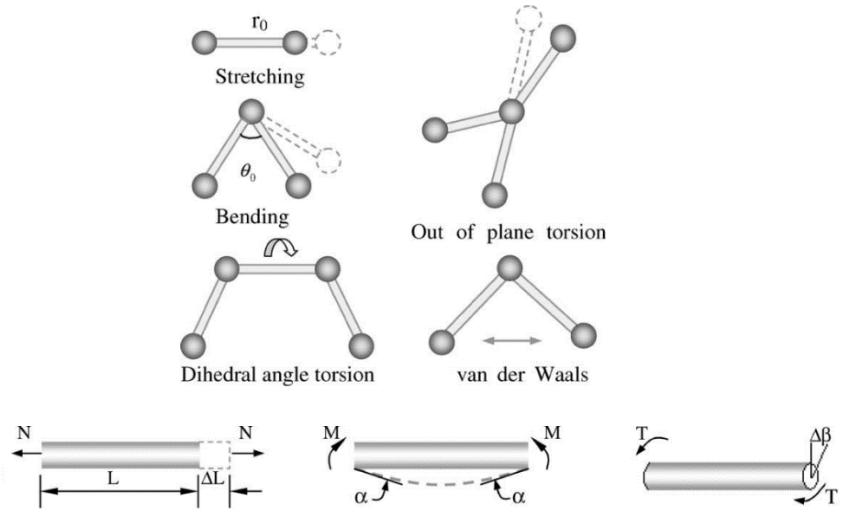

Figure 2.21: Linkage between molecular mechanics (top) and structural mechanics (bottom) [74].

$$U_A = \frac{1}{2}\int_0^L \frac{N^2}{EA}dL = \frac{1}{2}\frac{N^2 L}{EA} = \frac{1}{2}\frac{EA}{L}(\Delta L)^2$$
$$U_M = \frac{1}{2}\int_0^L \frac{M^2}{EI}dL = \frac{2EI}{L}\alpha^2 = \frac{1}{2}\frac{EI}{L}(2\alpha)^2$$
$$U_T = \frac{1}{2}\int_0^L \frac{T^2}{GJ}dL = \frac{1}{2}\frac{T^2 L}{GJ} = \frac{1}{2}\frac{GJ}{L}(\Delta\beta)^2 \quad (2.6)$$

where ΔL, α and $\Delta\beta$ are axial stretch, rotational angle at the ends of the beam and torsional rotation angle [74].

$$\frac{EA}{L} = k_r$$
$$\frac{EI}{L} = k_\theta$$
$$\frac{GJ}{L} = k_\tau \quad (2.7)$$

Weak van der Waals interaction between CNT and polymer matrix are defined by Lennard-Jones potential. These non-covalent bonds can be represented by nonlinear spring or truss elements. Equation 2.8 and 2.9 show the energy and force on these spring elements, respectively [75].

$$V_{LJ} = 4\varepsilon\left[\left(\frac{\sigma}{r}\right)^{12} + \left(\frac{\sigma}{r}\right)^{6}\right] \quad (2.8)$$

$$F_{LJ} = \frac{dV(r)}{dr} = \frac{4\varepsilon}{r}\left[-12\left(\frac{\sigma}{r}\right)^{12} + 6\left(\frac{\sigma}{r}\right)^{6}\right] \quad (2.9)$$

where σ_{LJ} (= 0.365 nm) and ε_{LJ} (= 0.1102 kcal/mol) are Lennard-Jones parameters and r_{LJ} is the distance between atoms [68], [75].

When the carbon atoms get too close, they start to repel each other and the Lennard-Jones forces reach to infinity. Critical distance (0.43266 nm) is the distance where attraction force is maximum. If the distance between atoms gets too far, attraction force approaches to zero. Figure 2.22 shows Lennard-Jones force versus distance between atoms. Negative force means repulsion while positive force means attraction [75].

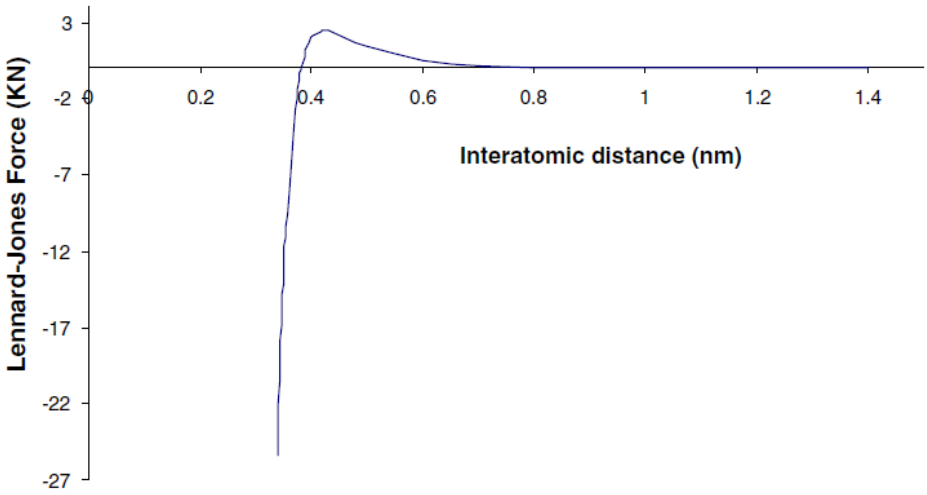

Figure 2.22: Lennard-Jones force versus distance between atoms [75].

Wernik and Meguid [76] constructed a different nano-scale model for representing carbon bonds with structural elements. Their model utilized Morse interatomic potential which has the advantage of taking into account fracture in CNT. Morse interatomic potential is composed of bond stretching and angle bending components (see Equations from 2.10 to 2.12) [76].

$$E_{MP} = E_{MP-s} + E_{MP-b} \tag{2.10}$$

$$E_{MP-s} = D_e \left(\left[1 - e^{-\beta_{MP}(r_{MP} - ro)} \right]^2 - 1 \right) \tag{2.11}$$

$$E_{MP-b} = \frac{1}{2} k_{\theta-MP} (\theta_{MP} - \theta_o)^2 [1 + k_{sextic} (\theta_{MP} - \theta_o)^4] \tag{2.12}$$

where r_{MP}, θ_{MP}, D_e and β_{MP} are current bond length, current angle of the adjacent bond, dissociation energy and potential width control constant, respectively [76]. Table 2.1 presents the Morse potential parameters which are taken from Belytschko et al [77].

Table 2.1: *Modified Morse potential parameters* [77].

Parameter	Value
ro (m)	1.421 x 10^{-10}
D_e (N.m)	6.03105 x 10^{-19}
β_{MP} (m^{-1})	2.625 x 10^{10}
θ_o (rad)	2.094
$k_{\theta-MP}$ (N.m.rad^{-2})	0.876 x 10^{-18}
k_{sextic} (rad^{-4})	0.754

Taking derivative of bond stretching and angle bending components with respect to bond length change and change in rotation, respectively give force required to stretch C-C bond (see Equation 2.13) and moment required to bend neighbouring bonds (see Equation 2.14).

$$F = 2\beta_{MP}D_e\left(1 - e^{-\beta_{MP}\varepsilon_{MP}r_{MP}}\right)e^{-\beta_{MP}\varepsilon_{MP}r_{MP}} \tag{2.13}$$

$$M = k_{\theta-MP}\Delta\theta[1 + 3k_{sextic}(\Delta\theta)^4] \tag{2.14}$$

where $\varepsilon_{MP} = (r_{MP} - ro)/r_{MP}$ is the tensile strain of beam element. Wernik and Meguid used beam elements for stretching of C-C bonds and rotational spring elements at the coinciding nodes of beam elements for bending (see Figure 2.23).

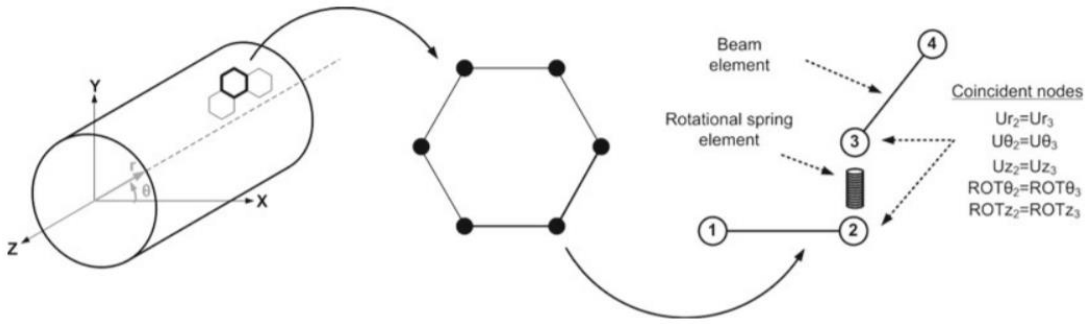

Figure 2.23: Beam and rotational spring elements used to represent C-C bonds [76].

Figures 2.24 and 2.25 are the plots of tensile stress versus strain for beam element and moment versus rotation for rotational spring element.

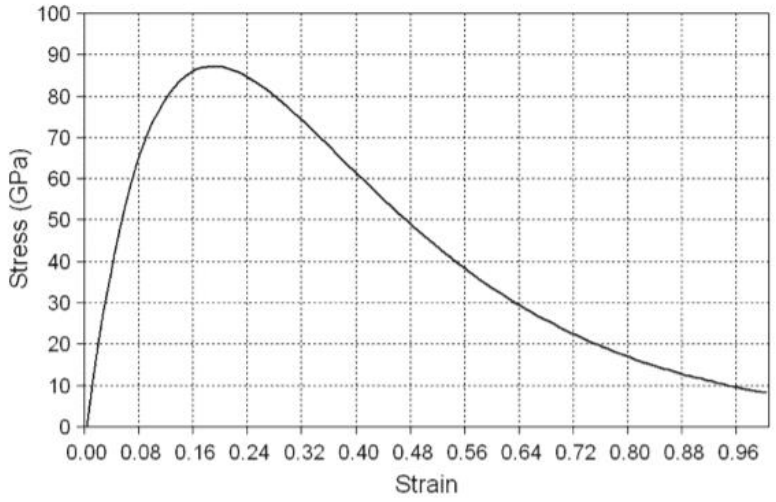

Figure 2.24: Tensile stress-strain relation derived from Morse potential [76].

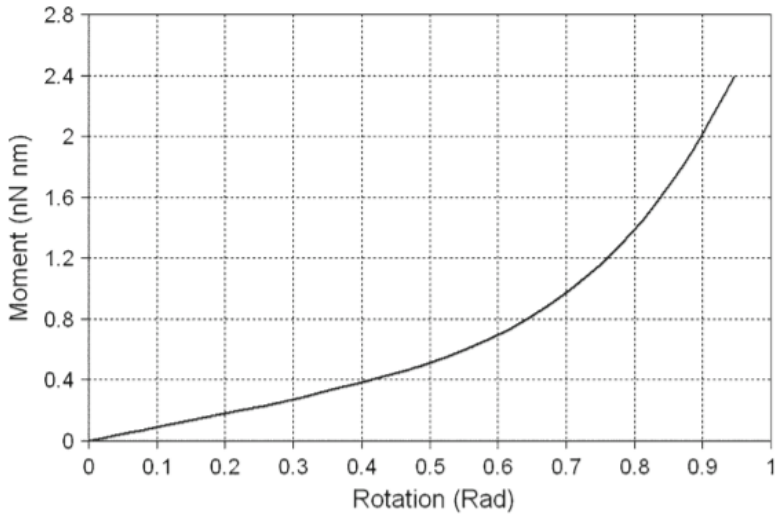

Figure 2.25: Moment-rotation relation derived from Morse potential [76].

2.6.2 Micro-Scale Model

Commercial finite element analysis (FEA) software is used for micro-scale analysis of CNTRP representative volume elements (RVEs) (see Figure 2.26). Polymer matrix is modelled by 3D solid elements because it has higher density than CNT thus regarded as continuum in micro-scale. Most of the researchers employed Li and Chou's method to model CNT and Lennard-Jones forces for modelling non-covalent interface [71], [78]–[81].

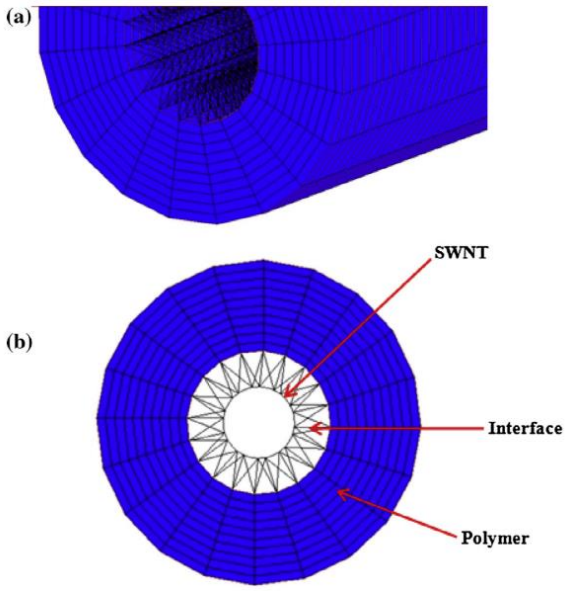

Figure 2.26: (a) Isometric view of micro-scale RVE, (b) Front view of micro-scale RVE showing constituting parts [78].

Zuberi and Esat also investigated the perfect bonding case and modelled CNT, interface and matrix as continuum (see Figure 2.27) [78].

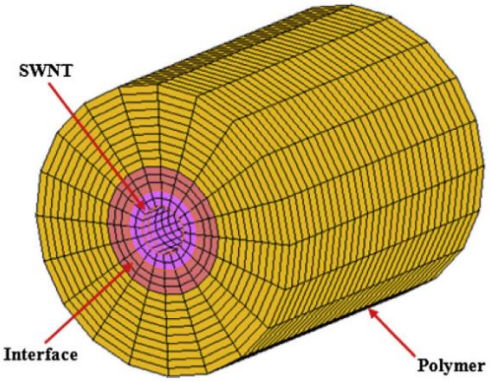

Figure 2.27: Micro-Scale CNTRP with perfect bonding [78].

Wernik and Meguid modelled the CNT by utilizing Morse interatomic potential. Apart from that, the interface and the polymer matrix are modelled in the same manner as the aforementioned models (see Figure 2.28) [76].

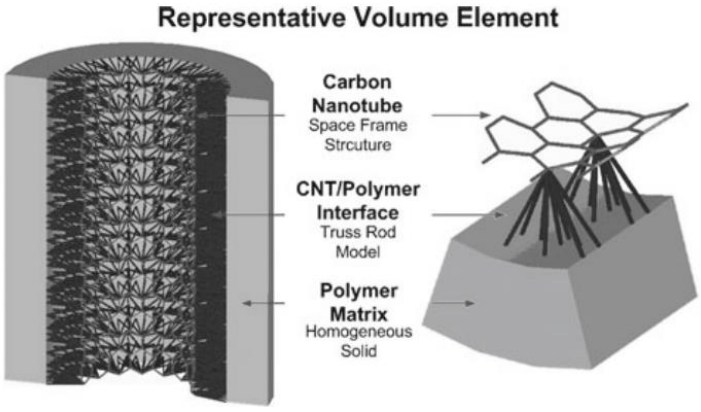

Figure 2.28: RVE developed by Wernik and Meguid [76].

Micro-scale RVE is a transversely isotropic material and elasticity stiffness matrix has 5 independent constants (see Figure 2.29). These constants can be calculated by applying 5 sets of boundary conditions (see Table 2.2) [82].

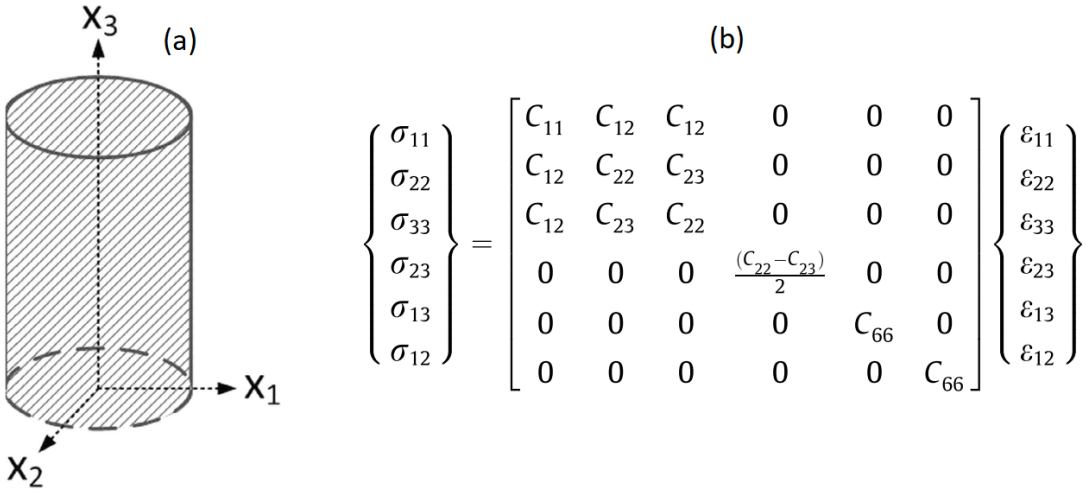

$$\begin{Bmatrix} \sigma_{11} \\ \sigma_{22} \\ \sigma_{33} \\ \sigma_{23} \\ \sigma_{13} \\ \sigma_{12} \end{Bmatrix} = \begin{bmatrix} C_{11} & C_{12} & C_{12} & 0 & 0 & 0 \\ C_{12} & C_{22} & C_{23} & 0 & 0 & 0 \\ C_{12} & C_{23} & C_{22} & 0 & 0 & 0 \\ 0 & 0 & 0 & \frac{(C_{22}-C_{23})}{2} & 0 & 0 \\ 0 & 0 & 0 & 0 & C_{66} & 0 \\ 0 & 0 & 0 & 0 & 0 & C_{66} \end{bmatrix} \begin{Bmatrix} \varepsilon_{11} \\ \varepsilon_{22} \\ \varepsilon_{33} \\ \varepsilon_{23} \\ \varepsilon_{13} \\ \varepsilon_{12} \end{Bmatrix}$$

Figure 2.29: (a) Schematic representation of RVE fibre, (b) Constitutive relation of transversely isotropic material [82].

Table 2.2*: Elastic constants and corresponding boundary conditions* [82].

Elastic Constant	Strain Energy Equation	Boundary Condition	Boundary Displacement
E	$U = \frac{1}{8}\pi D^2 L E_L e^2$	$\varepsilon_{11} = e$ $\sigma_{22} = \sigma_{33} = 0$	$u_1(B) = ex_1$ $T_2(B) = 0$ $T_3(B) = 0$
G_L	$U = \frac{1}{8}\pi D^2 L G_L e^2$	$\varepsilon_{12} = e/2$	$u_1(B) = \frac{e}{2}x_2$ $u_2(B) = \frac{e}{2}x_1$ $u_3(B) = 0$
G_T	$U = \frac{1}{8}\pi D^2 L G_T e^2$	$\varepsilon_{23} = e/2$	$u_1(B) = 0$ $u_2(B) = \frac{e}{2}x_3$ $u_3(B) = \frac{e}{2}x_2$
K_T	$U = \frac{1}{2}\pi D^2 L K_T e^2$	$\varepsilon_{22} = \varepsilon_{33} = e$	$u_1(B) = 0$ $u_2(B) = ex_2$ $u_3(B) = ex_3$
C_{11}	$U = \frac{1}{8}\pi D^2 L C_{11} e^2$	$\varepsilon_{11} = e$	$u_1(B) = ex_1$ $u_2(B) = 0$ $u_3(B) = 0$

The mechanical properties obtained from micro-scale RVE contain matrix as well. Shokrieh and Rafiee extracted the mechanical properties of CNT and interface by utilizing inverse rule of mixtures [79]. They named this phase as equivalent fibre (EF). Inverse rule of mixtures formulae are [79]:

$$E_{LEF} = \frac{E_{LC}}{V_{EF}} - \frac{E_M V_M}{V_{EF}} \tag{2.15}$$

$$\frac{1}{E_{TEF}} = \frac{1}{E_{TC} V_{EF}} - \frac{V_M}{E_M V_{EF}} \tag{2.16}$$

$$\frac{1}{G_{EF}} = \frac{1}{G_C V_{EF}} - \frac{V_M}{G_M V_{EF}} \tag{2.17}$$

$$v_{EF} = \frac{v_C}{V_{EF}} - \frac{v_M V_M}{V_{EF}} \tag{2.18}$$

where E_{LEF}, E_{TEF}, G_{EF}, v_{EF} and V_{EF} are longitudinal modulus, transverse modulus, shear modulus, Poisson's ratio and volume fraction of EF, respectively. E_M, G_M, v_M and V_M are Young's modulus, shear modulus, Poisson's ratio and volume fraction of matrix, respectively. E_{LC}, E_{TC}, G_C and v_C are longitudinal, transverse, shear moduli and Poisson's ratio of micro-scale RVE composite [79]. Figure 2.30 depicts the EF extracted from composite.

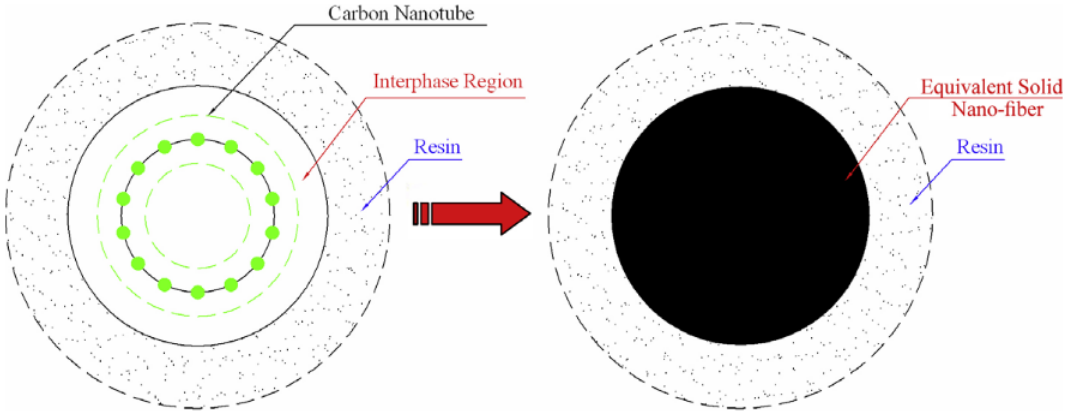

Figure 2.30: Depiction of converting CNT and interface into EF [79].

2.6.3 Meso-Scale Model

Shi et al. [83] exploited Mori-Tanaka method [84] to estimate elastic properties of CNTRP. They developed three cases which are aligned CNTs case, randomly distributed CNTs case and randomly distributed and agglomerated CNTs case. In this method, CNTs are considered as straight fibres [83].

2.6.3.1 Aligned CNTs Case

Mori-Tanaka method considers matrix as infinite pristine material which surrounds ellipsoidal inclusions. It is assumed that each inclusion is subjected to effective stress or strain in the far field. Stress-strain constitutive equation (Equation 2.19) and elasticity tensor of CNTRP which contains aligned CNTs with the same shape (Equation 2.20) are as follows [83]:

$$\sigma = C : \varepsilon \tag{2.19}$$

$$C = (c_m C_m + c_r C_r : A) : (c_m I + c_r A)^{-1} \tag{2.20}$$

where colon means inner product, I is identity tensor, subscripts m and r represent matrix and reinforcing phase, respectively, c_m and c_r are volume fractions, C_m and C_r stand for elasticity tensor and A is the relation between average strains ε_r and ε_m[83]. A is given in Equation 2.21 [83],

$$A = [I + S:(C_m)^{-1}:(C_r - C_m)]^{-1} \tag{2.21}$$

where S is Eshelby tensor [85], [86]. The matrix is assumed elastic-isotropic with Young's modulus E_m and Poisson's ration v_m and CNTs are aligned in x-2 direction. Equation 2.19 is expressed in terms of Hill's elastic moduli in Figure 2.31. Hill's elastic moduli [87] are k, l, m, n and p which stand for plane-strain bulk modulus normal to fibre direction, associated cross modulus, shear moduli in planes normal to fibre direction, uniaxial tension modulus and shear moduli in planes parallel to fibre direction, respectively [83].

$$\begin{Bmatrix} \sigma_{11} \\ \sigma_{22} \\ \sigma_{33} \\ \sigma_{23} \\ \sigma_{13} \\ \sigma_{12} \end{Bmatrix} = \begin{bmatrix} k+m & l & k-m & 0 & 0 & 0 \\ l & n & l & 0 & 0 & 0 \\ k-m & l & k+m & 0 & 0 & 0 \\ 0 & 0 & 0 & p & 0 & 0 \\ 0 & 0 & 0 & 0 & m & 0 \\ 0 & 0 & 0 & 0 & 0 & p \end{bmatrix} \begin{Bmatrix} \varepsilon_{11} \\ \varepsilon_{22} \\ \varepsilon_{33} \\ 2\varepsilon_{23} \\ 2\varepsilon_{13} \\ 2\varepsilon_{12} \end{Bmatrix}$$

Figure 2.31: Constitutive relation in terms of Hill's elastic moduli [83].

Non-vanishing components of Eshelby tensor for straight, aligned fibres are shown in Equation 2.22 [85], [86]. It is substituted into Equation 2.21 and non-vanish components of A are written in Equation 2.23. Substitution of A into Equation 2.20 gives elastic properties of CNTRP which can be written in terms of Hill's elastic moduli (see Equation 2.24). Young's modulus parallel and perpendicular to fibre orientation is calculated using Equation 2.25 [83].

$$S_{1111} = S_{3333} = \frac{5 - 4v_m}{8(1 - v_m)}, \quad S_{1122} = S_{3322} = \frac{v_m}{2(1 - v_m)},$$
$$S_{1133} = S_{3311} = \frac{4v_m - 1}{8(1 - v_m)}, \quad S_{2323} = S_{1212} = \frac{1}{4}$$
$$S_{1313} = \frac{3 - 4v_m}{8(1 - v_m)} \tag{2.22}$$

$$A_{1111} = A_{3333} =$$
$$-\frac{E_m(1-v_m)\{E_m + 2k_r(1+v_m)[m_r(3-4v_m) + k_r(2-4v_m)]\}}{(-1+2v_m)[E_m + 2k_r(1+v_m)][E_m + 2m_r(3-v_m-4v_m^2)]},$$

$$A_{1133} = A_{3311} =$$
$$-\frac{(E_m(1-v_m)\{E_m(1-4v_m) + 2(v_m+1)[m_r(3-4v_m) + k_r(2-4v_m)]\})}{(-1+2v_m)[E_m + 2k_r(1+v_m)][E_m + 2m_r(3-v_m-4v_m^2)]}$$

$$A_{1122} = A_{3322} = \frac{l_r(1-v_m-2v_m^2) - E_m v_m}{(-1+2v_m)[E_m + 2k_r(1+v_m)]}$$

$$A_{2222} = 1$$

$$A_{2323} = A_{1212} = \frac{E_m}{E_m + 2p_r(1+v_m)}$$

$$A_{1313} = \frac{2E_m(1-v_m)}{E_m + 2m_r(3-v_m-4v_m^2)} \tag{2.23}$$

$$k = \frac{E_m\{E_m c_m + 2k_r(1+v_m)[1+c_r(1-2v_m)]\}}{2(1+v_m)[E_m(1+c_r-2v_m) + 2c_m k_r(1-v_m-2v_m^2)]}$$

$$l = \frac{E_m\{c_m v_m[E_m + 2k_r(1+v_m)] + 2c_r l_r(1-v_m^2)\}}{(1+v_m)[2c_m k_r(1-v_m-2v_m^2) + E_m(1+c_r-2v_m)]}$$

$$n = \frac{E_m^2 c_m(1+c_r-c_m v_m) + 2c_m c_r(k_r n_r - l_r^2)(1+v_m)^2(1-2v_m)}{(1+v_m)\{2c_m k_r(1-v_m-2v_m^2) + E_m(1+c_r-2v_m)\}} +$$
$$\frac{E_m[2c_m^2 k_r(1-v_m) + c_r n_r(1-2v_m+c_r) - 4c_m l_r v_m]}{2c_m k_r(1-v_m-2v_m^2) + E_m(1+c_r-2v_m)}$$

$$p = \frac{E_m[E_m c_m + 2(1+c_r)p_r(1+v_m)]}{2(1+v_m)[E_m(1+c_r) + 2c_m p_r(1+v_m)]}$$

$$m = \frac{E_m[E_m c_m + 2m_r(1+v_m)(3+c_r-4v_m)]}{2(1+v_m)\{E_m[c_m + 4c_r(1-v_m)] + 2c_m m_r(3-v_m-4v_m^2)\}} \tag{2.24}$$

$$E_{\parallel} = n = \frac{l^2}{k}, \quad E_{\perp} = \frac{4m(kn - l^2)}{kn - l^2 + mn} \tag{2.25}$$

2.6.3.2 Randomly Distributed CNTs Case

Random distribution of CNTs is controlled by probability density function (see Equation 2.26) [83].

$$\int_0^{2\pi} \int_0^{\frac{\pi}{2}} p(\alpha, \beta) \sin\alpha \, d\alpha \, d\beta = 1 \tag{2.26}$$

where α and β are Euler angles (see Figure 2.32). $p(\alpha, \beta)$ is equal to $1/2\pi$ for completely random distribution [83].

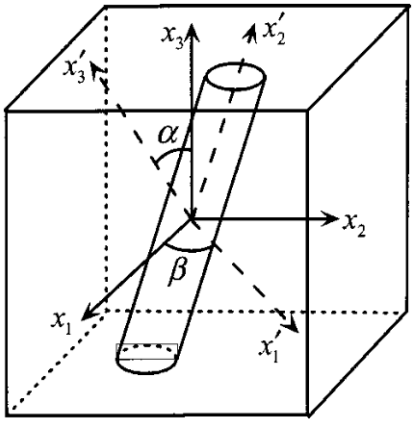

Figure 2.32: Rotation of a straight CNT with Euler angles α and β [83].

After taking average over special orientations, CNTRP elasticity tensor can be derived. CNTRP becomes isotropic material because of random distribution of CNTs. Bulk and shear moduli of CNTRP are derived as [83],

$$K = K_M + \frac{c_r(\delta_r - 3K_m\alpha_r)}{3(c_m + c_r\alpha_r)}$$

$$G = G_m + \frac{c_r(\eta_r - 2G_m\beta_r)}{2(c_m + c_r\beta_r)} \tag{2.27}$$

where [83],

$$\beta_r = \frac{1}{5}\left\{\frac{4G_m + 2k_r + l_r}{3(G_m + k_r)} + \frac{4G_m}{G_m + p_r} + \frac{2[G_m(3K_m + G_m) + G_m(3K_m + 7G_m)]}{G_m(3K_m + G_m) + m_r(3K_m + 7G_m)}\right\}$$

$$\delta_r = \frac{1}{3}\left[n_r + 2l_r + \frac{(2k_r + l_r)(3K_m + 2G_m - l_r)}{G_m + k_r}\right]$$

$$\eta_r = \frac{1}{5}\left[\frac{2}{3}(n_r - l_r) + \frac{8G_m p_r}{G_m + p_r} + \frac{8m_r G_m(K_m + 4G_m)}{3K_m(m_r + G_m) + G_m(7m_r + G_m)} + \frac{2(k_r - l_r)(2G_m + l_r)}{3(G_m + k_r)}\right] \quad (2.28)$$

Young's modulus and Poisson's ratio can be calculated by substituting K and G into Equation 2.29 [83].

$$E = \frac{9KG}{3K + G}$$

$$v = \frac{3K - 2G}{6K + 2G} \quad (2.29)$$

2.6.3.3 Randomly Distributed and Agglomerated CNTs Case

CNTs tend to agglomerate in matrix due to its inherent chemical and physical properties which are low bending stiffness, high aspect ratio and van der Waals forces between them [88]–[90]. Agglomerates have higher CNT concentrations than the rest of the matrix [91]. Agglomeration of CNTs diminish the mechanical properties CNTRP [88]. In order to reveal the effects of agglomeration Shi et al. developed a new model that considers agglomeration as well [83].

$$V_r = V_r^{inclusion} + V_r^m \quad (2.30)$$

CNT agglomerates are represented by spherical inclusions. V_r, $V_r^{inclusion}$ and V_r^m represents volume of reinforcement, volume of reinforcement inside inclusions and volume of reinforcements in hybrid matrix. ξ, ζ and c_r are defined in Equations 2.31 and 2.32 [83].

$$\xi = \frac{V_{inclusion}}{V} \quad (2.31)$$

$$\zeta = \frac{V_r^{inclusion}}{V_r}$$

$$c_r = \frac{V_r}{V} \tag{2.32}$$

CNT concentration in inclusions and hybrid matrix are defined in Equation 2.33 [83].

$$\frac{V_r^{inclusion}}{V_{inclusion}} = \frac{c_r \zeta}{\xi}$$

$$\frac{V_r^{m}}{V - V_{inclusion}} = \frac{c_r(1-\zeta)}{1-\xi} \tag{2.33}$$

Modifying Equation 2.27 in terms ξ, ζ and c_r gives Equation 2.34. Subscript in and out stand for inside and outside spherical inclusion, respectively [83].

$$K_{in} = K_m + \frac{(\delta_r - 3K_m\alpha_r)c_r\zeta}{3(\xi - c_r\zeta + c_r\zeta\alpha_r)}$$

$$K_{out} = K_m + \frac{c_r(\delta_r - 3K_m\alpha_r)(1-\zeta)}{3[1-\xi - c_r(1-\zeta) + c_r(1-\zeta)\alpha_r]}$$

$$G_{in} = G_m + \frac{c_r\zeta(\eta_r - 2G_m\beta_r)}{2(\xi - c_r\zeta + c_r\zeta\beta_r)}$$

$$G_{out} = G_{in} + \frac{c_r(1-\zeta)(\eta_r - 2G_m\beta_r)}{2[1-\xi - c_r(1-\zeta) + c_r(1-\zeta)\beta_r]} \tag{2.34}$$

Eshelby's tensor for spherical inclusions in isotropic matrix is given in Equation 2.35 [83].

$$S_{1111} = S_{2222} = S_{3333} = \frac{7 - 5v_{out}}{15(1 - v_{out})}$$
$$S_{1122} = S_{2233} = S_{3311} = -\frac{1 - 5v_{out}}{15(1 - v_{out})}$$
$$S_{1212} = S_{2323} = S_{3131} = \frac{4 - 5v_{out}}{15(1 - v_{out})} \quad (2.35)$$

Poisson's ratio of hybrid matrix is calculated by Equation 2.36 [83].

$$v_{out} = \frac{3K_{out} - 2G_{out}}{2(3K_{out} + G_{out})} \quad (2.36)$$

By substituting Equation 2.36 into Equation 2.21 and performing necessary substitutions, bulk and shear moduli of agglomerated CNTRP is derived (see Equation 2.37 and 2.38) [83].

$$K = K_{out}\left[1 + \frac{\xi\left(\frac{K_{in}}{K_{out}} - 1\right)}{1 + \alpha_{MT}(1 - \xi)(\frac{K_{in}}{K_{out}} - 1)}\right]$$

$$G = G_{out}\left[1 + \frac{\xi(\frac{G_{in}}{G_{out}} - 1)}{1 + \beta_{MT}(1 - \xi)(\frac{G_{in}}{G_{out}} - 1)}\right] \quad (2.37)$$

where α_{MT} and β_{MT} are,

$$\alpha_{MT} = \frac{1 + v_{out}}{3(1 - v_{out})}$$
$$\beta_{MT} = \frac{2(4 - 5v_{out})}{15(1 - v_{out})} \quad (2.38)$$

2.6.4 Macro-Scale Model

Shokrieh and Rafiee [69], Ghasemi et al. [70] and Vu-Bac et al. [71] developed stochastic multiscale model and investigated the effects of parameters at different length scales (nano, micro, meso and macro) on macroscopic mechanical properties of CNTRP. Some of the parameters considered were

CNT length, orientation, agglomeration, curvature and dispersion. They constructed a tessellate that is composed of meso-scale models with varying parameters and applied certain boundary conditions to this tessellate in a FEA software to calculate mechanical properties of this macroscopic CNTRP (see Figure 2.33) [69].

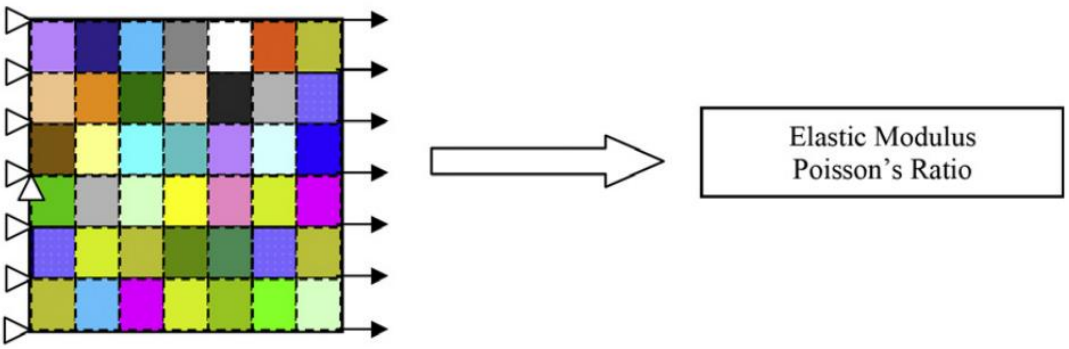

Figure 2.33: FEA of tessellated CNTRP [69].

2.7 Analytical Micromechanics

Several micromechanics methods are developed to estimate the mechanical properties of composite materials. In this section some of these methods are explained.

2.7.1 Rule of Mixtures

Rule of mixtures covers only aligned fibre composites. Elastic modulus in fibre direction is calculated by [92],

$$E_L = c_r E_f + (1 - c_r) E_m \tag{2.39}$$

E_L, E_f and E_m are Young's modulus of composite in fibre direction, Young's modulus of fibre and Young's modulus of matrix, respectively. c_r is the volume fraction of fibre which is equal to fibre volume over the whole volume of composite. Elastic modulus perpendicular to the fibre orientation is calculated by Equation 2.40 [93].

$$E_T = \left(\frac{c_r}{E_f} + \frac{1 - c_r}{E_m} \right)^{-1} \tag{2.40}$$

2.7.2 Hashin-Shtrikman Bounds

Hashin and Shtrikman developed this model to predict maximum and minimum elastic properties of composites (see Equation 2.41) [94].

$$K_c^u = K_f + (1 - v_f)\left[\frac{1}{K_m - K_f} + \frac{3v_f}{3K_f + 4G_f}\right]^{-1}$$

$$K_c^l = K_m + v_f\left[\frac{1}{K_f - K_m} + \frac{3(1 - v_f)}{3K_m + 4G_m}\right]^{-1}$$

$$G_c^u = G_f + (1 - v_f)\left[\frac{1}{G_m - G_f} + \frac{6v_f(K_f + 2G_f)}{5G_f(3K_f + 4G_f)}\right]^{-1}$$

$$G_c^l = G_m + v_f\left[\frac{1}{G_f - G_m} + \frac{6(1 - v_f)(K_m + 2G_m)}{5G_m(3K_m + 4G_m)}\right]^{-1} \quad (2.41)$$

where subscripts f, m and c stands for fibre, matrix and composite, respectively. Superscripts u mean upper bound while l mean lower bound. K, G and v represents bulk and shear moduli and Poisson's ratio, respectively [94].

2.7.3 Halpin-Tsai Equations

This method is used for estimating the mechanical properties of discontinuous fibre reinforced composites [5].

$$E_{11} = \frac{1 + 2\left(\frac{l_f}{d_f}\right)\eta_L v_f}{1 - \eta_L v_f} E_m \quad (2.42)$$

$$E_{22} = \frac{1 + 2\eta_T v_f}{1 - \eta_T v_f} E_m \quad (2.43)$$

E_{11}, E_{22} and G_{12} are longitudinal, transverse and shear moduli of composite, respectively. l_f is fibre length and d_f is diameter of fibre.

$$G_{12} = G_{21} = \frac{1 + \eta_G v_f}{1 - \eta_G v_f} G_m \tag{2.44}$$

$$v_{12} = v_f c_r + v_m c_m$$

$$v_{21} = \frac{E_{22}}{E_{11}} v_{12} \tag{2.45}$$

where c_r and c_m are volume fractions of fibre and matrix, respectively and v denotes Poisson's ratio.

$$\eta_L = \frac{\frac{E_f}{E_m} - 1}{\left(\frac{E_f}{E_m}\right) + 2(\frac{l_f}{d_f})} \tag{2.46}$$

$$\eta_T = \frac{\frac{E_f}{E_m} - 1}{\left(\frac{E_f}{E_m}\right) + 2} \tag{2.47}$$

$$\eta_G = \frac{\left(\frac{G_f}{G_m}\right) - 1}{\left(\frac{G_f}{G_m}\right) + 1} \tag{2.48}$$

$$E_{random} = \frac{3}{8} E_{11} + \frac{5}{8} E_{22}$$

$$G_{random} = \frac{1}{8} E_{11} + \frac{1}{4} E_{22}$$

$$v_{random} = \frac{E_{random}}{2G_{random}} - 1 \tag{2.49}$$

Subscript $random$ stands for randomly distributed fibre composite.

2.7.4 Cox's Model

Cox's model can be used for composites with fibres aligned in one direction, aligned in-plane and aligned completely random [95], [96].

$$E_c = (\eta_0 \eta_l E_f - E_m) c_r + E_m \tag{2.50}$$

where,

$$\eta_l = 1 - \frac{\tanh(al/d)}{al/d} \tag{2.51}$$

where,

$$a = \sqrt{\frac{-3E_m}{2E_f \ln(c_r)}} \tag{2.52}$$

η_0 is the orientation efficiency factor and it is equal to 1, 3/8 or 1/5 for aligned, aligned in-plane and randomly oriented fibres, respectively [97].

2.7.5 Mori-Tanaka Method and Self-Consistent Scheme

The model conceived by Shi et al. [83] was explained in Section 2.6.3.2. Pan and Bian [98] developed a similar model by combining Mori-Tanaka method with self-consistent scheme. This method is able take into account both isotropic and transversely isotropic CNT properties. For isotropic CNT reinforced composites the bulk and shear moduli for inside and outside the inclusions are given in Equations 2.53 and 2.54, respectively [98].

$$K_{out} = \frac{[1 - \xi - c_r(1-\zeta)]K_m + c_r(1-\zeta)\xi^{LA}}{[1 - \xi - c_r(1-\zeta)] + 3c_r(1-\zeta)\xi^{A}}$$

$$G_{out} = \frac{[1 - \xi - c_r(1-\zeta)]G_m + c_r(1-\zeta)\eta^{LA}}{[1 - \xi - c_r(1-\zeta)] + 2c_r(1-\zeta)\eta^{A}} \tag{2.53}$$

$$K_{in} = \frac{\xi K_m + \zeta c_r \xi^{LA}}{\xi + 3\zeta c_r \xi^A}$$

$$G_{in} = \frac{\xi G_m + \zeta c_r \eta^{LA}}{\xi + 2\zeta c_r \eta^A} \tag{2.54}$$

where ξ^A, η^A, $\xi^{LA}$and η^{LA} are given below [99],

$$\xi^A = \frac{1}{9\left(1 + \frac{\left(K_{CNT} + \frac{G_{CNT}}{3}\right) - \left(K_m + \frac{G_m}{3}\right)}{\left(K_m + \frac{G_m}{3}\right) + G_m}\right)}$$

$$* \left[2 - 2\left(\frac{\left(\left(K_{CNT} - \frac{2G_{CNT}}{3}\right) - \left(K_m - \frac{2G_m}{3}\right)\right)}{2\left(K_m + \frac{G_m}{3} + G_m\right)}\right) + 1 + \frac{\left(K_{CNT} + \frac{G_{CNT}}{3}\right) - \left(K_m + \frac{G_m}{3}\right)}{\left(K_m + \frac{G_m}{3}\right) + G_m}\right] \tag{2.55}$$

$$\eta^A = \left[1 + 2\left(\frac{\left(\left(K_{CNT} - \frac{2G_{CNT}}{3}\right) - \left(K_m - \frac{2G_m}{3}\right)\right)}{2\left(K_m + \frac{G_m}{3} + G_m\right)}\right) + 2\left(1 + \frac{\left(K_{CNT} + \frac{G_{CNT}}{3}\right) - \left(K_m + \frac{G_m}{3}\right)}{\left(K_m + \frac{G_m}{3}\right) + G_m}\right)\right] / \left[30\left(1 + \frac{\left(K_{CNT} + \frac{G_{CNT}}{3}\right) - \left(K_m + \frac{G_m}{3}\right)}{\left(K_m + \frac{G_m}{3}\right) + G_m}\right)\right]$$

$$+ \frac{\left(1 + \left[\left(K_m + \frac{G_m}{3} + 2G_m\right)(G_{CNT} - G_m)\right] / \left[2G_m(G_m + K_m + \frac{G_m}{3})\right]\right)^{-1}}{5}$$

$$+ \frac{(1 + (G_{CNT} - G_m)/2G_m)^{-1}}{5} \qquad (2.56)$$

$$\xi^{LA} = \Bigg\{ \left[4\left(K_{CNT} + \frac{G_{CNT}}{3} \right) \right]$$

$$+ 2 \Bigg[\left(K_{CNT} - \frac{2G_{CNT}}{3} \right)$$

$$+ \left(\left(K_{CNT} - \frac{2G_{CNT}}{3} \right) \left(1 + \frac{\left(K_{CNT} + \frac{G_{CNT}}{3} \right) - \left(K_m + \frac{G_m}{3} \right)}{\left(K_m + \frac{G_m}{3} \right) + G_m} \right) \right)$$

$$- 2 \left(\left(K_{CNT} + \frac{G_{CNT}}{3} \right) \left(\frac{\left(\left(K_{CNT} - \frac{2G_{CNT}}{3} \right) - \left(K_m - \frac{2G_m}{3} \right) \right)}{2\left(K_m + \frac{G_m}{3} + G_m \right)} \right) \right) \Bigg]$$

$$+ \Bigg[\left(K_{CNT} + \frac{4G_{CNT}}{3} \right) \left(1 + \frac{\left(K_{CNT} + \frac{G_{CNT}}{3} \right) - \left(K_m + \frac{G_m}{3} \right)}{\left(K_m + \frac{G_m}{3} \right) + G_m} \right)$$

$$- 2\left(K_{CNT} - \frac{2G_{CNT}}{3} \right) \left(\frac{\left(\left(K_{CNT} - \frac{2G_{CNT}}{3} \right) - \left(K_m - \frac{2G_m}{3} \right) \right)}{2\left(K_m + \frac{G_m}{3} + G_m \right)} \right) \Bigg] \Bigg\}$$

$$/ \left\{ 9 \left(1 + \frac{\left(K_{CNT} + \frac{G_{CNT}}{3} \right) - \left(K_m + \frac{G_m}{3} \right)}{\left(K_m + \frac{G_m}{3} \right) + G_m} \right) \right\} \qquad (2.57)$$

$$\eta^{LA} = \left\{\left[\left(K_{CNT} + \frac{G_{CNT}}{3}\right)\right.\right.$$

$$- \left(\left(K_{CNT} - \frac{2G_{CNT}}{3}\right)\right.$$

$$+ \left(K_{CNT} - \frac{2G_{CNT}}{3}\right)\left(1 + \frac{\left(K_{CNT} + \frac{G_{CNT}}{3}\right) - \left(K_m + \frac{G_m}{3}\right)}{\left(K_m + \frac{G_m}{3}\right) + G_m}\right)$$

$$- 2\left(\left(K_{CNT} + \frac{G_{CNT}}{3}\right)\left(\frac{\left(\left(K_{CNT} - \frac{2G_{CNT}}{3}\right) - \left(K_m - \frac{2G_m}{3}\right)\right)}{2\left(K_m + \frac{G_m}{3} + G_m\right)}\right)\right)\Bigg)$$

$$+ \left(\left(K_m + \frac{4G_m}{3}\right)\left(1 + \frac{\left(K_{CNT} + \frac{G_{CNT}}{3}\right) - \left(K_m + \frac{G_m}{3}\right)}{\left(K_m + \frac{G_m}{3}\right) + G_m}\right)\right.$$

$$\left.\left.- 2\left(\left(K_m - \frac{2G_m}{3}\right)\left(\frac{\left(\left(K_{CNT} - \frac{2G_{CNT}}{3}\right) - \left(K_m - \frac{2G_m}{3}\right)\right)}{2\left(K_m + \frac{G_m}{3} + G_m\right)}\right)\right)\right)\right]$$

$$\left.\left./\left[15\left(1 + \frac{\left(K_{CNT} + \frac{G_{CNT}}{3}\right) - \left(K_m + \frac{G_m}{3}\right)}{\left(K_m + \frac{G_m}{3}\right) + G_m}\right)\right]\right\}$$

$$+ \left\{\left[2\left(\left(\left(G_{CNT}\right.\right.\right.\right.\right.$$

$$\left./\left(1 + \left(\left(K_m + \frac{G_m}{3} + 2G_m\right)(G_{CNT} - G_m)\right)/\left(2G_m\left(G_m + K_m + \frac{G_m}{3}\right)\right)\right)\right.$$

$$\left.\left.\left.\left.\left. + G_{CNT}/(1 + (G_{CNT} - G_m)/2G_m)\right)\right)\right]/5\right\} \tag{2.58}$$

Bulk and shear moduli inside and outside the spherical inclusions for transversely isotropic CNTs case is the same as Shi et al [83] (see Equation 2.34).

Substituting Equations 2.59 and 2.60 into Equation 2.61 give the bulk and shear moduli of CNTRP [98].

$$\begin{aligned} \overline{K} &= c_r K_{in} + c_m K_{out} \\ \bar{G} &= c_r G_{in} + c_m G_{out} \end{aligned} \tag{2.59}$$

$$\alpha = \frac{3\overline{K}}{3\overline{K} + 4\bar{G}}$$

$$\beta = \frac{6(\overline{K} + 2\bar{G})}{5(3\overline{K} + 4\bar{G})} \tag{2.60}$$

$$\frac{1}{K} = \frac{\xi}{\xi K_{in} + (1-\xi)\dfrac{\overline{K}(1-\alpha) + \alpha K_{in}}{\dfrac{\overline{K}(1-\alpha)}{K_{out}} + \alpha}} + \frac{1-\xi}{(1-\xi)K_{out} + \xi\dfrac{\overline{K}(1-\alpha) + \alpha K_{out}}{\dfrac{\overline{K}(1-\alpha)}{K_{in}} + \alpha}}$$

$$\frac{1}{G} = \frac{\xi}{\xi G_{in} + (1-\xi)\dfrac{\bar{G}(1-\beta) + \beta G_{in}}{\dfrac{\bar{G}(1-\beta)}{G_{out}} + \beta}} + \frac{1-\xi}{(1-\xi)G_m + \xi\dfrac{\bar{G}(1-\beta) + \beta G_{out}}{\dfrac{\bar{G}(1-\beta)}{G_{in}} + \beta}} \tag{2.61}$$

2.7.6 Hui-Shia Model

It is a Mori-Tanaka [84] based model. This model is able to calculate elastic properties of only aligned fibre reinforced composites [100], [101].

$$E_L = E_m\left(1 - \frac{c_r}{\lambda}\right)^{-1} \tag{2.62}$$

$$E_T = E_m\left(1 - \frac{c_r}{4}\left(\frac{1}{\lambda} + \frac{3}{\lambda + \mu}\right)\right) \tag{2.63}$$

where λ, μ and κ are given below and Λ is aspect ratio of fibre.

$$\lambda = c_r + \frac{E_m}{E_f - E_m} + 3(c_m)\left[\frac{(1-\kappa)\Lambda^2 - \frac{\kappa}{2}}{\Lambda^2 - 1}\right] \tag{2.64}$$

$$\mu = f_m\left(\frac{3(\Lambda^2 + 0.25)\kappa - 2\Lambda^2}{\Lambda^2 - 1}\right) \tag{2.65}$$

$$\kappa = \frac{\Lambda}{(\Lambda^2 - 1)^{\frac{3}{2}}}\left[\Lambda\sqrt{\Lambda^2 - 1} - \cosh^{-1}\Lambda\right] \tag{2.66}$$

2.7.7 Wang-Pyrz Model

This method is also based on Mori-Tanaka approach and considers aspect ratio. It is used for randomly distributed CNTs case [101], [102]. Bulk and shear moduli are given in Equation 2.67.

$$K = K_m + K_m\frac{c_r\varphi}{1 - c_r(1-\Omega)}$$

$$G = G_m + G_m\frac{c_r\Psi}{1 - c_r(1-\gamma)} \tag{2.67}$$

where φ, Ψ, Ω and γ are as follows,

$$\varphi = \frac{1}{3F_2}(2F_6A_1 + 6F_6B_1 + F_7A_2 + 3F_7B_2)$$

$$\Psi = \frac{1}{5F_2}(F_8A_1 + F_9A_2 + 2F_6B_1 + F_7B_2) + \frac{2}{5}\left(\frac{A_3}{F_4} + \frac{A_4}{F_3}\right) - \frac{\varphi}{5}$$

$$\Omega = \frac{F_1}{F_2}$$

$$\gamma = \frac{1}{5}\left(\frac{2}{F_3} + \frac{2}{F_4} + \frac{F_5 - F_1}{F_2}\right) \tag{2.68}$$

where F_1, F_2, F_3, F_4, F_5, F_6, F_7, F_8 and F_9 are:

$$F_1 = 1 + \frac{1}{3}\left[\frac{1}{2}(1-R)(3\Pi + 9\Sigma - 4) + 2R(1-\Sigma)\right]A_1 + \frac{1}{3}[(1-R)(2+3\Pi) + R(2-\Sigma)]A_2 + \frac{1}{3}(3-4R)(3\Sigma - 2)(B_1 - B_2) \quad (2.69)$$

$$F_2 = 1 + \frac{1}{2}(1-R)(\Pi + 3\Sigma)A_1 + [(1-R)(1+\Pi) + R(1-\Sigma)]A_2 + (3-4R)[\Sigma B_1 + (1-\Sigma)B_2] + \frac{1}{2}(3-4R)[\Pi + \Sigma - R(\Pi - \Sigma + 2\Sigma^2)](A_1A_2 + A_1B_2 + 2B_1A_2) \quad (2.70)$$

$$F_3 = 1 + \left[1 - \left(f + \frac{3}{2}\Sigma\right) + R(\Pi + \Sigma)\right]A_4 \quad (2.71)$$

$$F_4 = 1 + 0.25[\Pi + 3\Sigma + R(\Sigma - \Pi)]A_3 \quad (2.72)$$

$$F_5 = 2 + \frac{1}{2}(1-R)(\Pi + 3\Sigma)A_1 + [(1-R)(1+\Pi) + R(1-\Sigma)]A_2 + (3-4R)[\Sigma B_1 + (1-\Sigma)B_2] \quad (2.73)$$

$$F_6 = 1 + \frac{1}{2}[(1-R)(2+3\Pi) + R(2-\Sigma)]A_2 + \frac{1}{2}(3-4R)(2-3\Sigma)B_2 \quad (2.74)$$

$$F_7 = 1 + \frac{1}{2}[(1-R)(3\Pi + 9\Sigma - 4) + 4R(1-\Sigma)]A_1 + (3-4R)(3\Sigma - 2)B_1 \quad (2.75)$$

$$F_8 = 1 + [(1-R)(1+\Pi) + R(1-\Sigma)]A_2 + (3-4R)(1-\Sigma)B_2 \quad (2.76)$$

$$F_9 = 1 + \frac{1}{2}(1-R)(\Pi + 3\Sigma)A_1 + \Sigma(3-4R)B_1 \quad (2.77)$$

Non-dimensional constants are given below [101].

$$R = \frac{3G_m}{3K_m + 4G_m} \tag{2.78}$$

$$A_1 = \frac{k_f - l_f}{G_m} - 1$$

$$A_2 = \frac{n_f - l_f}{2G_m}$$

$$A_3 = \frac{m_f}{G_m} - 1$$

$$A_4 = \frac{p_f}{G_m} - 1 \tag{2.79}$$

$$B_1 = \frac{2k_f + l_f}{9K_m} - \frac{2k_f - 2l_f}{6G_m}$$

$$B_2 = \frac{n_f + 2l_f}{9K_m} - \frac{n_f - l_f}{6G_m} \tag{2.80}$$

If CNTs are considered as isotropic material then k, l, m, n and p becomes [101],

$$k = K + \frac{1}{3}G$$

$$n = K + \frac{4}{3}G$$

$$m = p = G$$

$$l = K - \frac{2}{3}G \tag{2.81}$$

Π and Σ are related to the geometry of inclusions and given in Equation 2.82.

$$\Pi = \frac{\Lambda^2}{\Lambda^2 - 1}(2 - 3\Sigma)$$

$$\Sigma = \frac{\Lambda}{(\Lambda^2 - 1)^{\frac{3}{2}}}\left[\Lambda(\Lambda^2 - 1)^{\frac{1}{2}} - \cosh^{-1}\Lambda\right] \tag{2.82}$$

2.8 Gaps in the Literature

Some of the gaps in the current literature are listed below.

- All of the researchers who worked on meso and macro-scale considered only weak bonded CNT-polymer interaction in their research. Functionalized CNTRP should also be modelled.
- To the best of author's knowledge MWNT reinforced polymer composite has not been modelled in meso or macro-scale before.
- There is a paucity of research on the plastic modelling of CNTRPs.
- Agglomeration is not taken into account in meso-scale FEAs.
- CNTs are not always blunt-open ended. The influence of capped CNTs on CNTRP should be investigated in meso-scale FEAs.
- Cohesive interface parameters are scarce in the literature. MD simulations can be done to obtain parameters for different CNT chiralities. Both CNT-CNT (for MWNT case) and CNT polymer interface parameters are required. These parameters will be very beneficial in meso-scale FEAs.
- Most of the researchers have dealt with intact CNTRPs but in reality CNTs can have defects, hence models of defected CNTRP are needed.

CHAPTER 3

THEORY AND METHODOLOGY

3.1 Generation of CNTs

At meso-scale FEA, CNTs are randomly scattered in matrix. Generally, CNTs are randomly scattered using either Monte-Carlo [103], [104] or Random Sequential Adsorption (RSA) [105], [106] algorithms. The codes which were developed to scatter CNTs are not publicly available, hence we have built our own code. C++ programming language is preferred for coding and the details of the code are explained in this chapter. The flowchart of CNT generation algorithm is shown in Appendix A.

3.1.1 Generating Straight CNTs

3.1.1.1 Orientation and Distribution of CNTs

The centre points of CNTs are chosen randomly inside the cubical RVE by exploiting uniform real distribution function of C++. The interval of uniform distribution is between the boundaries of RVE in x, y and z directions. This method is also applied by Chen et al. [107]. Preferably CNTs can be aligned in one direction (1D) (see Figure 3.1) or aligned completely random in 3D space (see Figure 3.2). Although CNTs are generally randomly distributed in matrix some studies show that CNTs can be aligned in one direction by magnetic-assisted methods [108], [109].

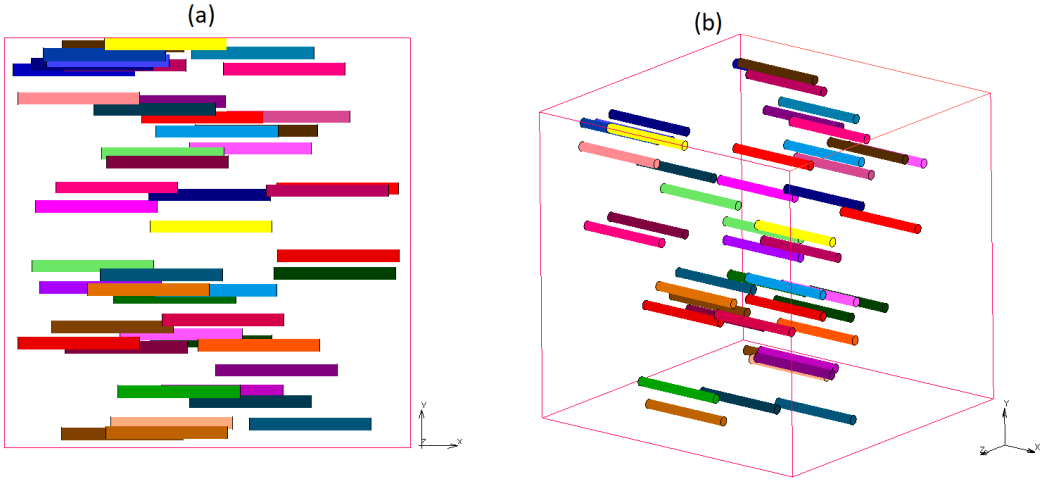

Figure 3.1: (a) Front and (b) isometric views of 1D aligned CNTs in RVE.

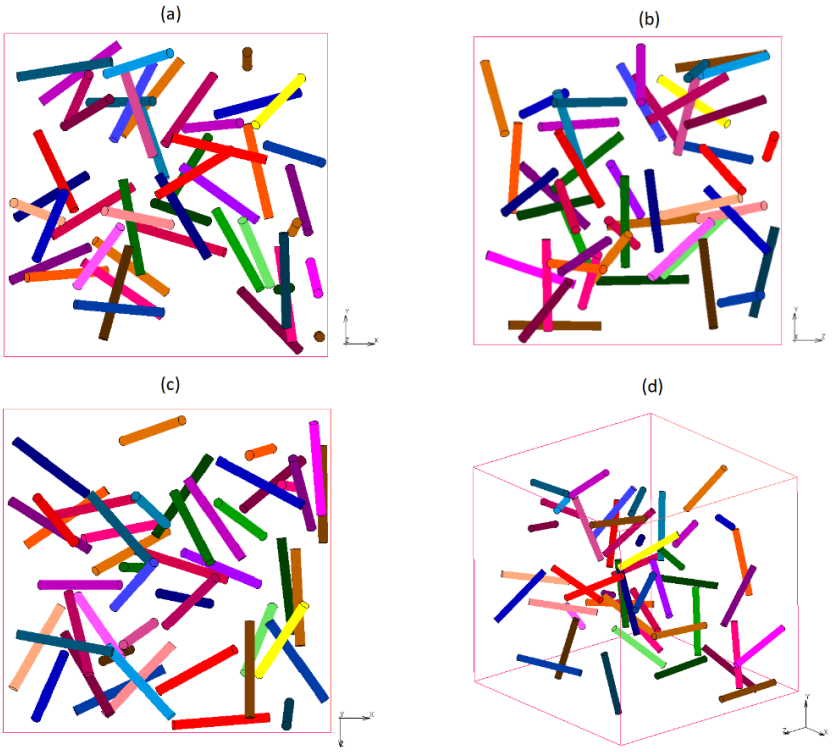

Figure 3.2: (a) Front, (b) left, (c) top and (d) isometric views of 3D aligned CNTs in RVE.

1D representation of CNT simply allows alignment along x-direction. On the other hand, in 3D random distribution CNTs are oriented with randomly selected spherical angles which are θ_r (inclination angle) and φ_r (azimuth angle) (see Figure 3.3). The relation between spherical coordinates and cartesian coordinates are given in Equation 3.1.

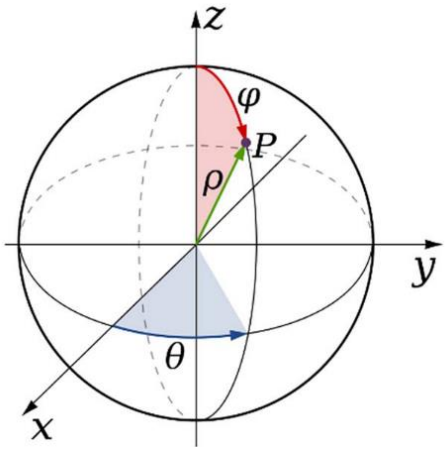

Figure 3.3: Spherical angles [103].

$$x = \rho \sin \varphi_r \cos \theta_r$$

$$y = \rho \sin \varphi_r \sin \theta_r$$

$$z = \rho \cos \varphi_r \tag{3.1}$$

ρ in Figure 3.3 and Equation 3.1 is the magnitude of the vector. Selection of $\theta_r \in [0, 2\pi)$ and $\varphi_r \in [0, \pi]$ by utilizing uniform distribution is wrong because with this method randomly selected points on sphere surface accumulate on the poles of the sphere (see Figure 3.4) [110].

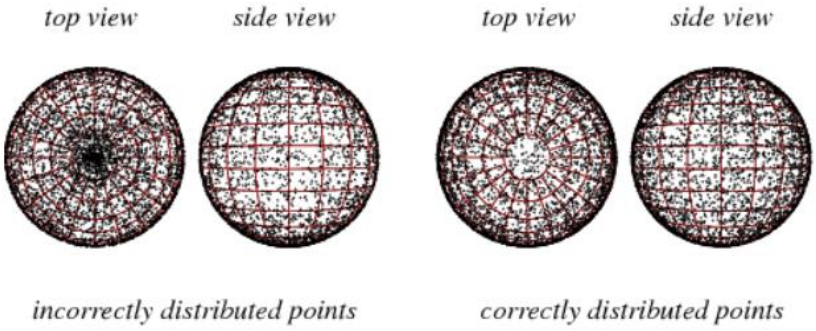

Figure 3.4: Comparison of sphere point picking with different methods [110].

Marsaglia [111] derived formulae (see Equation 3.2) to uniformly distribute randomly selected points on sphere.

$$x = 2x_1\sqrt{1 - x_1^2 - x_2^2}$$

$$y = 2x_2\sqrt{1 - x_1^2 - x_2^2}$$

$$z = 1 - 2(x_1^2 + x_2^2) \tag{3.2}$$

where $x_1 \in (-1,1)$ and $x_2 \in (-1,1)$ are selected randomly with uniform distribution and only x_1 and x_2 that satisfy the condition $x_1^2 + x_2^2 < 1$ are accepted [110]. Relation between cartesian coordinates and spherical coordinates (see Equation 3.1) is used to calculate spherical angles of CNTs.

3.1.1.2 Detection of CNT Collision

As it can be seen from Figures 3.1 and 3.2, CNTs are not allowed to collide. The minimum distance between CNTs is calculated and if it is less than the desired value the last created CNT is eliminated and a new one is created in place of it. Increasing the minimum distance between CNTs may predispose proper mesh generation.

If the cross product of two CNTs' axis lines is equal to 0 ($l_1 \; x \; l_2 = 0$) then CNTs are parallel and the distance between parallel lines is calculated by [112],

$$d_{\|} = \frac{\|l_1 \; x \; (m_1 - m_2/2)\|}{\|l_2\|^2}$$

$$m_{1,2} = po_{1,2} \; x \; l_{1,2} \tag{3.3}$$

where $l_2 = sl_1$ for $s \neq 0$ and po is a point on the line. The distance between CNTs should not be less than diameter of CNT. When the distance between parallel lines is lower than CNT diameter the perpendicular distance between CNTs should be calculated and it is not allowed more than CNT length (see Figure 3.5).

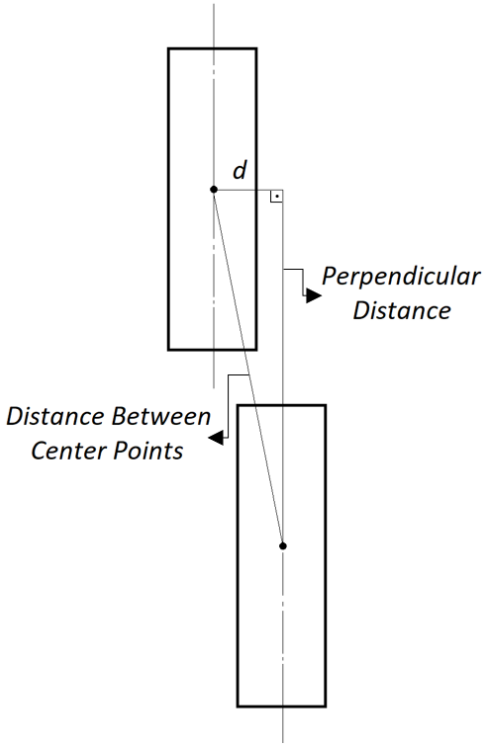

Figure 3.5: Illustration of parallel CNTs.

Unparallel CNTs case is divided into two which are lines intersecting each other and lines never intersecting each other (not coplanar). Equation 3.4 is used for testing intersectability, if reciprocal product is equal to 0 then the lines intersect each other [112].

$$Reciprocal\ Product = (l_1, m_1) * (l_2, m_2) = l_1.m_2 + l_2.m_1 \tag{3.4}$$

where the dot (.) represents dot product. The intersecting CNTs' axis lines has two scenarios. In the first scenario upper CNT is closer to intersection point while in the second scenario lower CNT is closer to intersection point (see Figure 3.6).

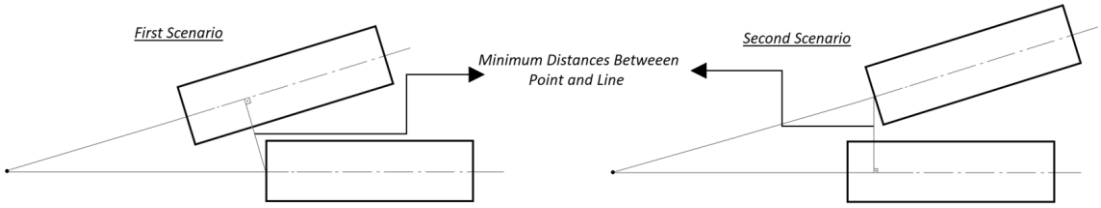

Figure 3.6: Minimum distances for intersecting CNT axes.

Intersection point of lines is found by the following equation [113],

$$x_{int} = x_p + \lambda a_1$$

$$y_{int} = y_p + \lambda b_1$$

$$z_{int} = z_p + \lambda c_1 \tag{3.5}$$

where subscript p means any point on the line and λ is given in Equation 3.6.

$$\lambda = \frac{a_2(y_2 - y_1) - b_1(x_2 - x_1)}{a_2 b_1 - a_1 b_2} \tag{3.6}$$

a, b and c are x, y and z components of direction vector, respectively. y and x are any points on the lines. Substituting Equation 3.6 into Equation 3.5 will give the coordinates of the intersection point. For conciseness, proof is not included but it can be found in reference [113].

Minimum distance is the length of the vector which is perpendicular to the axis line and reaches to the extremity point of CNT. This distance should not be allowed more than CNT diameter. It can be calculated by the following steps:

1. Write axis line equation in parametric form and solve for x, y, z components.
2. Subtract x, y, z from the point coordinates to find vector $\overrightarrow{PP'}$ (see Figure 3.7).
3. Calculate parametric equation constant by solving $\overrightarrow{PP'} . l = 0$.
4. Substitute parametric constant into $\overrightarrow{PP'}$ and calculate the length of this vector which is the minimum distance between point and line.

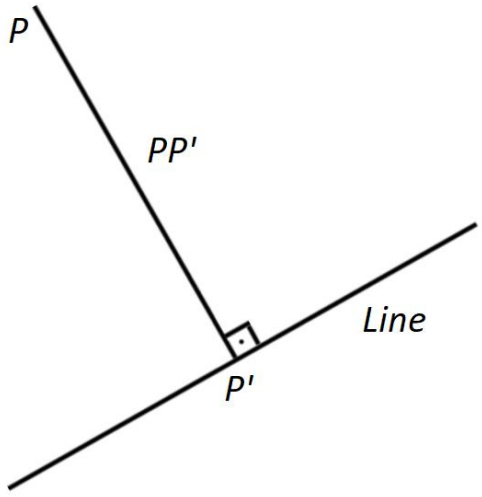

Figure 3.7: Depiction of minimum distance between a point and line.

Collision of noncoplanar CNTs is tested by the method developed by Ketchel and Larochelle [114]. This method is particularly developed for preventing collision of cylindrical robotic arms but it is also suitable for testing CNT collision. The minimum distance between noncoplanar lines is calculated by [112],

$$d = \frac{|(l_1, m_1) * (l_2, m_2)|}{\|l_1 x l_2\|} = \frac{l_1 . m_2 + l_2 . m_1}{\|l_1 x l_2\|} \tag{3.7}$$

In the first place, minimum distance between noncoplanar lines is calculated and if it is smaller than CNT diameter second test is applied. Secondly common normal line's intersection points with CNTs' axes are calculated. If both of the intersection points are inside CNT segments last generated CNT is removed but if only one of the intersection point is inside the CNT or neither of the points are inside the

CNT segment then the minimum distance between CNT's tip points and the other CNT's line is calculated and vice versa and if any of the calculations are below CNT diameter last generated CNT is removed [114]. Equation 3.8 is used for finding intersection points' locations.

$$t_1 = \frac{\left[\left(\vec{d} - \vec{c}\right) x\, \vec{w}\right].\vec{n}}{\vec{n}.\vec{n}}$$

$$t_2 = \frac{\left[\left(\vec{d} - \vec{c}\right) x\, \vec{s}\right].\vec{n}}{\vec{n}.\vec{n}}$$

$$\vec{n} = \vec{s}\, x\, \vec{w} \tag{3.8}$$

See Figure 3.8 for the location of vectors. If t_1 or t_2 gets a value between 0 and 1 it means that intersection points lie inside CNT, otherwise intersection points are out of CNTs [114].

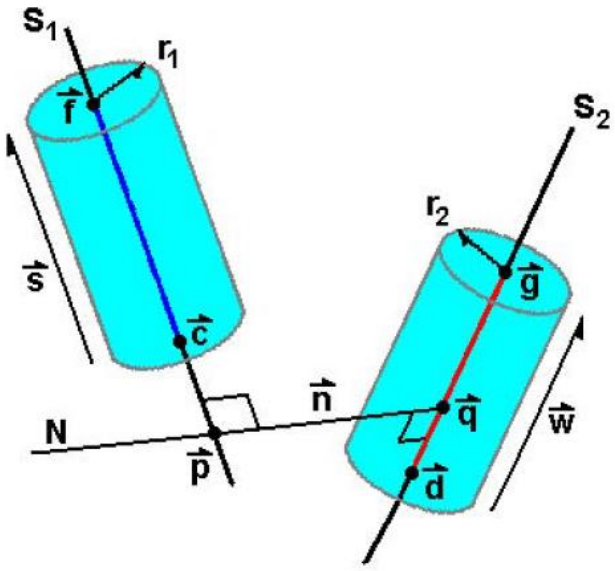

Figure 3.8: Noncoplanar cylinders [114].

3.1.1.3 Capped CNTs

Developed model is also capable of creating capped CNTs. Cap shape is hemisphere (see Figure 3.9).

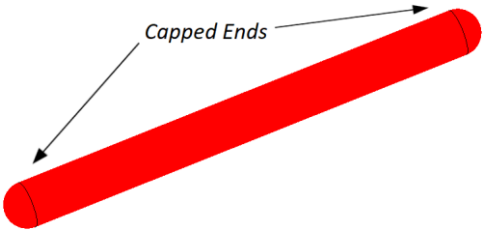

Figure 3.9: Capped CNT.

3.1.2 Generating CCNTs

CCNTs are imagined in cylinders (see Figure 3.10) and distribution, orientation and collision test procedures are the same as straight CNT generation. Developed C++ code ably calculates the start and end points of helical CNTs then this data is imported into in-house developed MATLAB script. MATLAB program creates helical CNTs' surfaces in STL file format and these files are later converted into solids in Parasolid format by utilizing reverse engineering software Geomagic Design X.

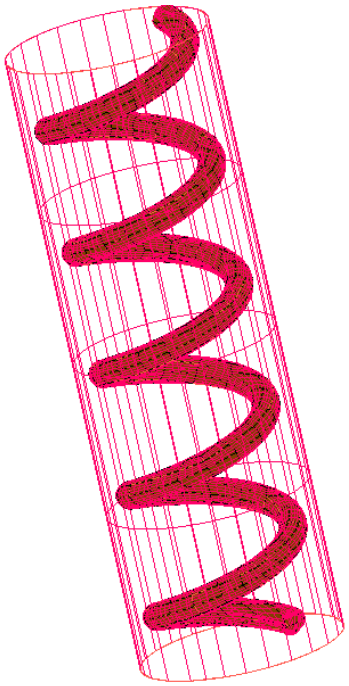

Figure 3.10: Helical CNT conceived in imaginary cylinder.

See Figure 3.11 for depiction of helix. The parametric equations of helix are given below [115],

$$x(t) = \mathrm{a_h}\cos(t)$$

$$y(t) = \mathrm{a_h}\sin(t)$$

$$z(t) = b_h t \tag{3.9}$$

where t from 0 to 2π means one revolution of helix, a_h is the circular radius of helix and $2\pi b_h$ is equal to pitch of the helix [115].

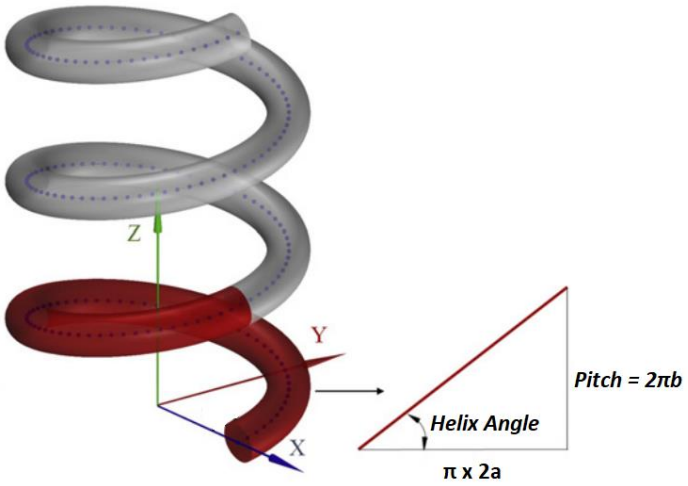

Figure 3.11: Depiction of helix [106].

Helix equation is rotated in y and z axes, respectively. Equation 3.10 shows rotation matrices for y and z axes [116].

$$R_y\,(\varphi) = \begin{bmatrix} \cos\varphi & 0 & \sin\varphi \\ 0 & 1 & 0 \\ -\sin\varphi & 0 & \cos\varphi \end{bmatrix}$$

$$R_z(\theta) = \begin{bmatrix} \cos\theta & -\sin\theta & 0 \\ \sin\theta & \cos\theta & 0 \\ 0 & 0 & 1 \end{bmatrix} \tag{3.10}$$

where φ and θ are azimuth and inclination angles, respectively.

Orientation in 1D or 3D can also be applied to CCNT (see Figures 3.12 and 3.13).

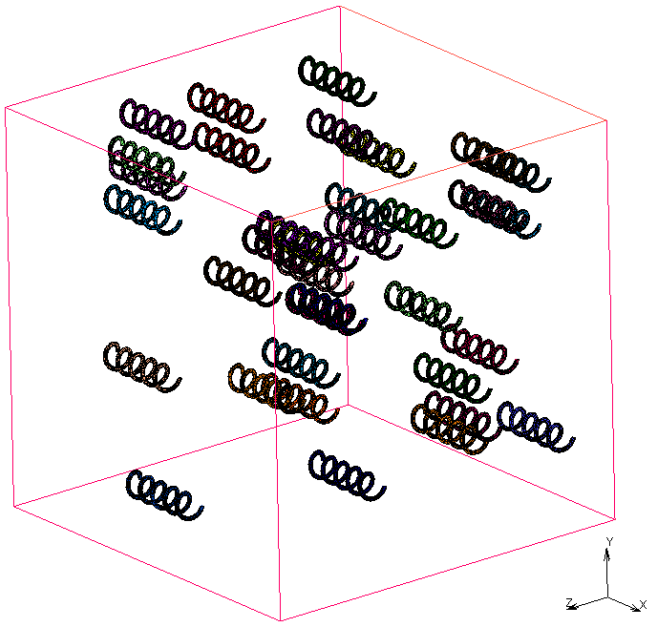

Figure 3.12: 1D aligned CCNTs in an RVE.

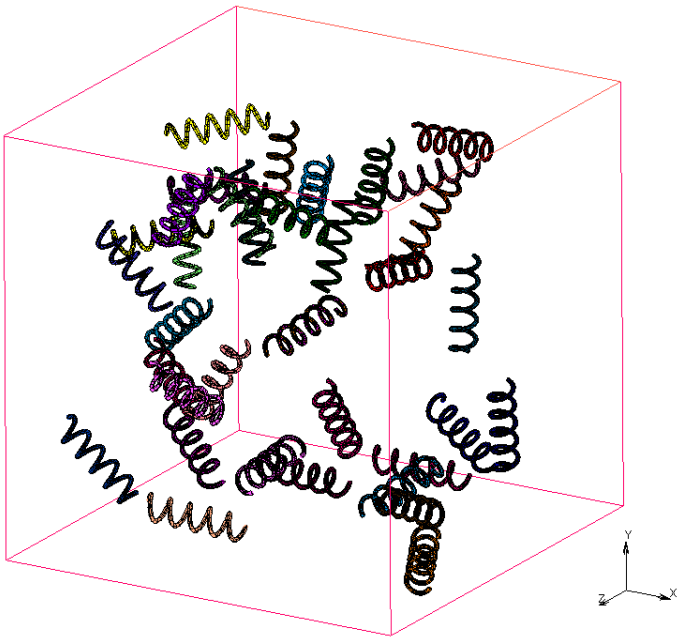

Figure 3.13: 3D aligned CCNTs in an RVE.

3.2 Meso-Scale FE Modelling of CNTRP

Commercial FEA software MSC Marc-Mentat 2021.3 is chosen for this study. The details of the FEA are explained in the following subsections.

3.2.1 Consistent Units

Table 3.1 shows the units used in FEA.

Table 3.1: *Consistent units used in FEA.*

Quantity	Units
Length	nm
Area	nm^2
Force	N x 10^{-8}
Pressure	10^4 MPa
Moment	N.nm x 10^{-8}
Area Moment of Inertia	nm^4
Density	($N.s^2$ x 10^{-8}) / nm^4
Time	s
Mass	kg x 10

3.2.2 Boundary Conditions

Periodic boundary condition (PBC) [117] is not preferred in this study due to its relatively complex boundary conditions. Strain energy density approach [118] is used instead which is quite straightforward. Equation 3.11 is the relation between elastic constants and strain energy. Figure 3.14 and Table 3.2 demonstrate the applied boundary conditions. Since we are only dealing with elastic properties, strain is taken as 1 %.

$$Strain\ Energy = \frac{E_{ijkl}\varepsilon_{kl}^2}{2} x\ Volume \tag{3.11}$$

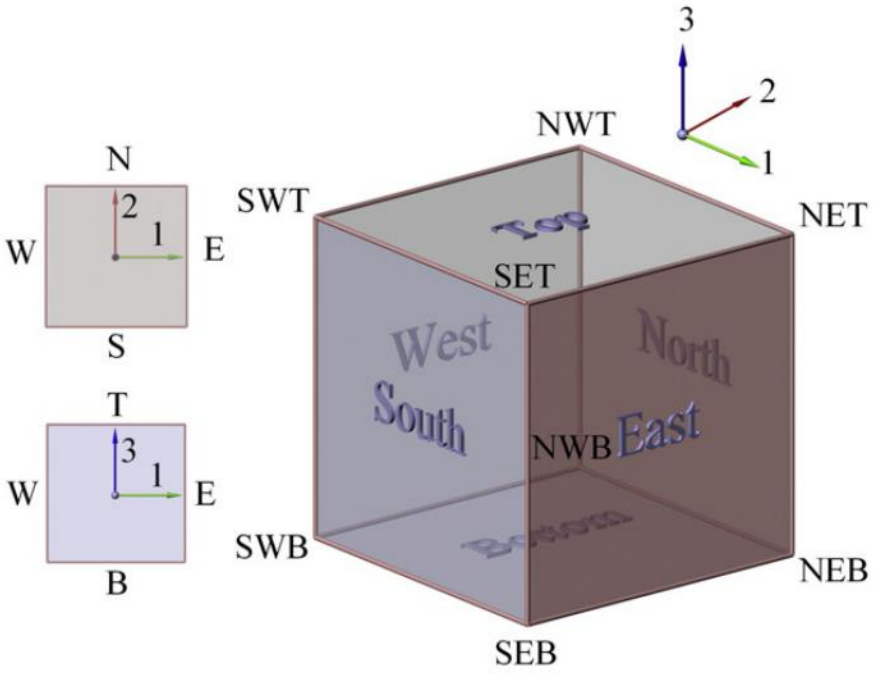

Figure 3.14: 6-faces of RVE [106].

Table 3.2: *Strain energy density approach boundary conditions* [118].

Tensile 1	Tensile 2	Tensile 3
$East$: $u_1 = \varepsilon_{11}\, x\, L$	$East$: $u_1 = 0$	$East$: $u_2 = 0$
$West$: $u_1 = 0$	$South$: $u_2 = 0$	$North$: $u_2 = 0$
$North$: $u_2 = 0$	$North$: $u_2 = \varepsilon_{22}\, x\, L$	Top: $u_3 = \varepsilon_{33}\, x\, L$
$Bottom$: $u_3 = 0$	$Bottom$: $u_3 = 0$	$Bottom$: $u_3 = 0$
Shear 12	Shear 13	Shear 23
$East$: $u_2 = \varepsilon_{12}/4\ x\, L$	$East$: $u_3 = \varepsilon_{13}/4\ x\, L$	$North$: $u_3 = \varepsilon_{23}/4\ x\, L$
$North$: $u_1 = \varepsilon_{12}/4\, x\, L$	Top: $u_1 = \varepsilon_{13}/4\, x\, L$	Top: $u_2 = \varepsilon_{23}/4\, x\, L$
$South$: $u_1 = -\varepsilon_{12}/4\, x\, L$	$Bottom$: $u_1 = -\varepsilon_{13}/4\, x\, L$	$Bottom$: $u_2 = -\varepsilon_{23}/4\, x\, L$
$West$: $u_2 = -\varepsilon_{12}/4\, x\, L$	$West$: $u_3 = -\varepsilon_{13}/4\, x\, L$	$South$: $u_3 = -\varepsilon_{23}/4\, x\, L$
$Bottom$: $u_3 = 0$	$North$: $u_2 = 0$	$West$: $u_1 = 0$

3.2.3 Epoxy Matrix Modelling

Epoxy polymer possesses high density and because of this it can be modelled as continuum [68]. It has been modelled as isotropic linear-elastic material using 4-node 3D tetrahedron element (Element type 134) [119]. The elastic properties of epoxy are taken from [79] and the Young's modulus and Poisson's ratio are 10 GPa and 0.3, respectively.

3.2.4 CNT Reinforcement Modelling

At meso-scale FEAs various researchers have modelled CNTs as solid cylinders [103], [104], [106] and in this study the same assumption is made. In reality CNTs are transversely isotropic materials but it is shown that modelling them as isotropic material is rational [120]. Element type 134 is used for modelling CNTs [119]. The mechanical properties of pristine CNTs are taken from [121] (such as (6,6) armchair as $E_{CNT} = 0.881\ TPa, \nu_{CNT} = 0.279$) and the wall thickness of CNT is taken as 0.34 nm [74]. Young's modulus of CNT belong to tube structure and the values are converted into solid cylinder by exploiting Equation 3.12 [122].

$$E_{LEF} = \frac{A_{CNT}}{A_{LEF}} E_{CNT} \tag{3.12}$$

where E_{LEF}, E_{CNT}, A_{LEF}, A_{CNT} are effective fibre and CNT Young's moduli, effective fibre and CNT cross-sectional areas, respectively.

3.2.5 Modelling the Interface Region Between CNT and Epoxy

Zero-thickness interface elements were used by many researchers to model the region between CNT and epoxy [104], [123]–[125]. 6-node 3D interface elements (Element type 192) are utilized to model interface region. Marc-Mentat offers various cohesive models such as bilinear, exponential and linear-exponential (see Figure 3.15) [126]. Bilinear cohesive model is the most popular model in the literature for modelling CNT-epoxy interface and researchers stated that rather than the type of interface model, the entered cohesive zone parameters are more influential [124] therefore bilinear model is used in this thesis.

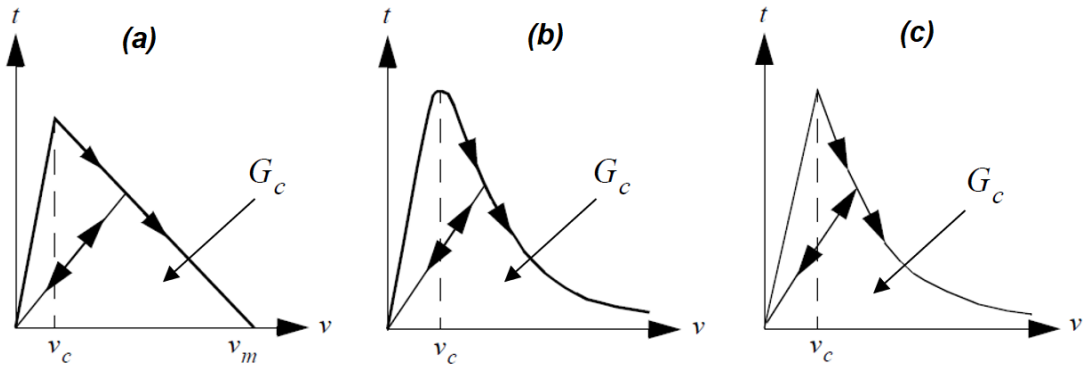

Figure 3.15: (a) Bilinear, (b) exponential and (c) linear-exponential cohesive models [126].

Figure 3.15 shows typical traction-separation curves. At v_c displacement traction becomes maximum and after that point stiffness of the interface decreases and reaches to 0 at v_m which means complete separation. It should be noted that until v_c the deformation is elastic and any further separation results in permanent deformation. G_c stands for cohesive energy and it is equal to the area under traction-separation curve [126].

In this study only van der Waals interaction is considered. Interface properties in normal direction are taken from [127]. v_c, G_c and maximum stress are given as 0.0542 nm, 0.107 J/m^2 and 479 MPa, respectively. v_m is calculated considering bilinear cohesive model (see Figure 3.16).

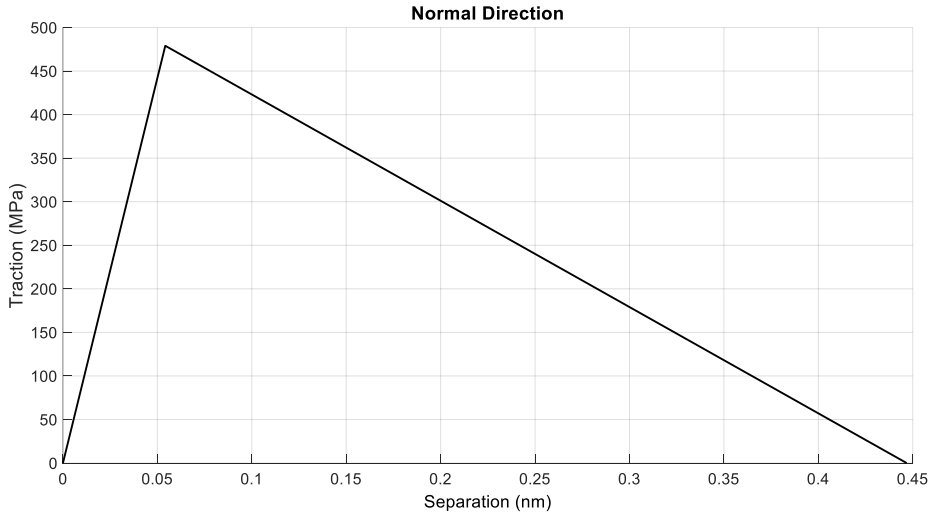

Figure 3.16: Traction-separation curve in normal direction.

Rafiee and Mahdavi [39] performed molecular dynamics simulation and calculated maximum shear stress as 278 MPa. Rafiee and Zehtabzadeh [123] took G_c as 0.256 J/m^2 for tangential stress. v_m is calculated by considering bilinear model and v_c is calculated by keeping the ratio of v_c/v_m same in normal and tangential directions (see Figure 3.17).

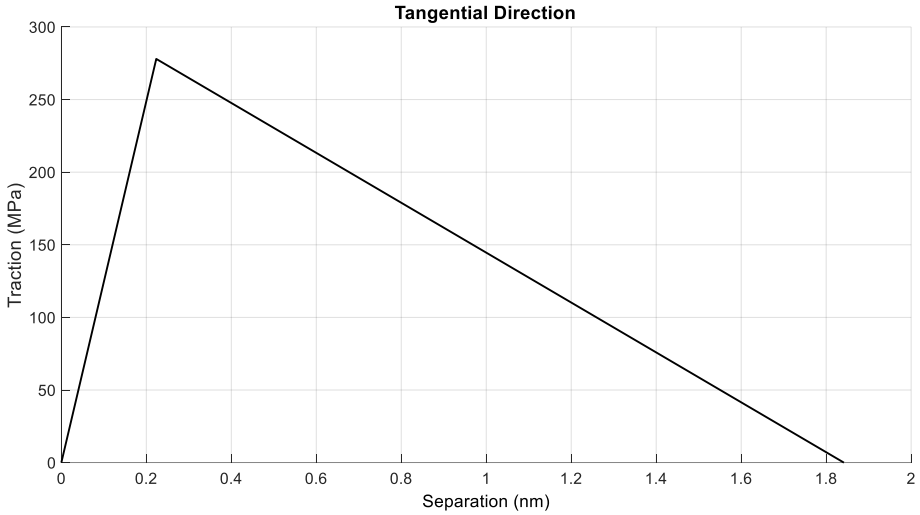

Figure 3.17: Traction-separation curve in tangential direction.

See Appendix B for detailed cohesive interface data.

CHAPTER 4

RESULTS AND DISCUSSION

In this chapter FEAs results are presented on graphs. Furthermore, FEA results are compared and validated by analytical micromechanics models. The influence of CNT volume fraction, end structure (capped or blunt), orientation and geometric properties of CCNT on the elastic mechanical properties of CNTRP is investigated. Table 4.1 shows the geometric properties of CCNTs which are used in three case studies.

Table 4.1: *Geometric Features of CCNTs*.

Case Study	Helix Angle (Degree)	Number of Revolutions	CNT Outer Diameter (nm)	CNT Length (nm)
Helix Angle	30, 60, 90	3	1.154	34.62
Number of Revolutions	30	3, 4, 5	1.154	34.62, 46.16, 57.7
CNT Diameter	30	5	1.154, 1.696, 1.967	57.7

The mechanical properties of CNTs are acquired from reference [121] and Young's moduli are converted into solid fibre Young's moduli (see Table 4.2).

Table 4.2: *Properties of CNTs which are used in FEAs.*

Chirality	CNT Diameter (nm)	CNT Outer Diameter (nm)	$E_{CNT}\ (TPa)$	$E_{LEF}\ (TPa)$	v_{CNT}
(6,6)	0.814	1.154	0.881	0.732	0.279
(10,10)	1.356	1.696	0.883	0.566	0.254
(12,12)	1.627	1.967	0.883	0.505	0.250

Sensitivity analysis is performed to decide minimum mesh density. The sensitivity analysis is performed on 1% volume fraction, capped SWNT reinforced composite. Matlab's piecewise cubic Hermite interpolation is used for fitting data (see Figure 4.1). See Appendix C for sensitivity analysis data.

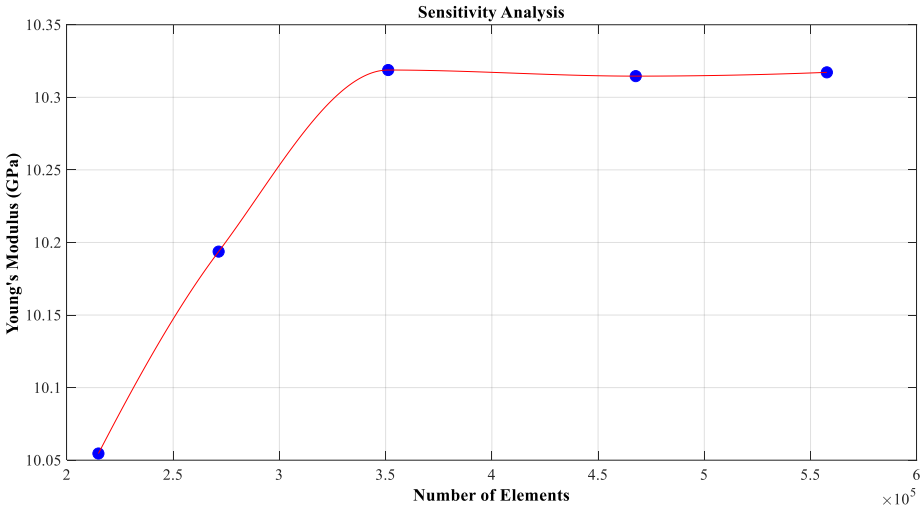

Figure 4.1: Sensitivity Analysis.

In all of the FEAs the side length of the cubic RVE is equal to 50 nm.

4.1 Effect of CNT Volume Fraction

Only SWNT reinforced composites are analysed in this case study. CNTs are completely randomly oriented and distributed inside the RVE, thus the composite behaves like an isotropic material. The RVE is stretched in 3-cartesian coordinates and the arithmetic mean of Young's moduli and Poisson's ratios are calculated. Moreover, Poisson's ratio is evaluated by calculating the average displacement of nodes on the contracting surfaces. Figure 4.2 shows that the FEAs results are inside the rule of mixtures and Hashin-Shtrikman bounds. In addition to this, FEAs indicate that reinforcement ratio of CNTRP increases with rise in CNT volume fraction.

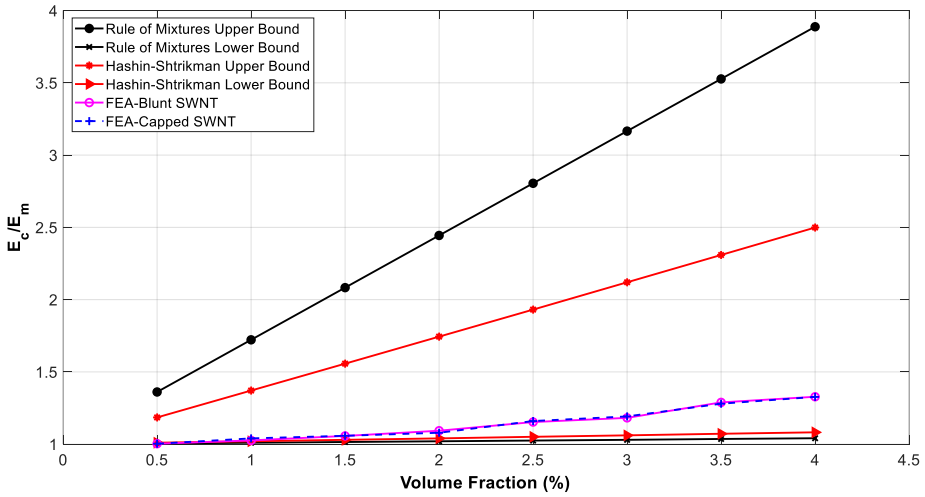

Figure 4.2: Reinforcement ratio comparison of analytical micromechanics bounds and FEAs.

Figure 4.3 presents a collection of micromechanics models and FEAs.

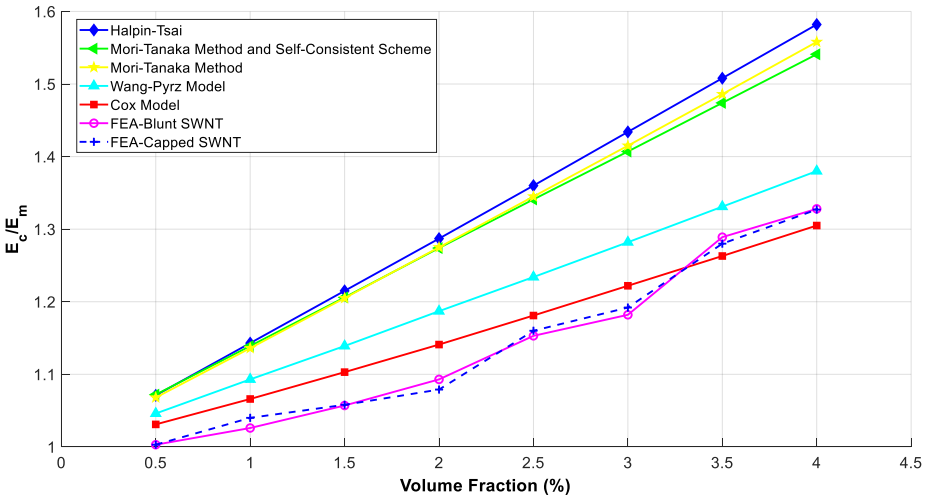

Figure 4.3: Young's moduli ratio comparison of various micromechanics models and FEAs.

Among micromechanics models, Wang-Pyrz and Cox model showed closer estimations to FEAs, but Cox model started to underestimate FEAs after 3% volume fraction. Mori-Tanaka method showed slightly closer estimation than Mori-Tanaka method and self-consistent scheme until 2% but in volume fraction larger than 2% the latter makes better predictions. Halpin-Tsai makes the farthest estimates.

Shear modulus of CNTRP is calculated by Equation 4.1 [128] since the composite is considered isotropic and linear-elastic.

$$G = \frac{E}{2(1+\nu)} \tag{4.1}$$

Figure 4.4 presents shear moduli ratios of FEAs and various micromechanics models.

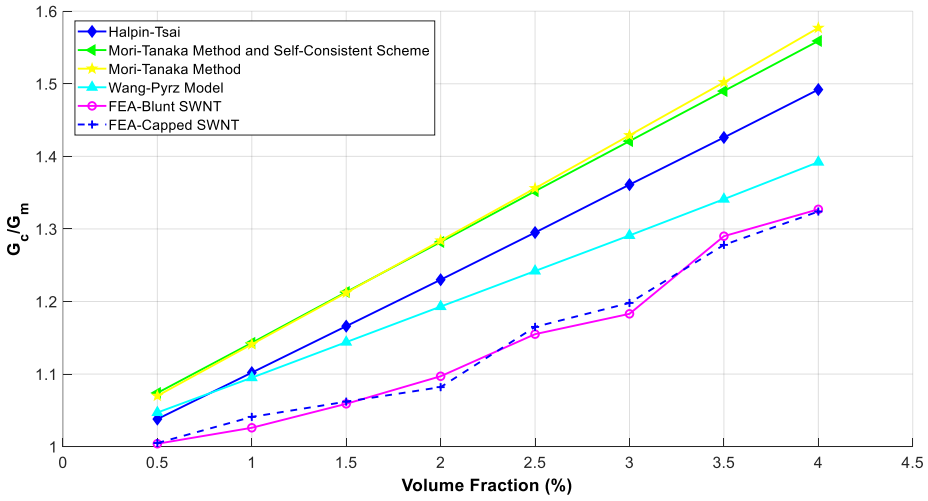

Figure 4.4: Shear moduli ratio comparison of various micromechanics models and FEAs.

In this case, Wang-Pyrz model makes the best estimate. Halpin-Tsai showed closer estimates than Mori-Tanak methods. FEAs indicate that the influence of CNT end structure is negligible and volume fraction is more influential in both Young's and shear moduli. Micromechanics models consider perfect bonding between matrix and fibre, as a result, they overestimated the FEAs results in most of the cases.

Mori-Tanaka methods and Wang-Pyrz model makes rather closer predictions of Poisson's ratios than Halpin-Tsai (see Figure 4.5).

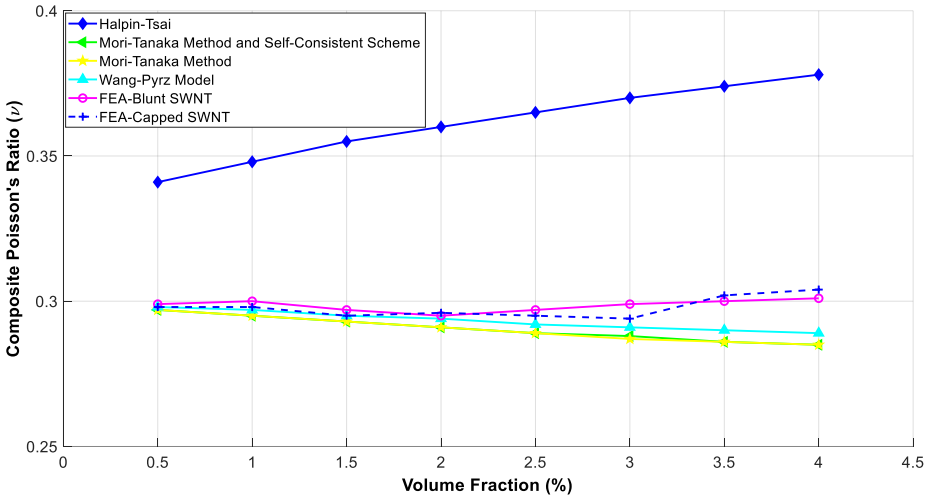

Figure 4.5: Poisson's ratio comparison of micromechanics models and FEAs.

Figures 4.6 and 4.7 present maximum equivalent Von Mises stress and maximum equivalent elastic strain in CNT for blunt and capped SWNT reinforced composite cases respectively. The trendlines demonstrate increase in max. stress and max. strain with increase in volume fraction for both blunt and capped-SWNT reinforced composite cases.

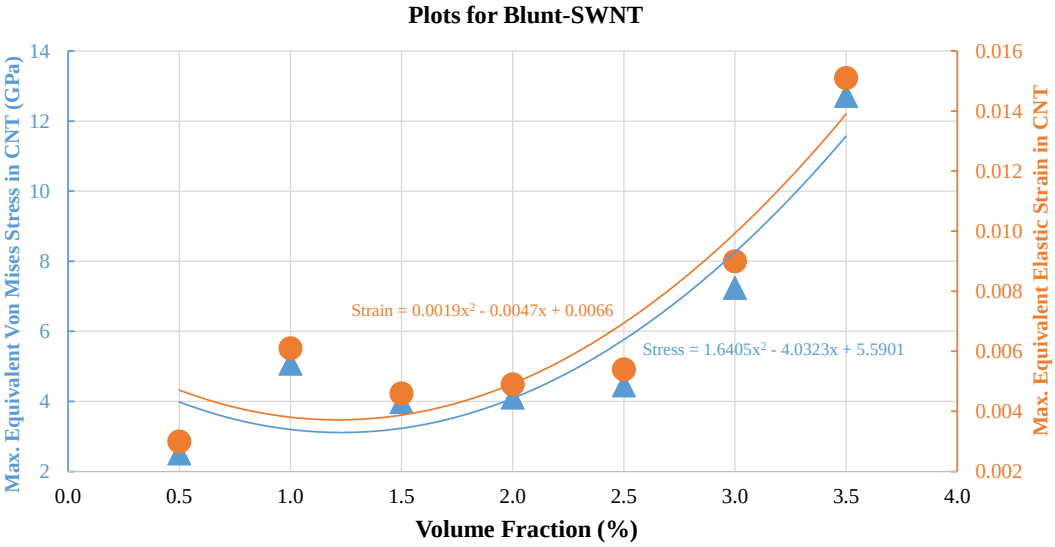

Figure 4.6: Max. Von Mises stress and max. elastic strain in CNT in blunt SWNT case.

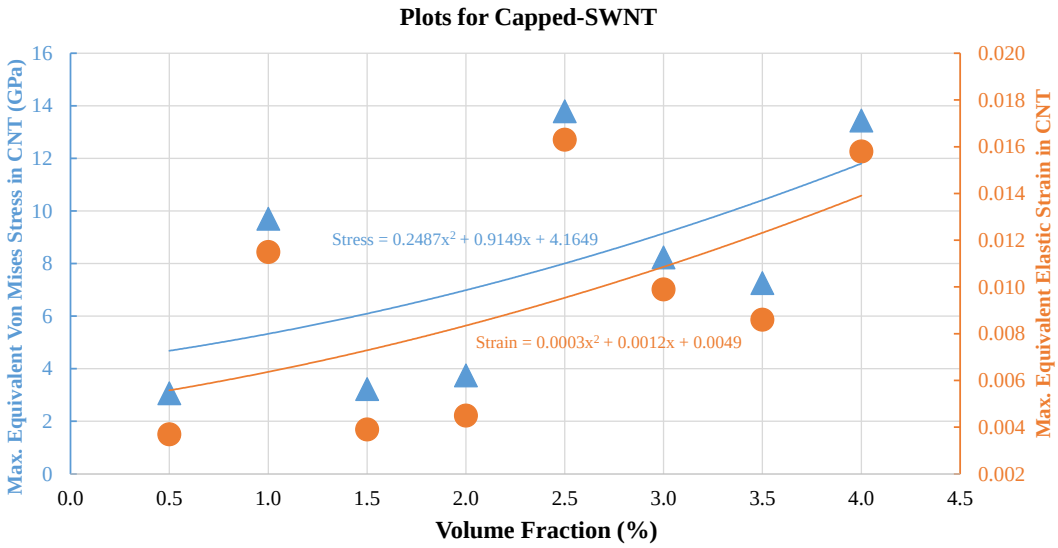

Figure 4.7: Max. Von Mises stress and max. elastic strain in CNT in capped SWNT case.

Figures 4.8, 4.9 and 4.10 are some screenshots taken from 2.5% volume fraction, blunt-SWNT reinforced composite FEAs. In these figures the RVE is stretched along y-axis.

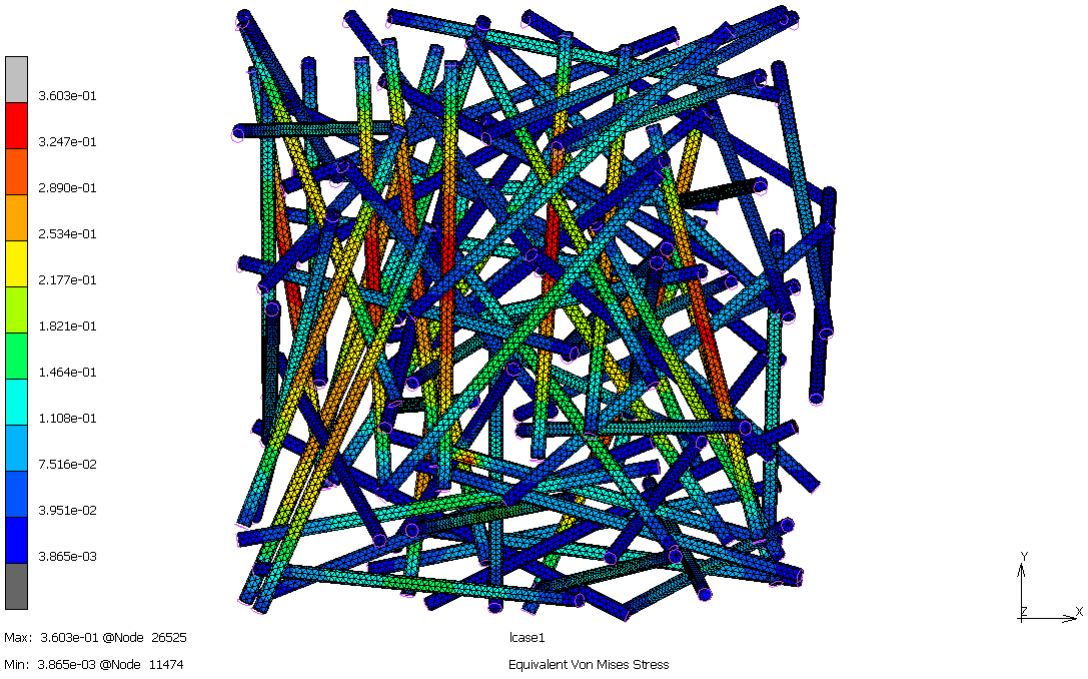

Figure 4.8: Equivalent Von Mises stress distribution on CNTs (2.5%, blunt-SWNT).

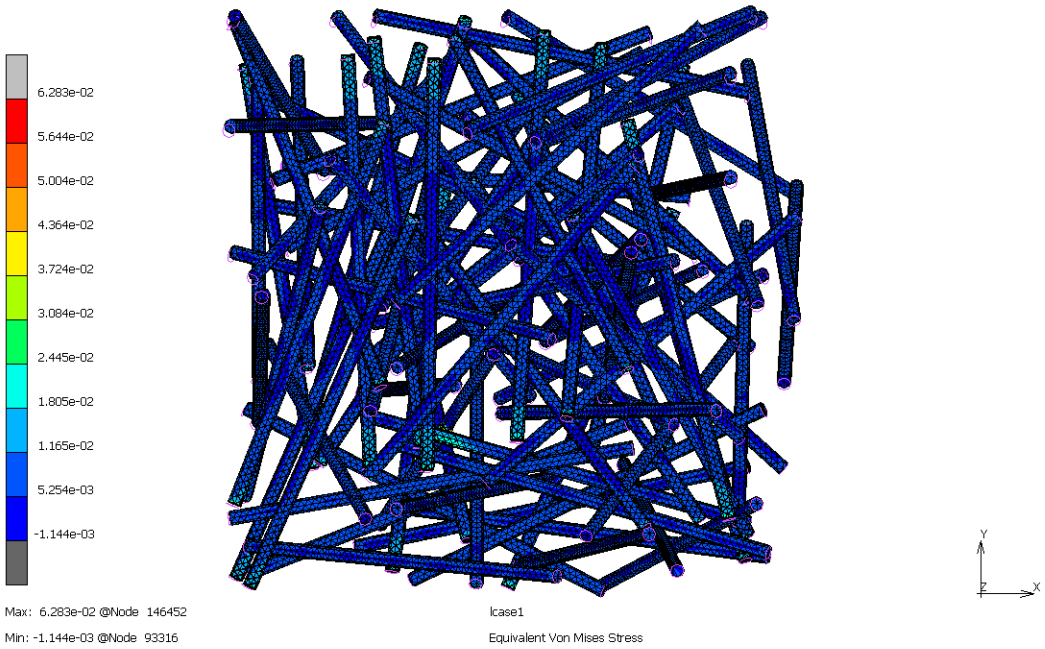

Figure 4.9: Equivalent Von Mises stress distribution on interface (2.5%, blunt-SWNT).

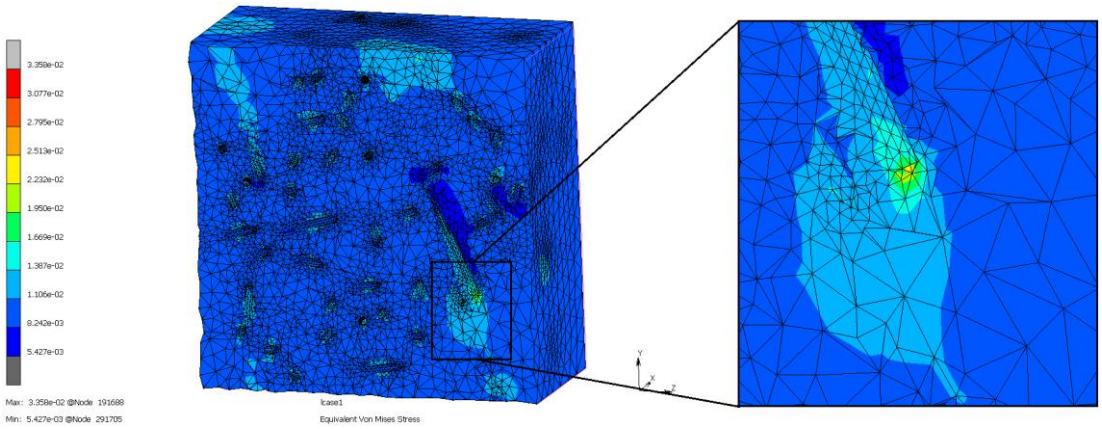

Figure 4.10: Equivalent Von Mises stress distribution on half matrix (2.5%, blunt-SWNT).

Figure 4.10 zoomed in the rise in Von Mises stress at the vicinity of CNT tip. Figures 4.11 and 4.12 depict the generated mesh for 4% volume fraction capped-SWNT and half matrix, respectively.

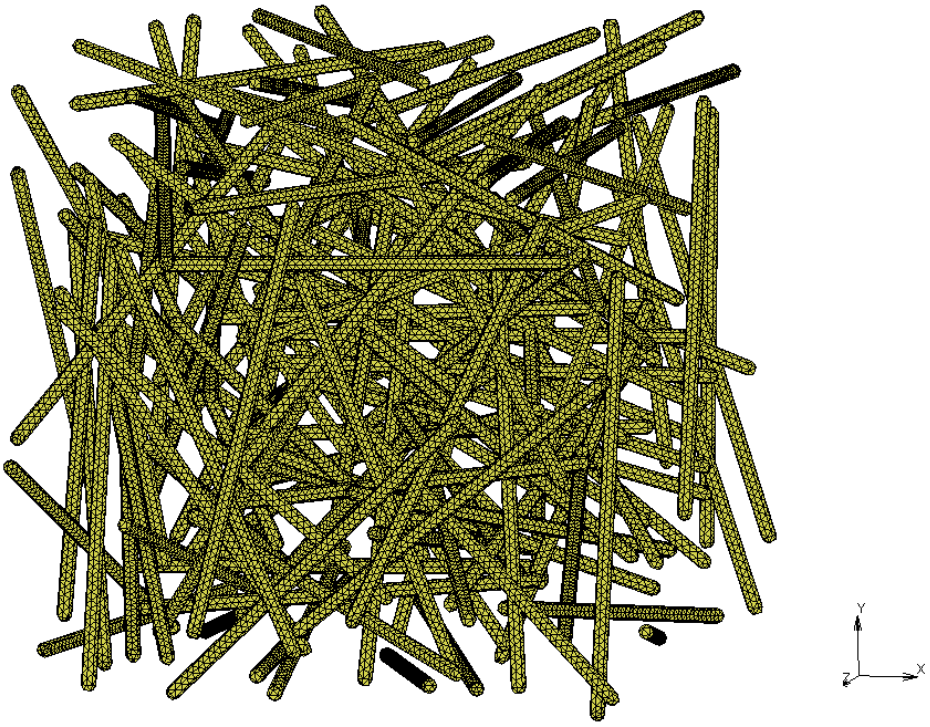

Figure 4.11: Generated mesh for CNTs (4%, capped-SWNT).

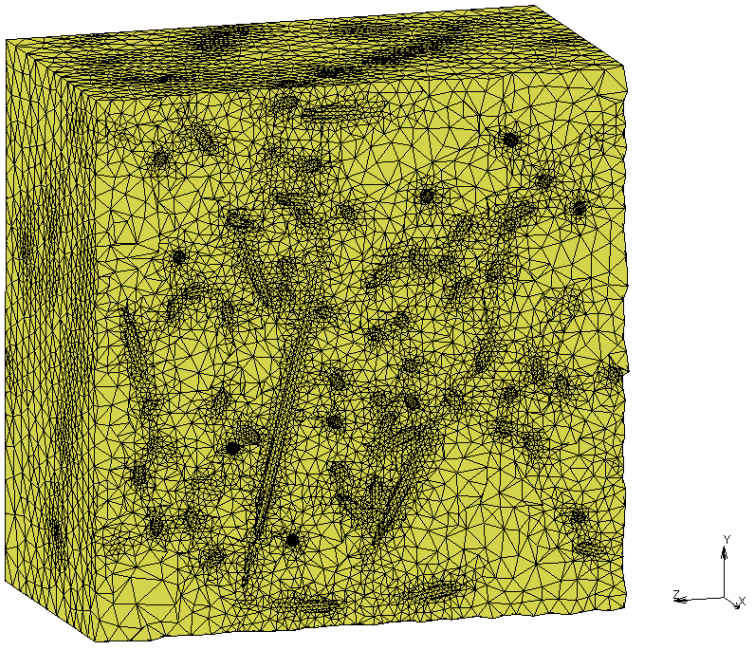

Figure 4.12: Generated mesh for half matrix (4%, capped-SWNT).

The applied boundary conditions when the RVE is stretched along x-axis are shown in Figure 4.13.

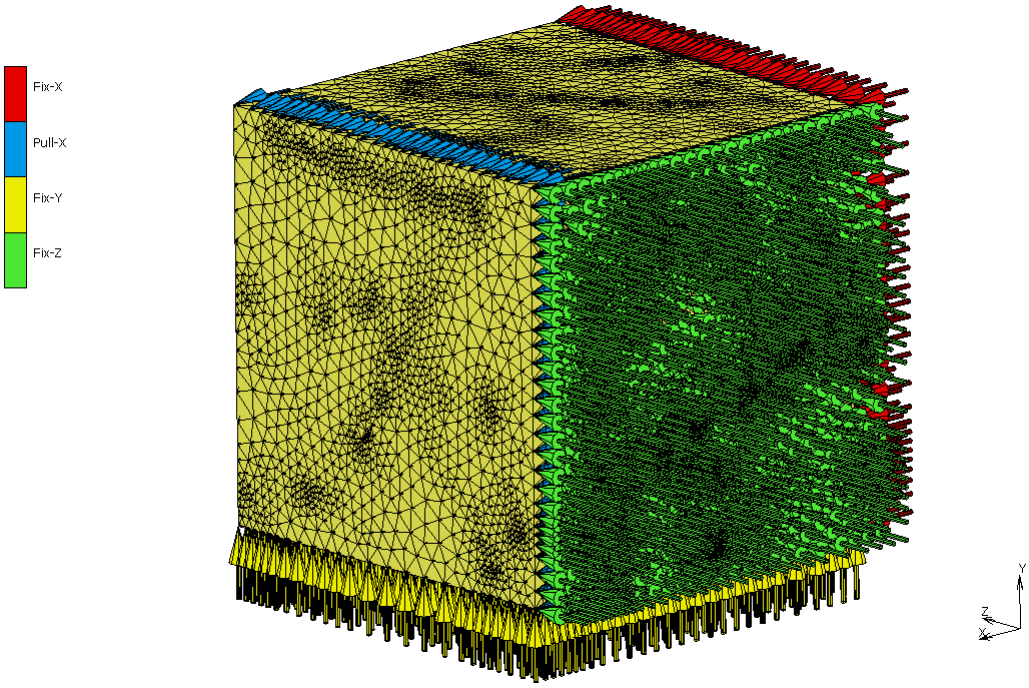

Figure 4.13: The boundary conditions applied when the RVE is stretched along x-axis.

4.2 Effect of CCNT Geometry

Three different geometrical features of CCNT have been analysed in this study. These features are helix angle (see Figure 4.14), number of revolutions (see Figure 4.15) and chirality (see Figure 4.16). In this section, merely blunt-CCNT reinforced composites are modelled with a volume fraction of 1%.

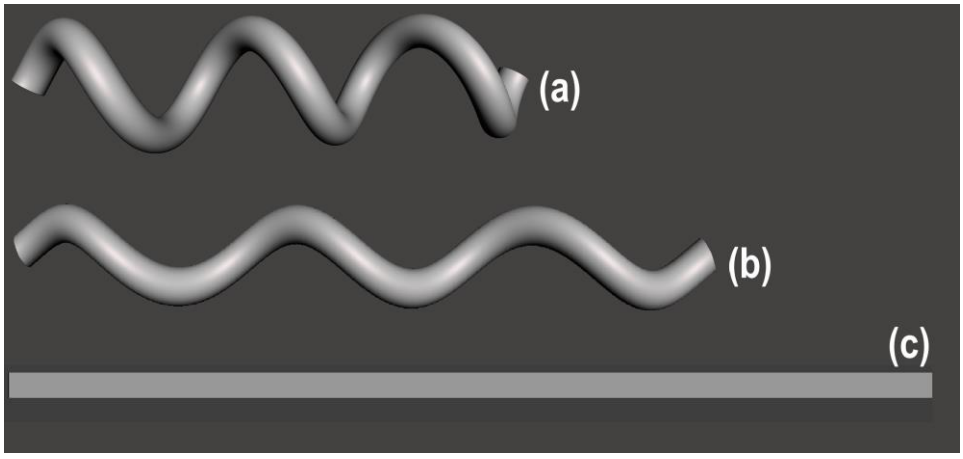

Figure 4.14: CCNTs with helix angle (a) 30°, (b) 60° and (c) 90°.

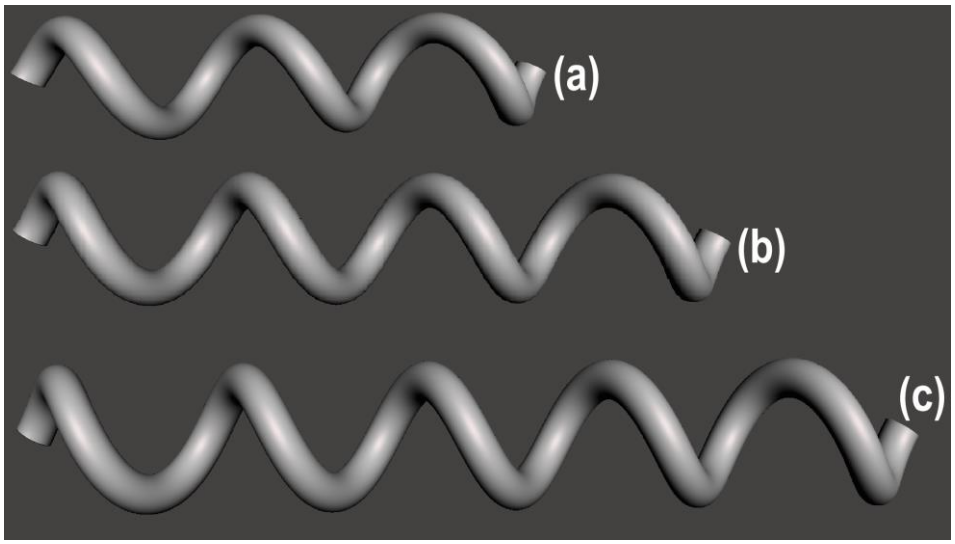

Figure 4.15: CCNTs with (a) 3, (b) 4 and (c) 5 revolutions.

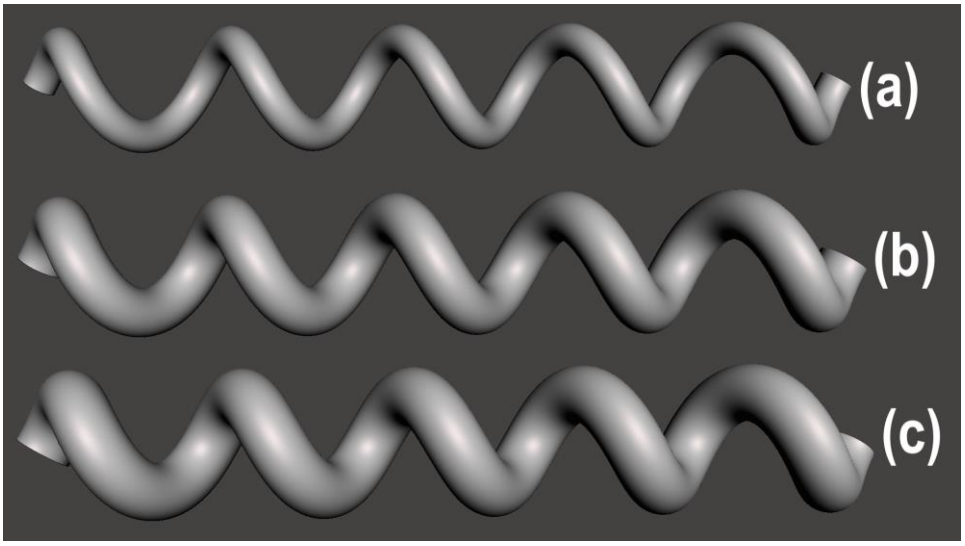

Figure 4.16: CCNTs with (a) (6,6), (b) (10,10) and (c) (12,12) chirality.

4.2.1 Randomly Oriented CNTs Case

In this case, CNTs are randomly oriented inside the RVE and because of this composite is considered as an isotropic material. Figure 4.17 demonstrates the increase in Young's and shear moduli with increase in helix angle.

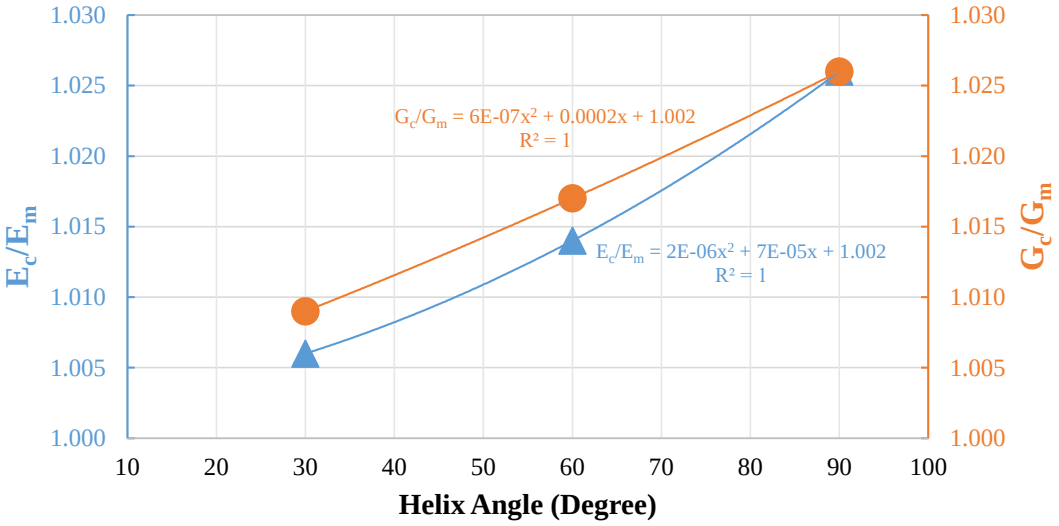

Figure 4.17: Helix angle versus Young's and shear moduli (randomly oriented case).

As the number of revolutions increase Young's and shear moduli also increase (see Figure 4.18).

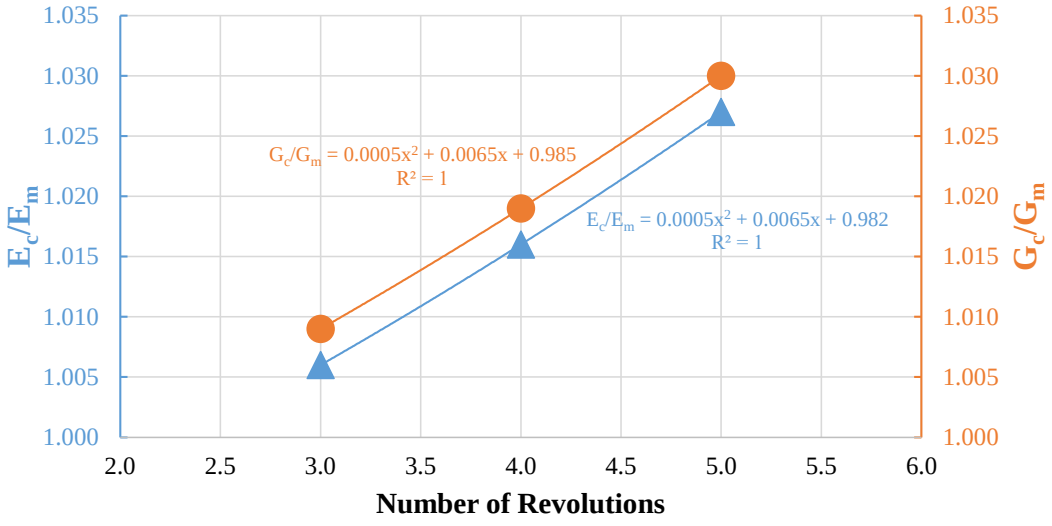

Figure 4.18: Number of revolutions versus Young's and shear moduli (randomly oriented case).

On the other hand, increasing CNT diameter had detrimental effects on elastic mechanical properties of CNTRP (see Figure 4.19).

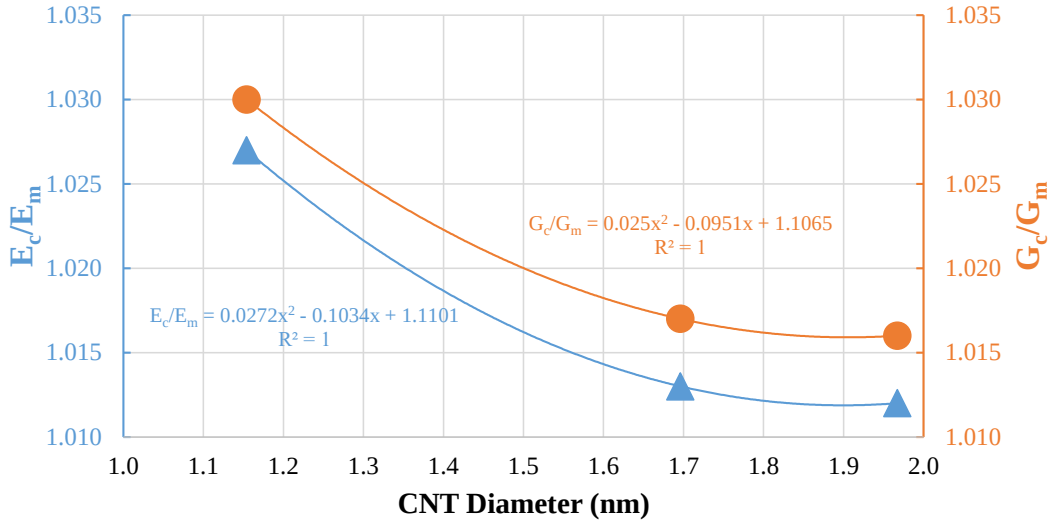

Figure 4.19: CNT diameter versus Young's and shear moduli (randomly oriented case).

The rise in the number of revolutions and CNT diameter has slightly decreased the composite Poisson's ratio (see Figures 4.20 and 4.21), whereas rise in helix angle marginally increased composite Poisson's ratio (see Figure 4.22).

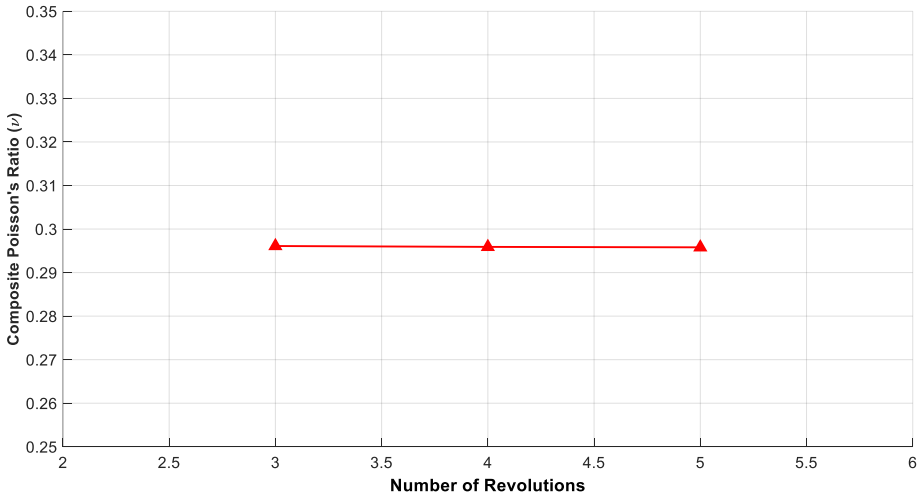

Figure 4.20: Composite Poisson's ratio versus number of revolutions.

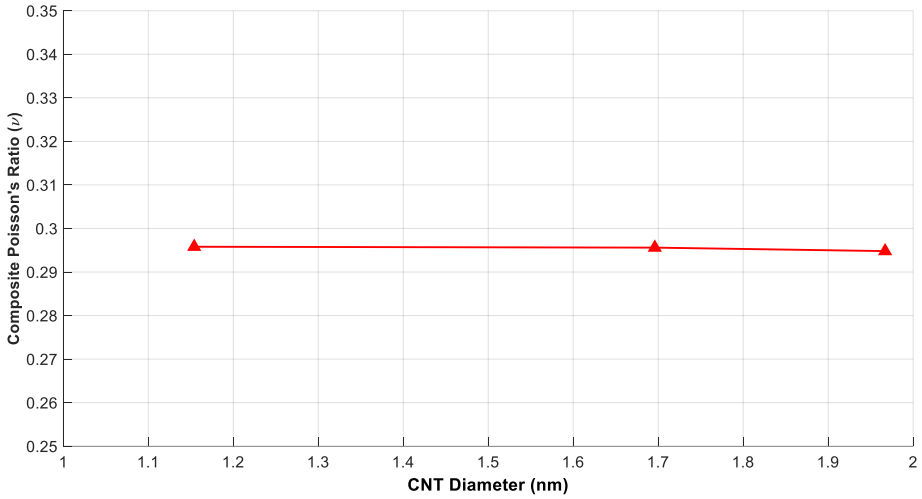

Figure 4.21: Composite Poisson's ratio versus CNT diameter.

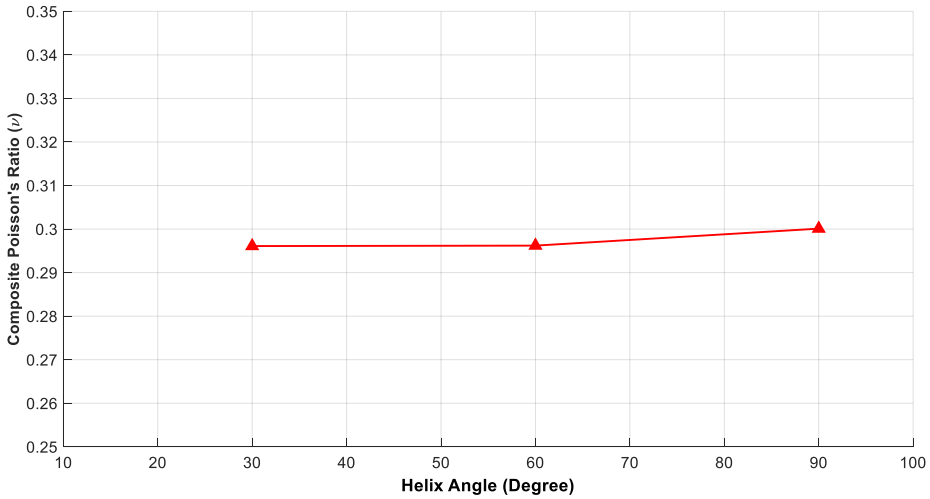

Figure 4.22: Composite Poisson's ratio versus helix angle.

4.2.2 Aligned CNTs Case

In this case study CNTs are aligned along x-axis (or direction-1) and therefore the composite is considered as a transversely isotropic material. Directions 1, 2 and 3 refer to x, y and z axes respectively. E_{22} is the mean of sum of E_{22} and E_{33}. In this section the term "Reinforcement Ratio" refers to the ratio of elastic constant of composite to elastic constant of matrix.

Increase in helix angle plummeted E_{11} but decreased E_{22}, G_{12} and G_{23} (see Figure 4.23). Halpin-Tsai made the closest estimation among micromechanics models (see Figure 4.23).

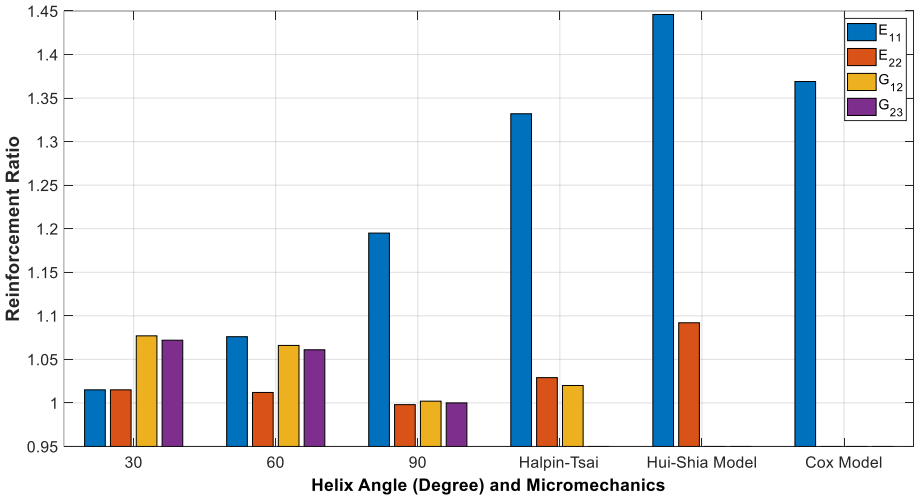

Figure 4.23: Reinforcement ratio versus helix angle and micromechanics models (aligned case).

Increasing the number of revolutions had positive effects on all elastic properties (see Figure 4.24).

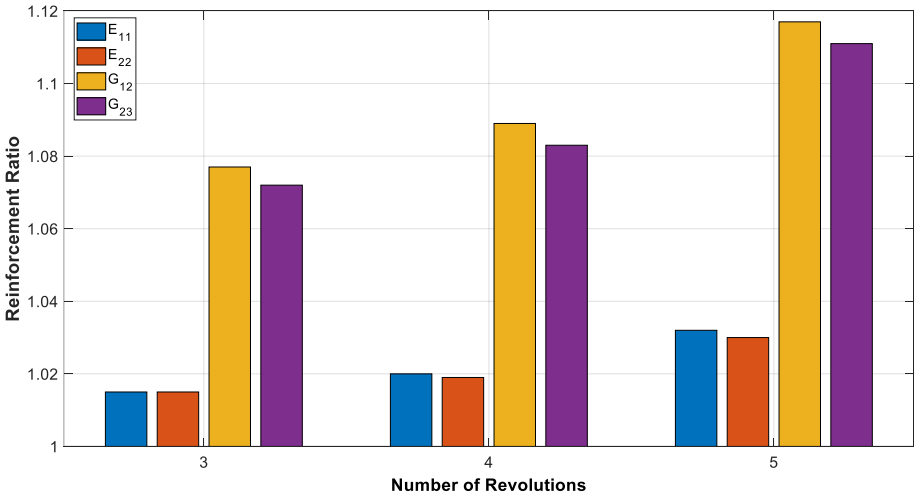

Figure 4.24: Reinforcement ratio versus number of revolutions (aligned case).

Increasing CNT diameter had detrimental effects on all elastic properties (see Figure 4.25).

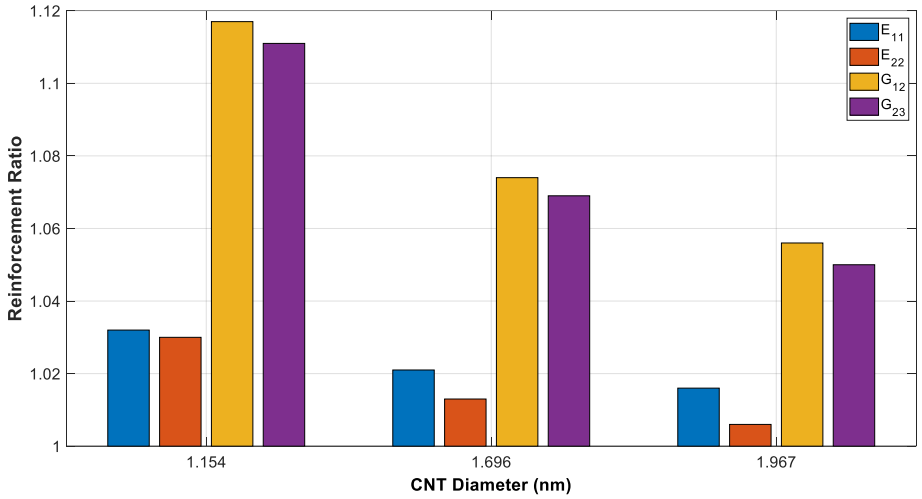

Figure 4.25: Reinforcement ratio versus CNT diameter (aligned case).

Composite's Poisson' ratio ν_{12} is calculated by taking the average of ν_{12} and ν_{13}. Increasing helix angle increases ν_{12} (see Figure 4.26) however rise in the number of revolutions and CNT diameter, reduced ν_{12} (see Figures 4.27 and 4.28).

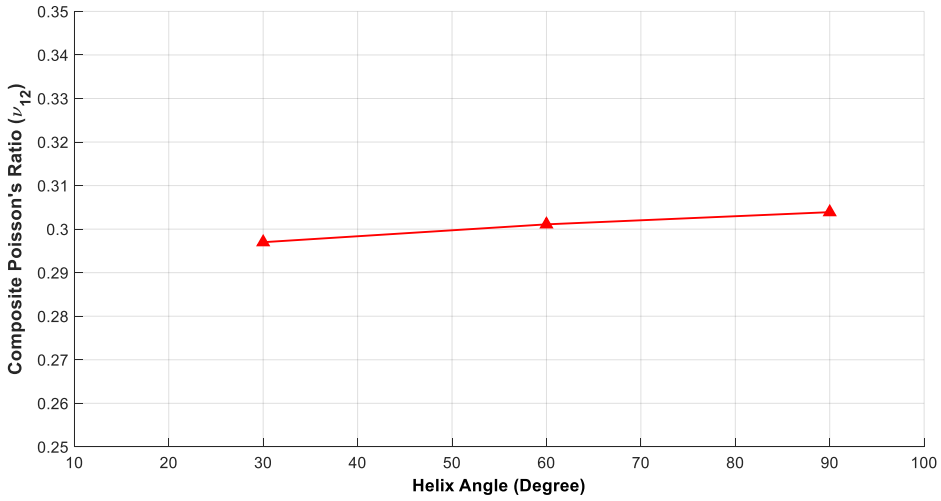

Figure 4.26: Composite ν_{12} versus helix angle.

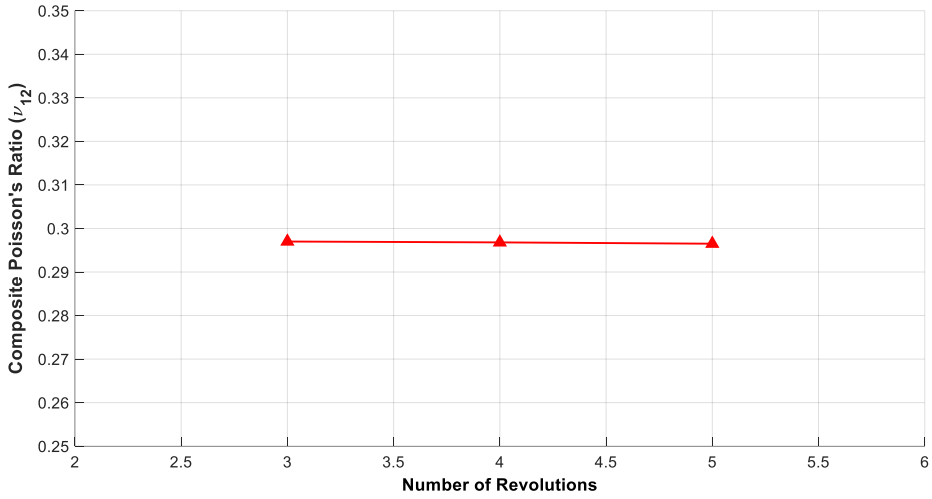

Figure 4.27: Composite ν_{12} versus number of revolutions.

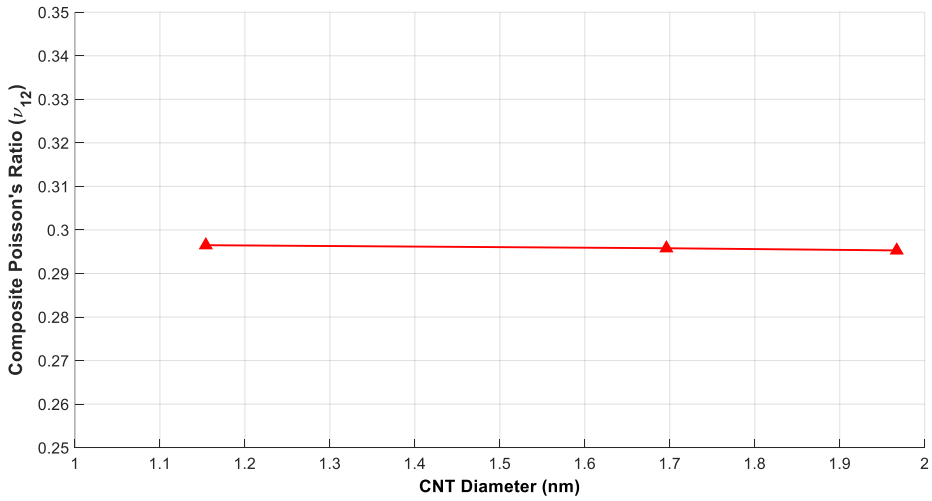

Figure 4.28: Composite ν_{12} versus CNT diameter.

Figures 4.29, 4.30 and 4.31 depicts the FEAs results obtained from randomly oriented 5 revolution (6,6) CCNT model. These figures show loading in y-direction. Figure 4.31 zooms in to show increase in Von Mises stress at the vicinity of CCNT.

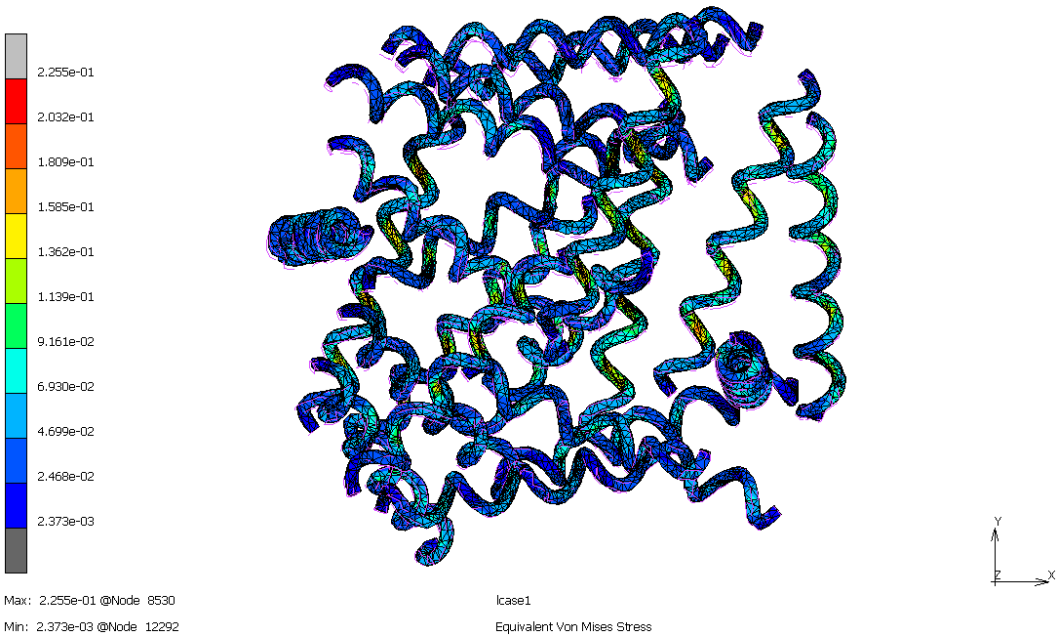

Figure 4.29: Equivalent Von Mises stress distribution on CCNTs (5 revolutions, (6,6), randomly oriented case).

Figure 4.30: Equivalent Von Mises stress distribution on interface (5 revolutions, (6,6), randomly oriented case).

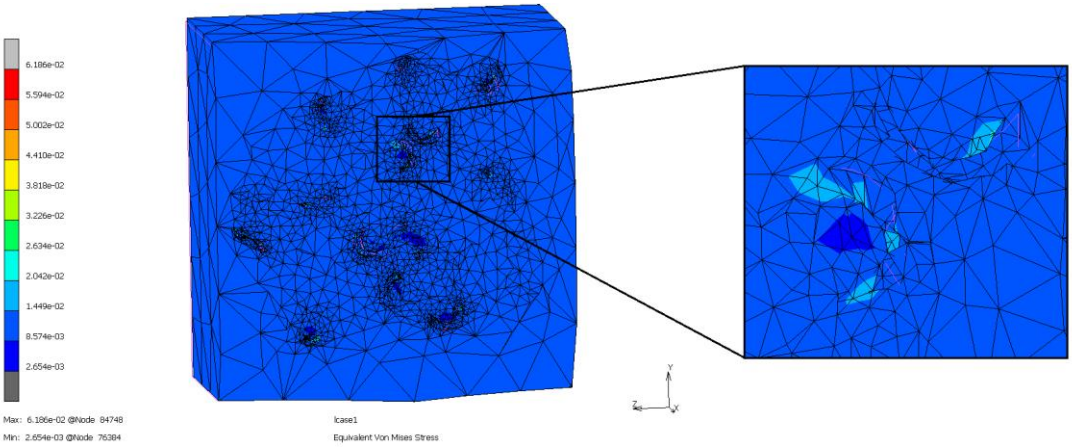

Figure 4.31: Equivalent Von Mises stress distribution on half matrix (5 revolutions, (6,6), randomly oriented case).

Figure 4.32 depicts the applied boundary conditions for calculating G_{12}.

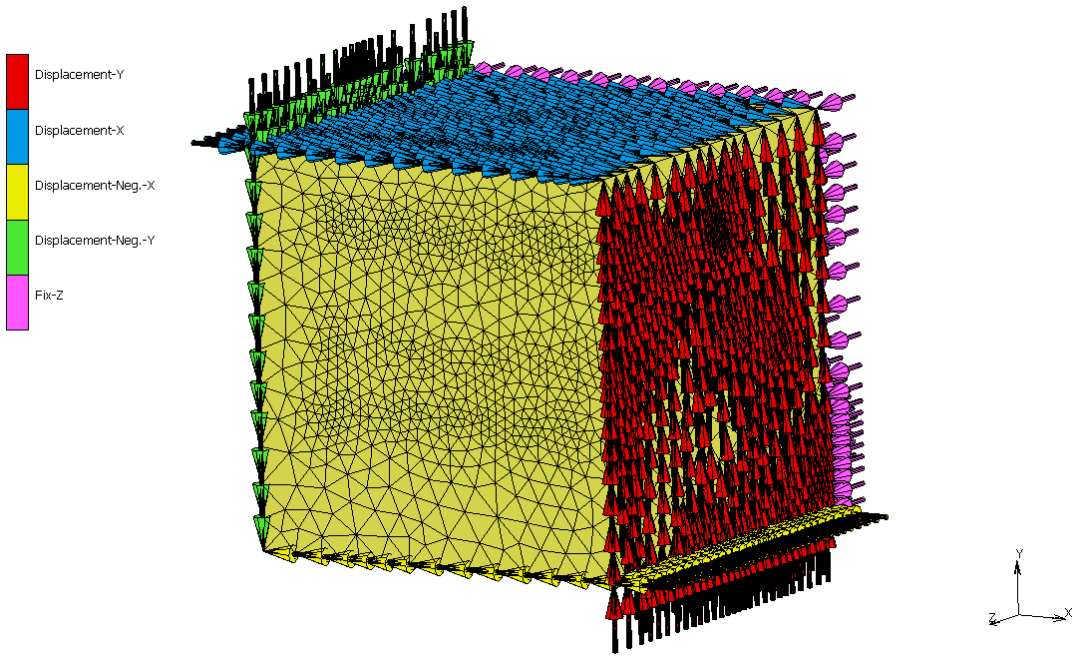

Figure 4.32: Boundary conditions applied for calculating G_{12}.

See Appendices D and E for tabulated FEAs results and detailed information about FEAs, respectively.

CHAPTER 5

CONCLUSIONS

This study demonstrated that increasing CNT volume fraction enhances elastic mechanical properties of CNTRP. The end structure of SWNT (capped or blunt) does not have any substantial effect on elastic properties of nano-composite. Overall, Cox and Wang-Pyrz model made the closet estimation for randomly oriented straight CNT reinforced composite case. All of the micromechanics models overestimated the FEA results except Cox model for volume fraction higher than 3%. The trendlines of max. equivalent Von Mises stress and max. equivalent elastic strain in CNT showed increase with the rise of CNT volume fraction. CNT alignment provides better mechanical property in the alignment direction and Halpin-Tsai had the closest prediction in this particular case. In randomly oriented CNTs case increasing helix angle and number of revolutions had positive effects on elastic properties. However, increasing CNT diameter had detrimental effects on elastic properties. Decreasing helix angle increases shear moduli and Young's modulus in transverse direction of CNTRP in aligned CNTs case. Increasing the number of revolutions had raised the entire elastic constants while increasing the CNT diameter did exactly the opposite in aligned CNTRP case. Increasing number of revolutions and CNT diameter slightly reduces composite's Poisson's ratio (ν and ν_{12}) while increasing helix angle causes a slight raise in composite's Poisson's ratio (ν and ν_{12}).

Author believes to has developed a novel CCNT reinforced epoxy composite FE model at meso-scale. As a result, author's results were compared with the FEA results available in the literature, where author's FEA results behaved in the same manner with the results obtained from CNT reinforced polyethylene [104], [129], [130] or polypropylene [106] matrix. Micro-scale FE models of CNT reinforced epoxy composites available in the literature [79], [121], [124] had estimated Young's modulus higher than this study. However, author believes that the model developed in this study is more realistic because parameters like random location-orientation and coiled shape of CNT were considered.

The main limitation of CNTRP FE models is computational cost. In this study, aspect ratios from 30 to 50 were merely used but in reality CNTs can have aspect ratios as high as 132 million. Performing FEAs of CNTRPs with high aspect ratio and high volume fraction of CNTs is quite time consuming in personal computers.

This study considered only van der Waals interaction between CNT and epoxy. Functionalized CNTRPs can have better interface properties, thus further research which considers functionalized interface is needed. CNT and epoxy matrix inherently have defects and this should be also taken into account in FEAs. Generally, CNTs are not straight and have randomly curved geometries. FE models with wavy CNTs can be developed.

REFERENCES

[1] NASA, “Overview: Weather, Global Warming and Climate Change.” https://climate.nasa.gov/resources/global-warming-vs-climate-change/.

[2] IEA, “Explore energy data by category, indicator, country or region.” https://www.iea.org/data-and-statistics/data-browser?country=WORLD&fuel=CO2 emissions&indicator=CO2BySector.

[3] IEA, “Improving the sustainability of passenger and freight transport.” https://www.iea.org/.

[4] F. C. Campbell, “Introduction and Uses of Lightweight Materials,” *Light. Mater. Underst. Basics*, p. 4, 2012, [Online]. Available: https://www.asminternational.org/documents/10192/1849770/05355G_Sample.pdf.

[5] F. C. Campbell, *Structural Composite Materials*, First Edit. ASM International, 2010.

[6] J. P. LU and J. HAN, “Carbon Nanotubes and Nanotube-Based Nano Devices,” *Int. J. High Speed Electron. Syst.*, vol. 09, no. 01, pp. 101–123, 1998, doi: 10.1142/s0129156498000063.

[7] S. I. Yengejeh, S. A. Kazemi, and A. Öchsner, *A Primer on the Geometry of Carbon Nanotubes and Their Modifications*. Springer, 2015.

[8] Q. Lu *et al.*, “Determination of Carbon Nanotube Density by Gradient Sedimentation,” *J. Phys. Chem. B*, vol. 110, no. 48, pp. 24371–24376, 2006, doi: 10.1021/jp063660k.

[9] S. Jafari, “Engineering Applications of Carbon Nanotubes,” in *Carbon Nanotube– Reinforced Polymers From Nanoscale to Macroscale*, R. Rafiee, Ed. Elsevier Inc., 2018, pp. 25–40.

[10] T. Deplancke, O. Lame, S. Barrau, K. Ravi, and F. Dalmas, “Impact of carbon nanotube prelocalization on the ultra-low electrical percolation threshold and on the mechanical behavior of sintered UHMWPE-based nanocomposites,” *Polymer (Guildf).*, vol. 111, pp. 204–213, 2017, doi: 10.1016/j.polymer.2017.01.040.

[11] M. Loos, “Applications of CNTs,” in *Carbon Nanotube Reinforced Composites*, Elsevier, 2015, pp. 189–205.

[12] “ISO/TS 80004-1:2015(en), Nanotechnologies — Vocabulary — Part 1: Core terms,” 2015. https://www.iso.org/obp/ui/#iso:std:iso:ts:80004:-1:ed-2:v1:en.

[13] S. Iijima, “Helical microtubules of graphitic carbon,” *Nature*, vol. 354, pp. 56–58, 1991, [Online]. Available: https://www.nature.com/articles/354056a0.

[14] M. Monthioux and V. L. Kuznetsov, “Who should be given the credit for the discovery of carbon nanotubes?,” *Carbon N. Y.*, vol. 44, no. 9, pp. 1621–1623, 2006, doi: 10.1016/j.carbon.2006.03.019.

[15] A. Oberlin, M. Endo, and T. Koyama, “Filamentous Growth of Carbon Through Benzene Decomposition,” *J. Cryst. Growth*, vol. 32, no. 3, pp. 335–349, 1976, doi: 10.1016/0022-0248(76)90115-9.

[16] R. Ghasempour and H. Narei, “CNT Basics and Characteristics,” in *Carbon Nanotube-Reinforced Polymers: From Nanoscale to Macroscale*, R. Rafiee, Ed. Elsevier Inc., 2018, pp. 1–24.

[17] F. Hennrich, C. Chan, V. Moore, M. Rolandi, and M. O’Connell, “The element carbon,” in *Carbon Nanotubes, Properties and Applications*, First Edit., vol. 295–297, M. J. O’Connell, Ed. Taylor & Francis, 2006, pp. 1–18.

[18] R. S. Ruoff, D. Qian, and W. K. Liu, “Mechanical properties of carbon nanotubes: Theoretical predictions and experimental measurements,” *Comptes Rendus Phys.*, vol. 4, no. 9, pp. 993–1008, 2003, doi: 10.1016/j.crhy.2003.08.001.

[19] Z. Ren, Y. Lan, and Y. Wang, *Aligned Carbon Nanotubes Physics, Concepts, Fabrication and Devices*, vol. 121–123, no. PART 2. Springer, 2012.

[20] M. Balasubramanian and P. Jawahar, “Rubber-CNT Nanocomposites,” in *Advances in Nanostructured Composites*, M. Aliofkhazraei, Ed. CRC Press, 2019, pp. 295–314.

[21] S. Iijima and T. Ichihashi, “Single-shell carbon nanotubes of 1-nm diameter,” *Nature*, vol. 363, no. 6430, pp. 603–605, 1993, doi: 10.1038/363603a0.

[22] R. Bacon, “Growth, Structure, and Properties of Graphite Whiskers,” *J. Appl. Phys.*, vol. 31, no. 2, pp. 283–290, 1960, doi: 10.1063/1.1735559.

[23] M. J. Hanus and A. T. Harris, “Synthesis , Characterisation and Applications of Coiled Carbon Nanotubes,” *J. Nanosci. Nanotechnol.*, vol. 10, no. 4, pp. 2261–2283, 2010, doi: 10.1166/jnn.2010.1912.

[24] M. Terrones, “Science and Technology of the Twenty-First Century: Synthesis, Properties, and Applications of Carbon Nanotubes,” *Annu. Rev. Mater. Res.*, vol. 33, pp. 419–501, 2003, doi: 10.1146/annurev.matsci.33.012802.100255.

[25] M. S. Dresselhaus, G. Dresselhaus, and P. C. Eklund, *Science of Fullerenes and Carbon Nanotubes*. Academic Press, 1996.

[26] E. T. Thostenson, R. Zhifeng, and C. Tsu-Wei, “Advances in the sciences and technology of carbon nanotubes and their composites: a review,” *Compos. Sci. Technol.*, pp. 1899–1912, 2001, doi: 10.1016/j.matpr.2018.03.038.

[27] C. N. R. Rao, R. Voggu, and A. Govindaraj, “Selective generation of single-walled carbon nanotubes with metallic, semiconducting and other unique electronic properties,” *Nanoscale*, vol. 1, no. 1, pp. 96–105, 2009, doi: 10.1039/b9nr00104b.

[28] W. Ruland, A. K. Schaper, H. Hou, and A. Greiner, “Multi-wall carbon nanotubes with uniform chirality: Evidence for scroll structures,” *Carbon N. Y.*, vol. 41, no. 3, pp. 423–427, 2003, doi: 10.1016/S0008-6223(02)00342-1.

[29] P. J. F. Harris, *Carbon Nanotube Science - Synthesis, properties and applications*. Cambridge University Press, 2009.

[30] M. Loos, “Production of CNTs and Risks to Health,” in *Carbon Nanotube Reinforced Composites*, Elsevier, 2015, pp. 103–123.

[31] N. M. Nurazzi *et al.*, “Fabrication, functionalization, and application of carbon nanotube-reinforced polymer composite: An overview,” *Polymers (Basel).*, vol. 13, no. 7, pp. 1–45, 2021, doi: 10.3390/polym13071047.

[32] A. Thess, R. Lee, P. Nikolaev, and H. Dai, “Crystalline Ropes of Metallic Carbon Nanotubes,” *Science (80-.).*, vol. 273, no. 4, pp. 483–487, 1996, doi: 10.2307/1384782.

[33] T. Guo, P. Nikolaev, A. Thess, D. T. Colbert, and R. E. Smalley, “Catalytic growth of single-walled nanotubes by laser vaporization,” *Chem. Phys. Lett.*, vol. 243, no. 1–2, pp. 49–54, 1995, doi: 10.1016/0009-2614(95)00825-O.

[34] M. L. Terranova, V. Sessa, and M. Rossi, “The World of Carbon Nanotubes: An Overview of CVD Growth Methodologies,” *Chem. Vap. Depos.*, vol. 12, no. 6, pp. 315–325, 2006, doi: 10.1002/cvde.200600030.

[35] J. N. Coleman, U. Khan, W. J. Blau, and Y. K. Gun’ko, “Small but strong: A review of the mechanical properties of carbon nanotube-polymer composites,” *Carbon N. Y.*, vol. 44, no. 9, pp. 1624–1652, 2006, doi: 10.1016/j.carbon.2006.02.038.

[36] Q. Lu and B. Bhattacharya, “Effect of randomly occurring Stone-Wales defects on mechanical properties of carbon nanotubes using atomistic simulation,” *Nanotechnology*, vol. 16, no. 4, pp. 555–566, 2005, doi: 10.1088/0957-4484/16/4/037.

[37] K. Sharma, K. K. Saxena, and M. Shukla, “Effect of Multiple Stone-Wales and Vacancy

Defects on the Mechanical Behavior of Carbon Nanotubes Using Molecular Dynamics," *Procedia Eng.*, vol. 38, pp. 3373–3380, 2012, doi: 10.1016/j.proeng.2012.06.390.

[38] N. A. Sakharova, A. F. G. Pereira, J. M. Antunes, and J. V. Fernandes, "Numerical simulation study of the elastic properties of single-walled carbon nanotubes containing vacancy defects," *Compos. Part B Eng.*, vol. 89, pp. 155–168, 2016, doi: 10.1016/j.compositesb.2015.11.029.

[39] R. Rafiee and M. Mahdavi, "Characterizing nanotube-polymer interaction using molecular dynamics simulation," *Comput. Mater. Sci.*, vol. 112, pp. 356–363, 2016, doi: 10.1016/j.commatsci.2015.10.041.

[40] P. G. Collins, "Defects and Disorder in Carbon Nanotubes," in *Oxford Hand Book of Nanoscience and Technology: Volume 2: Materials*, A. V. Narlikar and Y. Y. Fu, Eds. Oxford University Press, 2010, pp. 31–81.

[41] A. J. Stone and D. J. Wales, "Theoretical Studies of Icosahedral C60 and Some Related Species," *Chem. Phys. Lett.*, vol. 128, no. 5,6, pp. 501–503, 1986, [Online]. Available: https://www.sciencedirect.com/science/article/abs/pii/0009261486806613.

[42] M. Mahboob and M. Z. Islam, "Effect of Vacancy and Stone-Wales Defects on The Shear Strength of Carbon Nanotube-Polymer Interfaces," *Adv. Mater. Res.*, vol. 970, no. i, pp. 263–266, 2014, doi: 10.4028/www.scientific.net/AMR.970.263.

[43] "Novel Sensors Could Enable Smarter Textiles," *University of Delaware College of Engineering Communications Staff*, 2018. https://www.udel.edu/udaily/2018/august/smart-textiles-nanotube-sensors/.

[44] T. Schumacher and E. T. Thostenson, "Development of structural carbon nanotube-based sensing composites for concrete structures," *J. Intell. Mater. Syst. Struct.*, vol. 25, no. 11, pp. 1331–1339, 2014, doi: 10.1177/1045389X13505252.

[45] S. Park, P. T. Theilmann, P. M. Asbeck, and P. R. Bandaru, "Enhanced Electromagnetic Interference Shielding Through the Use of Functionalized Carbon- Nanotube-Reactive Polymer Composites," *IEEE Trans. Nanotechnol.*, vol. 9, no. 4, pp. 464–469, 2010, [Online]. Available: https://ieeexplore.ieee.org/stamp/stamp.jsp?tp=&arnumber=5282625.

[46] A. M. Díez-Pascual, "Chemical Functionalization of Carbon Nanotubes with Polymers: A Brief Overview," *Macromol*, vol. 1, no. 2, pp. 64–83, 2021, doi: 10.3390/macromol1020006.

[47] ASTM International, "Standard Test Method for Tensile Properties of Plastics D638-14," 2014. doi: 10.1520/D0638-14.1.

[48] ASTM International, “Standard Test Methods for Flexural Properties of Unreinforced and Reinforced Plastics and Electrical Insulating Materials D790-17,” 2017. doi: 10.1520/D0790-17.2.

[49] ASTM International, “Standard Test Method for Flexural Properties of Unreinforced and Reinforced Plastics and Electrical Insulating Materials by Four-Point Bending D6272-17e1,” 2017. doi: 10.1520/D6272-17E01.1.

[50] ASTM International, “Standard Test Method for Determining the Charpy Impact Resistance of Notched Specimens of Plastics D6110-18,” 2018. doi: 10.1520/D6110-18.1.

[51] ASTM International, “Standard Test Methods for Determining the Izod Pendulum Impact Resistance of Plastics D256-10 (Reapproved 2018),” 2018. doi: 10.1520/D0256-10R18.N.

[52] NIOSH, “Current Intelligence Bulletin 65: Occupational Exposure to Carbon Nanotubes and Nanofibers,” 2013. [Online]. Available: https://www.cdc.gov/niosh/docs/2013-145/default.html.

[53] K. Aschberger *et al.*, “Review of carbon nanotubes toxicity and exposure — Appraisal of human health risk assessment based on open literature,” *Taylor Fr.*, vol. 8444, pp. 759–790, 2010, doi: 10.3109/10408444.2010.506638.

[54] S. Luanpitpong, L. Wang, and Y. Rojanasakul, “The effects of carbon nanotubes on lung and dermal cellular behaviors,” *Nanomedicine*, vol. 9, pp. 895–912, 2014, [Online]. Available: https://www.futuremedicine.com/doi/abs/10.2217/nnm.14.42.

[55] A. R. Murray *et al.*, “Factoring-in agglomeration of carbon nanotubes and nanofibers for better prediction of their toxicity versus asbestos,” *Part. Fibre Toxicol.*, vol. 9, pp. 1–19, 2012, doi: 10.1186/1743-8977-9-10.

[56] D. W. Porter *et al.*, “Mouse pulmonary dose- and time course-responses induced by exposure to multi-walled carbon nanotubes,” *Toxicology*, vol. 269, no. 2–3, pp. 136–147, 2010, doi: 10.1016/j.tox.2009.10.017.

[57] A. Takagi *et al.*, “Induction of mesothelioma in p53+/- mouse by intraperitoneal application of multi-wall carbon nanotube,” *J. Toxicol. Sci.*, vol. 33, no. 1, pp. 105–116, 2008, doi: 10.2131/jts.33.105.

[58] A. T. Saber *et al.*, “Epoxy composite dusts with and without carbon nanotubes cause similar pulmonary responses, but differences in liver histology in mice following pulmonary deposition,” *Part. Fibre Toxicol.*, vol. 13, no. 1, 2016, doi: 10.1186/s12989-016-0148-2.

[59] S. Koyama *et al.*, "Role of systemic T-cells and histopathological aspects after subcutaneous implantation of various carbon nanotubes in mice," *Carbon N. Y.*, vol. 44, no. 6, pp. 1079–1092, 2006, doi: 10.1016/j.carbon.2005.08.006.

[60] D. Mohanta, S. Patnaik, S. Sood, and N. Das, "Carbon nanotubes: Evaluation of toxicity at biointerfaces," *J. Pharm. Anal.*, vol. 9, no. 5, pp. 293–300, 2019, doi: 10.1016/j.jpha.2019.04.003.

[61] Health and Safety Executive (HSE), "Using nanomaterials at work," 2013. [Online]. Available: https://www.hse.gov.uk/pubns/books/hsg272.pdf.

[62] British Standards (BSI), "Part 2: Guide to safe handling and disposal of manufactured nanomaterials," 2007. [Online]. Available: https://shop.bsigroup.com/upload/Shop/Download/Nano/PD6699-2.pdf.

[63] ASTM International, "Standard Guide for Handling Unbound Engineered Nanoscale Particles in Occupational Settings E2535 − 07 (Reapproved 2018)," 2018. doi: 10.1520/E2535-07R18.empirical.

[64] Occupational Safety and Health Administration (OSHA), "Assigned Protection Factors for the Revised Respiratory Protection Standard," 2009. doi: 10.1016/j.jchas.2006.01.007.

[65] Safe Work Australia, "Safe Handling and Use of Carbon Nanotubes," 2012. [Online]. Available: http://eprints.internano.org/1744/1/Safe Handling and Use of Carbon Nanotubes.pdf.

[66] British Standards (BSI), "Disposal of manufacturing process waste containing manufactured nano-objects – Guide PAS 138:2012," *BSI Stand. Publ.*, p. 32, 2012.

[67] World Health Organization (WHO), "WHO Guidelines on Protecting Workers From Potential Risks of Manufactured Nanomaterials," 2017. doi: 10.1093/occmed/kqz070.

[68] N. Vu-Bac, T. Rabczuk, and X. Zhuang, "Chapter 15-Continuum/Finite Element Modeling of Carbon Nanotube-Reinforced Polymers," in *Carbon Nanotube-Reinforced Polymers: From Nanoscale to Macroscale*, 1st ed., R. Rafiee, Ed. Elsevier Inc., 2018, pp. 385–409.

[69] M. M. Shokrieh and R. Rafiee, "Stochastic multi-scale modeling of CNT/polymer composites," *Comput. Mater. Sci.*, vol. 50, no. 2, pp. 437–446, 2010, doi: 10.1016/j.commatsci.2010.08.036.

[70] H. Ghasemi, R. Rafiee, X. Zhuang, J. Muthu, and T. Rabczuk, "Uncertainties propagation in metamodel-based probabilistic optimization of CNT/polymer composite structure using

stochastic multi-scale modeling," *Comput. Mater. Sci.*, vol. 85, pp. 295–305, 2014, doi: 10.1016/j.commatsci.2014.01.020.

[71] N. Vu-Bac, R. Rafiee, X. Zhuang, T. Lahmer, and T. Rabczuk, "Uncertainty quantification for multiscale modeling of polymer nanocomposites with correlated parameters," *Compos. Part B Eng.*, vol. 68, pp. 446–464, 2015, doi: 10.1016/j.compositesb.2014.09.008.

[72] G. M. Odegard, T. S. Gates, K. E. Wise, C. Park, and E. J. Siochi, "Constitutive modeling of nanotube-reinforced polymer composites," *Compos. Sci. Technol.*, vol. 63, no. 11, pp. 1671–1687, 2003, doi: 10.1016/S0266-3538(03)00063-0.

[73] X. Lu and Z. Hu, "Mechanical property evaluation of single-walled carbon nanotubes by finite element modeling," *Compos. Part B Eng.*, vol. 43, no. 4, pp. 1902–1913, 2012, doi: 10.1016/j.compositesb.2012.02.002.

[74] C. Li and T. W. Chou, "A structural mechanics approach for the analysis of carbon nanotubes," *Int. J. Solids Struct.*, vol. 40, no. 10, pp. 2487–2499, 2003, doi: 10.1016/S0020-7683(03)00056-8.

[75] A. L. Kalamkarov, A. V. Georgiades, S. K. Rokkam, V. P. Veedu, and M. N. Ghasemi-Nejhad, "Analytical and numerical techniques to predict carbon nanotubes properties," *Int. J. Solids Struct.*, vol. 43, no. 22–23, pp. 6832–6854, 2006, doi: 10.1016/j.ijsolstr.2006.02.009.

[76] J. M. Wernik and S. A. Meguid, "Multiscale modeling of the nonlinear response of nano-reinforced polymers," *Acta Mech.*, vol. 217, no. 1–2, pp. 1–16, 2011, doi: 10.1007/s00707-010-0377-7.

[77] T. Belytschko, S. P. Xiao, G. C. Schatz, and R. S. Ruoff, "Atomistic simulations of nanotube fracture," *Phys. Rev. B - Condens. Matter Mater. Phys.*, vol. 65, no. 23, pp. 1–8, 2002, doi: 10.1103/PhysRevB.65.235430.

[78] M. J. S. Zuberi and V. Esat, "Investigating the mechanical properties of single walled carbon nanotube reinforced epoxy composite through finite element modelling," *Compos. Part B Eng.*, vol. 71, pp. 1–9, 2015, doi: 10.1016/j.compositesb.2014.11.020.

[79] M. M. Shokrieh and R. Rafiee, "Prediction of mechanical properties of an embedded carbon nanotube in polymer matrix based on developing an equivalent long fiber," *Mech. Res. Commun.*, vol. 37, no. 2, pp. 235–240, 2010, doi: 10.1016/j.mechrescom.2009.12.002.

[80] M. M. Shokrieh and R. Rafiee, "On the tensile behavior of an embedded carbon nanotube in polymer matrix with non-bonded interphase region," *Compos. Struct.*, vol. 92, no. 3, pp. 647–

652, 2010, doi: 10.1016/j.compstruct.2009.09.033.

[81] M. M. Shokrieh and R. Rafiee, “Investigation of nanotube length effect on the reinforcement efficiency in carbon nanotube based composites,” *Compos. Struct.*, vol. 92, no. 10, pp. 2415–2420, 2010, doi: 10.1016/j.compstruct.2010.02.018.

[82] J. M. Wernik and S. A. Meguid, “Multiscale micromechanical modeling of the constitutive response of carbon nanotube-reinforced structural adhesives,” *Int. J. Solids Struct.*, vol. 51, no. 14, pp. 2575–2589, 2014, doi: 10.1016/j.ijsolstr.2014.03.009.

[83] D. Shi, X. Feng, Y. Y. Huang, K.-C. Hwang, and H. Gao, “The Effect of Nanotube Waviness and Agglomeration on the Elastic Property of Carbon Nanotube-Reinforced Composites,” *J. Eng. Mater. Technol.*, vol. 126, no. July, pp. 205–257, 2004, doi: 10.1115/1.1751182.

[84] T. Mori and K. Tanaka, “Average Stress in Matrix and Average Elastic Energy of Materials With Misfitting Inclusions,” *Acta Metall.*, vol. 21, no. 5, pp. 571–574, 1973, doi: 10.1016/0001-6160(73)90064-3.

[85] T. Mura, *Micromechanics of Defects in Solids*, Second, Re. Martinus Nijhoff Publishers, 1987.

[86] J. D. Eshelby, “The determination of the elastic field of an ellipsoidal inclusion, and related problems,” *Math. Proc. Cambridge Philos. Soc.*, vol. 241, pp. 376–396, 1957, doi: 10.1017/S0305004100053366.

[87] R. Hill, “A Self-Consistent Mechanics of Composite Materials,” *J. Mech. Phys. Solids*, vol. 13, no. 4, pp. 213–222, 1965, doi: 10.1016/0022-5096(65)90010-4.

[88] R. I. Rubel, M. H. Ali, M. A. Jafor, and M. M. Alam, “Carbon nanotubes agglomeration in reinforced composites: A review,” *AIMS Mater. Sci.*, vol. 6, no. 5, pp. 756–780, 2019, doi: 10.3934/matersci.2019.5.756.

[89] B. M. S. P. Shaffer and A. H. Windle, “Fabrication and Characterization of Carbon Nanotube / Poly (vinyl alcohol) Composites,” *Adv. Mater.*, pp. 937–941, 1999, [Online]. Available: https://onlinelibrary.wiley.com/doi/abs/10.1002/(SICI)1521-4095(199908)11:11%3C937::AID-ADMA937%3E3.0.CO;2-9.

[90] B. Vigolo *et al.*, “Macroscopic Fibers and Ribbons of Oriented Carbon Nanotubes,” *Science (80-.).*, vol. 290, no. 5495, pp. 1331–1334, 2000, doi: 10.1126/science.290.5495.1331.

[91] C. Stéphan, T. P. Nguyen, M. L. De La Chapelle, S. Lefrant, C. Journet, and P. Bernier, “Characterization of singlewalled carbon nanotubes-PMMA composites,” *Synth. Met.*, vol.

108, no. 2, pp. 139–149, 2000, doi: 10.1016/S0379-6779(99)00259-3.

[92] W. Voigt, “Ueber die Beziehung zwischen den beiden Elasticitätsconstanten isotroper Körper,” *Ann. Phys.*, vol. 274, pp. 573–587, 1889, [Online]. Available: https://onlinelibrary.wiley.com/doi/10.1002/andp.18892741206.

[93] A. Reuss, “Berechnung der Fließgrenze von Mischkristallen auf Grund der Plastizitätsbedingung für Einkristalle,” *Zeitschrift für Angew. Math. und Mech.*, vol. 8, no. 9, pp. 49–58, 1929, [Online]. Available: https://onlinelibrary.wiley.com/doi/10.1002/zamm.19290090104.

[94] Z. Hashin and S. Shtrikman, “A Variational Approach to the Theory of the Elastic Behaviour of Multiphase Materials,” *J. Mech. Phys. Solids*, vol. 11, no. 2, pp. 127–140, 1963, doi: 10.1016/0022-5096(63)90060-7.

[95] H. L. Cox, “The elasticity and strength of paper and other fibrous materials,” *Br. J. Appl. Phys.*, vol. 3, no. 3, pp. 72–79, 1952, doi: 10.1088/0508-3443/3/3/302.

[96] G. P. Carman and K. L. Reifsnider, “Micromechanics of short-fiber composites,” *Compos. Sci. Technol.*, vol. 43, no. 2, pp. 137–146, 1992, doi: 10.1016/0266-3538(92)90004-M.

[97] M. Loos, “Fundamentals of Polymer Matrix Composites Containing CNTs,” in *Carbon Nanotube Reinforced Composites*, Elsevier, 2015, pp. 125–170.

[98] J. Pan and L. Bian, “Influence of agglomeration parameters on carbon nanotube composites,” *Acta Mech.*, vol. 228, no. 6, pp. 2207–2217, 2017, doi: 10.1007/s00707-017-1820-9.

[99] Y. P. Qiu and G. J. Weng, “On the Application of Mori-Tanaka’s Theory Involving Transversely Isotropic Spheroidal Inclusions,” *Int. J. Eng. Sci.*, vol. 28, no. 11, pp. 1121–1137, 1990, doi: 10.1016/0020-7225(90)90112-V.

[100] C. Y. Hui and D. Shia, “Simple Formulae for the Effective Moduli of Unidirectional Aligned Composites,” *Polym. Eng. Sci.*, vol. 38, no. 5, pp. 774–782, 1998, doi: 10.1002/pen.10243.

[101] H. Hu, L. Onyebueke, and A. Abatan, “Characterizing and Modeling Mechanical Properties of Nanocomposites-Review and Evaluation,” *J. Miner. Mater. Charact. Eng.*, vol. 09, no. 04, pp. 275–319, 2010, doi: 10.4236/jmmce.2010.94022.

[102] J. Wang and R. Pyrz, “Prediction of the overall moduli of layered silicate-reinforced nanocomposites-part I: Basic theory and formulas,” *Compos. Sci. Technol.*, vol. 64, no. 7–8, pp. 925–934, 2004, doi: 10.1016/S0266-3538(03)00024-1.

[103] E. Yarali, M. Baniassadi, and M. Baghani, “Numerical homogenization of coiled carbon

nanotube reinforced shape memory polymer nanocomposites," *Smart Mater. Struct.*, vol. 28, no. 3, 2019, doi: 10.1088/1361-665X/ab02b6.

[104] E. Yousefi, A. Sheidaei, M. Mahdavi, M. Baniassadi, M. Baghani, and G. Faraji, "Effect of nanofiller geometry on the energy absorption capability of coiled carbon nanotube composite material," *Compos. Sci. Technol.*, vol. 153, pp. 222–231, 2017, doi: 10.1016/j.compscitech.2017.10.025.

[105] Y. Pan, L. Iorga, and A. A. Pelegri, "Analysis of 3D random chopped fiber reinforced composites using FEM and random sequential adsorption," *Comput. Mater. Sci.*, vol. 43, no. 3, pp. 450–461, 2008, doi: 10.1016/j.commatsci.2007.12.016.

[106] N. Khani, M. Yildiz, and B. Koc, "Elastic properties of coiled carbon nanotube reinforced nanocomposite: A finite element study," *Mater. Des.*, vol. 109, pp. 123–132, 2016, doi: 10.1016/j.matdes.2016.06.126.

[107] L. Chen, B. Gu, J. Zhou, and J. Tao, "Study of the Effectiveness of the RVEs for Random Short Fiber Reinforced Elastomer Composites," *Fibers Polym.*, vol. 20, no. 7, pp. 1467–1479, 2019, doi: 10.1007/s12221-019-1178-9.

[108] E. Moaseri, M. Karimi, M. Baniadam, and M. Maghrebi, "Improvements in mechanical properties of multi-walled carbon nanotube-reinforced epoxy composites through novel magnetic-assisted method for alignment of carbon nanotubes," *Compos. Part A Appl. Sci. Manuf.*, vol. 64, pp. 228–233, 2014, doi: 10.1016/j.compositesa.2014.05.014.

[109] D. Shi *et al.*, "Magnetic alignment of Ni/Co-coated carbon nanotubes in polystyrene composites," *Compos. Part B Eng.*, vol. 42, no. 6, pp. 1532–1538, 2011, doi: 10.1016/j.compositesb.2011.04.014.

[110] E. W. Weisstein, "Sphere Point Picking," *MathWorld-A Wolfram Web Resource*. https://mathworld.wolfram.com/SpherePointPicking.html.

[111] G. Marsaglia, "Choosing a Point From the Surface of a Sphere," *Ann. Mat. Stat.*, vol. 43, no. 2, pp. 645–646, 1972, doi: 10.1214/aoms/1177692644.

[112] Y. Bin Jia, "Plücker Coordinates for Lines in the Space," 2020. [Online]. Available: https://faculty.sites.iastate.edu/jia/files/inline-files/plucker-coordinates.pdf.

[113] "Intersection Point of Two Lines in 3D Space," 2021. https://www.toppr.com/ask/content/story/amp/intersection-point-of-two-lines-in-3d-9406/.

[114] J. Ketchel and P. Larochelle, "Collision Detection of Cylindrical Rigid Bodies for Motion

Planning," in *Proceedings - IEEE International Conference on Robotics and Automation*, 2006, no. May, pp. 1530–1535, doi: 10.1109/ROBOT.2006.1641925.

[115] E. W. Weisstein, "Helix," *MathWorld-A Wolfram Web Resource*. https://mathworld.wolfram.com/Helix.html.

[116] G. Arfken, *Mathematical Methods for Physicists*, Third Edit. Academic Press, 1985.

[117] D. H. Pahr and P. K. Zysset, "Influence of boundary conditions on computed apparent elastic properties of cancellous bone," *Biomech. Model. Mechanobiol.*, vol. 7, no. 6, pp. 463–476, 2008, doi: 10.1007/s10237-007-0109-7.

[118] M. Ostoja-Starzewski, "Material spatial randomness: From statistical to representative volume element," *Probabilistic Eng. Mech.*, vol. 21, no. 2, pp. 112–132, 2006, doi: 10.1016/j.probengmech.2005.07.007.

[119] MSC Software, "Marc 2021.3, Volume B: Element Library," 2021.

[120] M. A. Bhuiyan, R. V. Pucha, J. Worthy, M. Karevan, and K. Kalaitzidou, "Understanding the effect of CNT characteristics on the tensile modulus of CNT reinforced polypropylene using finite element analysis," *Comput. Mater. Sci.*, vol. 79, pp. 368–376, 2013, doi: 10.1016/j.commatsci.2013.06.046.

[121] M. J. S. Zuberi and V. Esat, "Evaluating the effects of size and chirality on the mechanical properties of single-walled carbon nanotubes through equivalent-continuum modelling," *Proc. Inst. Mech. Eng. Part L J. Mater. Des. Appl.*, vol. 230, no. 5, pp. 913–926, 2016, doi: 10.1177/1464420715588217.

[122] E. T. Thostenson and T. W. Chou, "On the elastic properties of carbon nanotube- based composites: modelling and characterization," *J. Phys. D. Appl. Phys.*, vol. 47, no. 7, pp. 573–582, 2003, doi: 10.1088/0022-3727/47/7/079501.

[123] R. Rafiee and H. Zehtabzadeh, "Predicting the strength of carbon nanotube reinforced polymers using stochastic bottom-up modeling," *Appl. Phys. A Mater. Sci. Process.*, vol. 126, no. 8, pp. 1–13, 2020, doi: 10.1007/s00339-020-03784-z.

[124] R. Rafiee and A. Ghorbanhosseini, "Investigating interaction between CNT and polymer using cohesive zone model," *Polym. Compos.*, vol. 39, no. 11, pp. 3903–3911, 2018, doi: 10.1002/pc.24428.

[125] X. Liu, Q. Yang, and L. Su, "Interface analysis and design in carbon nanotube array composite based on cohesive finite element approach," *Mater. Sci. Eng. A*, vol. 592, pp. 83–

87, 2014, doi: 10.1016/j.msea.2013.10.100.

[126] MSC Software, “Marc 2021.3, Volume A : Theory and User Information,” 2021.

[127] H. Tan, L. Y. Jiang, Y. Huang, B. Liu, and K. C. Hwang, “The effect of van der Waals-based interface cohesive law on carbon nanotube-reinforced composite materials,” *Compos. Sci. Technol.*, vol. 67, no. 14, pp. 2941–2946, 2007, doi: 10.1016/j.compscitech.2007.05.016.

[128] S. Timoshenko and J. N. Goodier, *Theory of Elasticity*, 2nd ed. McGraw-Hill Book Company, Inc., 1951.

[129] A. Kianfar, M. M. Seyyed Fakhrabadi, and M. M. Mashhadi, “Prediction of mechanical and thermal properties of polymer nanocomposites reinforced by coiled carbon nanotubes for possible application as impact absorbent,” *Proc. Inst. Mech. Eng. Part C J. Mech. Eng. Sci.*, vol. 234, no. 4, pp. 882–902, 2020, doi: 10.1177/0954406219885969.

[130] E. Yousefi, M. Mahdavi, and M. Baniassadi, “Investigating mechanical properties of coiled carbon nanotube reinforced nanocomposite,” in *The 25th Annual International Conference on Mechanical Engineering ISME2017*, 2017, no. May, pp. 1–3.

APPENDICES

A. Flowchart of CNT Generation Algorithm

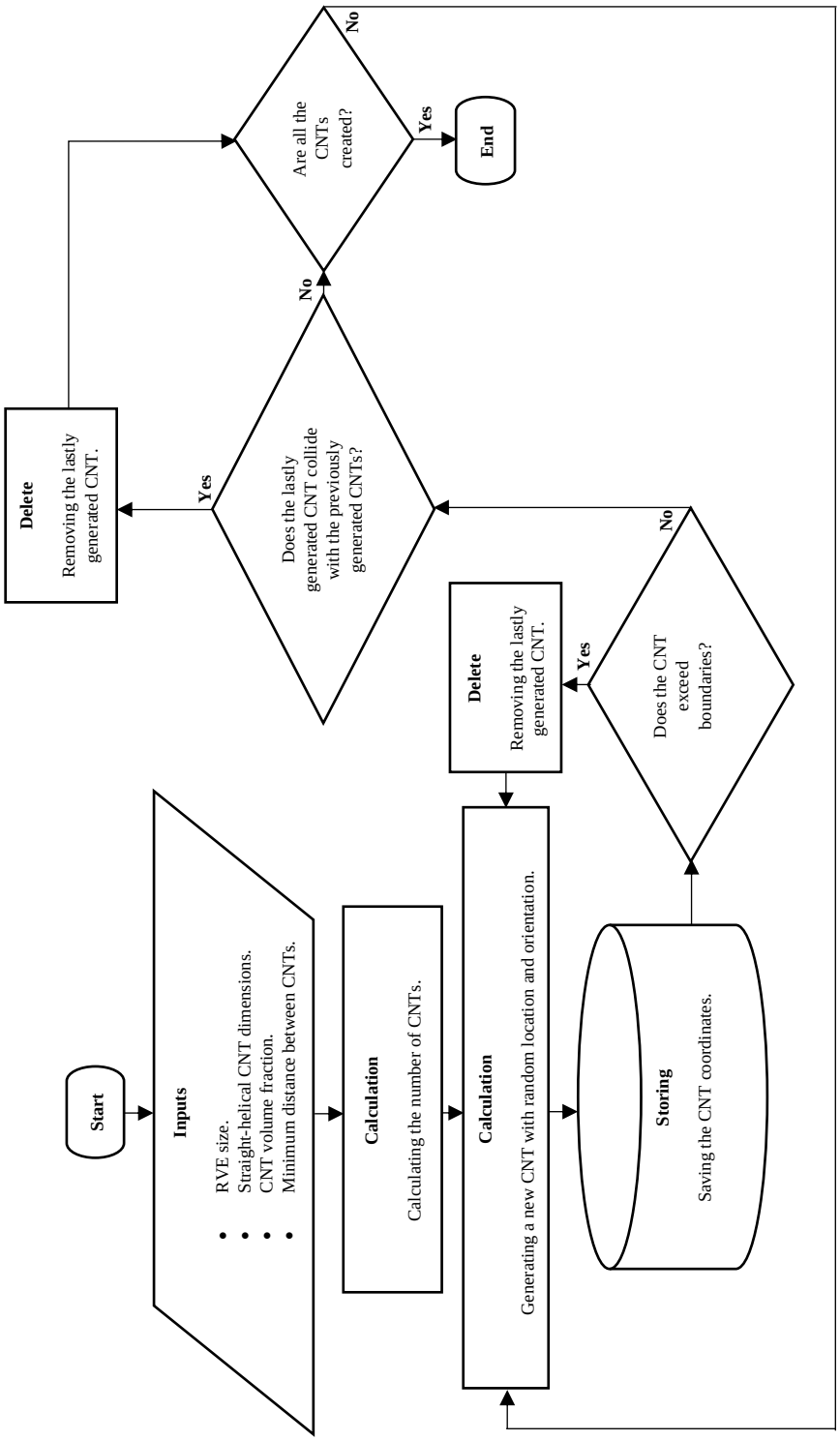

Figure A.1: Flowchart of CNT generation algorithm.

B. Cohesive Interface Data

The data of Figures 3.16 and 3.17 are given in Tables B.1 and B.2, respectively.

Table B.1: *Bilinear traction-separation curve data (normal direction).*

Number of Point	Separation (nm)	Traction (MPa)
1	0	0
2	0.0542	479
3	0.4468	0

Table B.2: *Bilinear traction-separation curve data (tangential direction).*

Number of Point	Separation (nm)	Traction (MPa)
1	0	0
2	0.2234	278
3	1.8417	0

The data entered in Marc-Mentat 2021.3 are given in Table B.3.

Table B.3: *Cohesive interface properties entered in Marc-Mentat 2021.3.*

Cohesive Property	Value
Cohesive Energy ([N x 10^{-8}]/nm)	0.0107
Critical Opening Displacement (nm)	0.0542
Maximum Opening Displacement (nm)	0.4468

Shear/Normal Coefficient	Value
Maximum Stress	0.5804
Cohesive Energy	2.3925

C. Sensitivity Analysis Data

The data of Figure 4.1 are given in Table C.1.

Table C.1: *Sensitivity analysis data.*

Number of Point	Number of Elements	Young's Modulus, E (GPa)
1	214,823	10.055
2	271,401	10.194
3	351,205	10.319
4	467,727	10.315
5	557,684	10.317

D. Tabulated Results of FEAs

In this section the results of FEAs are presented in tables.

Table D.1: *Effect of CNT volume fraction on elastic properties (randomly oriented CNTs).*

Type of CNT	Volume Fraction (%)	E_c (GPa)	G_c (GPa)	ν_c
Blunt-SWNT	0.5	10.034	3.862	0.299
“	1	10.264	3.948	0.300
“	1.5	10.570	4.074	0.297
“	2	10.925	4.218	0.295
“	2.5	11.526	4.442	0.297
“	3	11.823	4.551	0.299
“	3.5	12.893	4.960	0.300
“	4	13.281	5.103	0.301
Capped-SWNT	0.5	10.031	3.864	0.298
“	1	10.399	4.006	0.298
“	1.5	10.578	4.086	0.295
“	2	10.791	4.163	0.296
“	2.5	11.598	4.479	0.295
“	3	11.920	4.607	0.294
“	3.5	12.798	4.915	0.302
“	4	13.272	5.091	0.304

Table D.2: *Effect of CNT volume fraction on max. stress and strain in CNT (randomly oriented CNTs).*

Type of CNT	Volume Fraction (%)	Max. Equivalent Von Mises Stress in CNT (GPa)	Max. Equivalent Elastic Strain in CNT
Blunt-SWNT	0.5	2.516	0.0030
“	1	5.077	0.0061
“	1.5	3.980	0.0046
“	2	4.107	0.0049
“	2.5	4.454	0.0054
“	3	7.241	0.0090
“	3.5	12.720	0.0151
Capped-SWNT	0.5	3.067	0.0037
“	1	9.706	0.0115
“	1.5	3.231	0.0039
“	2	3.744	0.0045
“	2.5	13.790	0.0163
“	3	8.235	0.0099
“	3.5	7.258	0.0086
“	4	13.440	0.0158

Table D.3: *Effect of CCNT helix angle on elastic properties (randomly oriented CNTs).*

Type of CNT	Volume Fraction (%)	Helix Angle (Degree)	E_c (GPa)	G_c (GPa)	ν_c
Blunt-CCNT	1	30	10.060	3.881	0.2961
Blunt-CCNT	1	60	10.140	3.911	0.2962
Blunt-CCNT	1	90	10.264	3.948	0.3001

Table D.4: *Effect of CCNT number of revolutions on elastic properties (randomly oriented CNTs).*

Type of CNT	Volume Fraction (%)	Number of Revolutions	E_c (GPa)	G_c (GPa)	ν_c
Blunt-CCNT	1	3	10.060	3.881	0.2961
Blunt-CCNT	1	4	10.157	3.919	0.2959
Blunt-CCNT	1	5	10.267	3.962	0.2958

Table D.5: *Effect of CNT diameter on elastic properties (randomly oriented CNTs).*

Type of CNT	Volume Fraction (%)	CNT Outer Diameter (nm)	E_c (GPa)	G_c (GPa)	ν_c
Blunt-CCNT	1	1.154	10.267	3.962	0.2958
Blunt-CCNT	1	1.696	10.133	3.910	0.2956
Blunt-CCNT	1	1.967	10.125	3.909	0.2948

Table D.6: *Effect of CCNT helix angle on elastic properties (aligned CNTs).*

Type of CNT	Volume Fraction (%)	Helix Angle (Degree)	E_{11} (GPa)	E_{22} (GPa)	G_{12} (GPa)	G_{23} (GPa)	ν_{12}
Blunt CCNT	1	30	10.147	10.147	4.142	4.123	0.2970
Blunt CCNT	1	60	10.761	10.118	4.102	4.079	0.3011
Blunt CCNT	1	90	11.952	9.981	3.855	3.845	0.3039

Table D.7: *Effect of CCNT number of revolutions on elastic properties (aligned CNTs).*

Type of CNT	Volume Fraction (%)	Number of Revolutions	E_{11} (GPa)	E_{22} (GPa)	G_{12} (GPa)	G_{23} (GPa)	ν_{12}
Blunt CCNT	1	3	10.147	10.147	4.142	4.123	0.2970
Blunt CCNT	1	4	10.204	10.189	4.187	4.167	0.2968
Blunt CCNT	1	5	10.321	10.304	4.298	4.275	0.2965

Table D.8: *Effect of CNT diameter on elastic properties (aligned CNTs).*

Type of CNT	Volume Fraction (%)	CNT Outer Diameter (nm)	E_{11} (GPa)	E_{22} (GPa)	G_{12} (GPa)	G_{23} (GPa)	ν_{12}
Blunt CCNT	1	1.154	10.321	10.304	4.298	4.275	0.2965
Blunt CCNT	1	1.696	10.205	10.126	4.131	4.110	0.2958
Blunt CCNT	1	1.967	10.162	10.061	4.061	4.040	0.2953

E. Further Information About FEAs

Table E.1: *Effect of CNT volume fraction (randomly oriented CNTs), further details.*

RVE Side Length (nm)	Type of CNT	Volume Fraction (%)	Number of CNTs	Number of Elements	Number of Nodes	Iterative Procedure	Matrix Solver
50	Blunt SWNT	0.5	18	188,882	55,449	Full Newton Raphson	CASI Iterative
"	"	1	35	372,873	106,832	"	"
"	"	1.5	52	580,983	163,374	"	"
"	"	2	70	800,072	222,476	"	"
"	"	2.5	87	1,091,362	295,250	"	"
"	"	3	104	1,269,346	345,223	"	"
"	"	3.5	121	1,609,374	428,174	"	"
"	"	4	139	1,893,454	500,513	"	"
"	Capped SWNT	0.5	18	189,965	55,456	"	"
"	"	1	35	351,205	102,450	"	"
"	"	1.5	53	580,715	163,656	"	"
"	"	2	70	771,333	216,012	"	"
"	"	2.5	88	1,050,665	287,471	"	"
"	"	3	105	1,299,876	349,777	"	"
"	"	3.5	123	1,601,956	426,842	"	"
"	"	4	140	1,855,356	490,528	"	"

Table E.2: *Effect of CCNT helix angle (randomly oriented CNTs), further details.*

RVE Side Length (nm)	Helix Angle (Degree)	Number of CNTs	Number of Elements	Number of Nodes	Iterative Procedure	Matrix Solver
50	30	35	541,203	164,561	Full Newton Raphson	CASI Iterative
"	60	35	414,497	127,828	"	"
"	90	35	372,873	106,832	"	"

Table E.3: *Effect of CCNT number of revolutions (randomly oriented CNTs), further details.*

RVE Side Length (nm)	Number of Revolutions	Number of CNTs	Number of Elements	Number of Nodes	Iterative Procedure	Matrix Solver
50	3	35	541,203	164,561	Full Newton Raphson	CASI Iterative
"	4	26	416,165	127,525	"	"
"	5	21	362,481	107,311	"	"

Table E.4: *Effect of CNT diameter (randomly oriented CNTs), further details.*

RVE Side Length (nm)	CNT Outer Diameter (nm)	Number of CNTs	Number of Elements	Number of Nodes	Iterative Procedure	Matrix Solver
50	1.154	21	362,481	107,311	Full Newton Raphson	CASI Iterative
“	1.696	10	138,302	43,373	“	“
“	1.967	8	118,605	36,910	“	“

Table E.5: *Effect of CCNT helix angle (aligned CNTs), further details.*

RVE Side Length (nm)	Helix Angle (Degree)	Number of CNTs	Number of Elements	Number of Nodes	Iterative Procedure	Matrix Solver
50	30	35	491,057	146,451	Full Newton Raphson	CASI Iterative
“	60	35	408,271	123,475	“	“
“	90	35	380,330	108,821	“	“

Table E.6: *Effect of CCNT number of revolutions (aligned CNTs), further details.*

RVE Side Length (nm)	Number of Revolutions	Number of CNTs	Number of Elements	Number of Nodes	Iterative Procedure	Matrix Solver
50	3	35	491,057	146,451	Full Newton Raphson	CASI Iterative
“	4	26	382,566	114,897	“	“
“	5	21	333,365	100,325	“	“

Table E.7: *Effect of CNT diameter (aligned CNTs), further details.*

RVE Side Length (nm)	CNT Outer Diameter (nm)	Number of CNTs	Number of Elements	Number of Nodes	Iterative Procedure	Matrix Solver
50	1.154	21	333,365	100,325	Full Newton Raphson	CASI Iterative
“	1.696	10	129,899	40,485	“	“
“	1.967	8	112,688	35,081	“	“